The Galaxy Population Evolution of Sunyaev-Zeldovich selected clusters

Ph.D. Thesis in Astrophysics

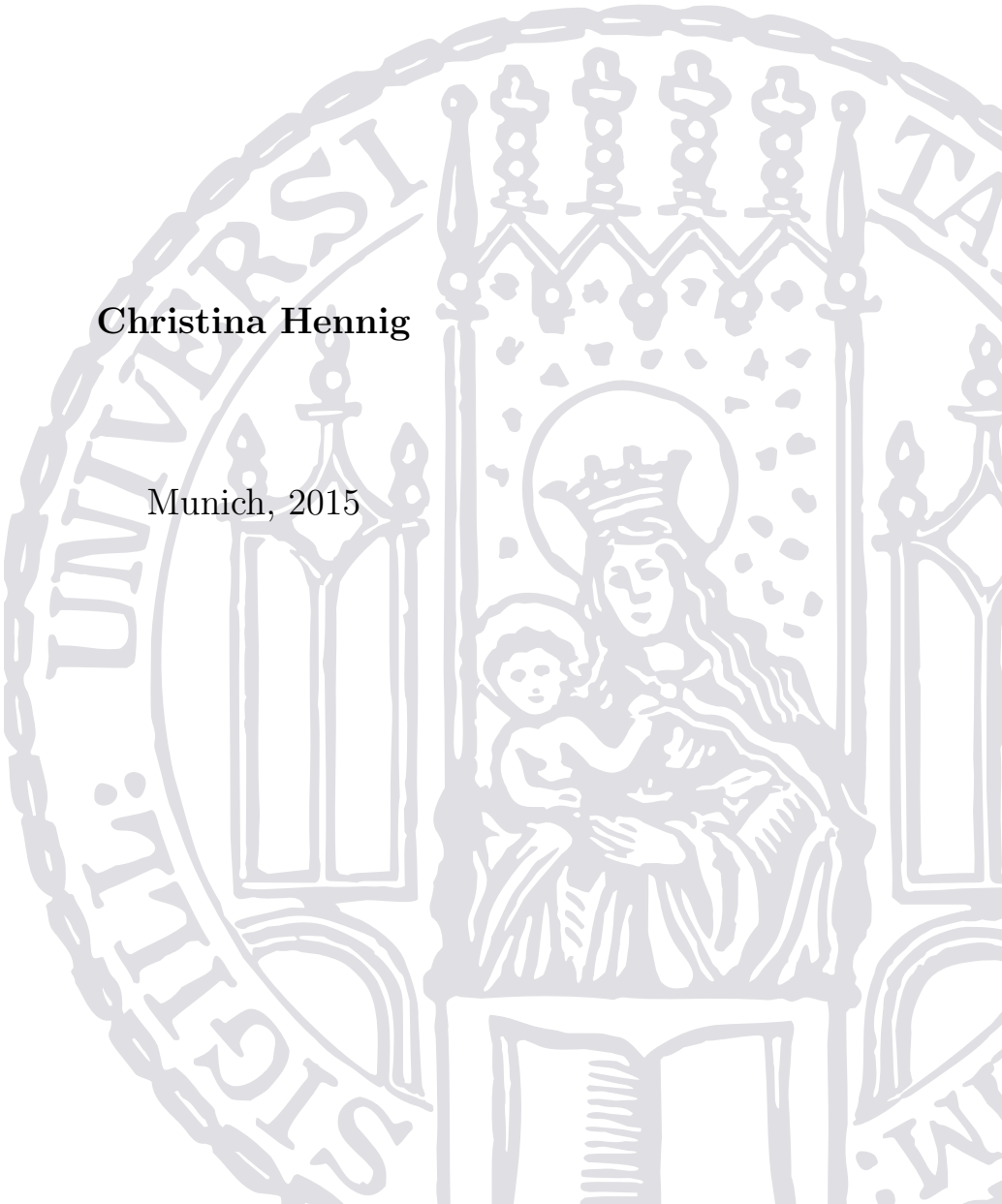

Christina Hennig

Munich, 2015

The Galaxy Population Evolution of Sunyaev-Zeldovich selected clusters

Ph.D. Thesis in Astrophysics

at the Faculty of Physics
of the Ludwig-Maximilians University Munich

submitted by

Christina Hennig

from Munich, Germany

Munich, 16th June 2015

First evaluator: Prof. Dr. Joseph J. Mohr
Second evaluator: Prof. Dr. Andreas Burkert

Date of the oral exam: July 14th, 2015

Zusammenfassung

Diese Arbeit präsentiert eine Studie über die Galaxienpopulation in massereichen Galaxienhaufen, welche mittels des Sunyaev-Zeldovich Effekt (SZE) durch das Südpol Teleskop entdeckt werden. Die Analyse basiert auf optischen Daten in fünf verschiedenen Filtern aus der initialen Verifikationsphase des Dark Energy Survey (DES). Diese Daten ermöglichen eine Studie mit insgesamt 74 Galaxienhaufen. Die Selektierung mittels des SZE erstellt ein rotverschiebungsunabhängiges und massenlimitiertes Galaxienhaufen-Sample. Für jeden dieser Galaxienhaufen errechnen wir eine robuste Massenabschätzung aus der Detektionssignifikanz des SZE und der vorgegebenen Rotverschiebung. Die Massenbestimmung berücksichtigt Korrekturen der SZE-Selektion und kosmologische Unsicherheiten. Aufgrund der optisch tiefen Daten des DES liegen die Galaxienhaufen in einem Rotverschiebungsbereich zwischen 0 und $\sim 1,1$. Es liegt dadurch ein ideales Galaxienhaufen-Sample für eine Studie über evolutionäre Tendenzen in Bezug auf Masse und Rotverschiebung vor.
Das erste Kapitel dieser Forschungsarbeit gibt einen Überblick über die physikalischen Prozesse und Charakteristika der Galaxienpopulation in Haufen. Ich informiere den Leser über die SZE-Selektierung, das Südpol Teleskop, sowie den DES. Darüber hinaus enthält die Einleitung den theoretischen Hintegrund für die folgenden Kapitel. Das zweite Kapitel beinhaltet eine Analyse der Verteilung von Galaxienfarben, sowie der radialen Profile von Galaxien. Im Speziellen wird zwischen der gesamten Galaxienpopulation und der roten Galaxienpopulation, welche mit Hilfe einer Red-Sequence-Farbselektierung (RS) und Hintergrundsubtraktion identifiziert wird, unterschieden. Zur Bestimmung der Farbselektierung und zusätzlich zur Berechung photometrischer Rotverschiebungen verwende ich ein stellares Populationsmodell, basiered auf einem Sternentstehungsausbruch bei Rotverschiebung $z = 3$ und einem exponentiellen Zerfall von 0,4 Giga-Jahren. Dieses Modell beruht auf passiver Entwicklung der Galaxienpopulation. Ich unterteile das Sample in acht Rotverschiebungsintervalle mit ungefähr zahn Haufen in jedem Intervall. Ich schichte diese einzelnen Galaxienhaufen im Farben-Magnituden-Raum, um die Lage und Breite der Red-Sequence zu untersuchen. Es stellt sich heraus, dass die Lage und Steigung der Red-Sequence des Samples mit jener des Modells übereinstimmt. Es kann ein leichter Anstieg der intrinsischen Red-Sequence-Streuung bei höherer Rotverschiebung festgestellt werden. Die individuellen radialen Profile, sowie ihre geschichteten radialen Profile werden an ein Navarro-Frenk-White (NFW) Modell angepasst. Dadurch erhalte ich einen typischen Konzentrationsparameter 3.89 ± 0.52 für die gesamte Population und 5.47 ± 0.53 für die RS-Population. Diese Werte stimmen mit der gängigen Literatur überein. Die gesamte Population und RS-Galaxienpopulation weisen keine Rotverschiebungsentwicklung auf, jedoch ergibt sich eine Tendenz zu erhöhter Konzentration bei ansteigender Rotverschiebung. Ich verwende für die radialen Profile eine Parametrisierung mit N_{200}, der Anzahl an Haufengalaxien innerhalb der virialen Region. Aus diesen Bedingungen messe ich den Anteil an roten Galaxien im Haufen. Es zeigt sich eine schwache Entwicklung des roten Anteils bei ansteigender Rotverschiebung. Typischerweise sind $\sim 80\%$ der Galaxien bei Rotverschiebung $z = 0,1$ Teil der RS. Dieser Anteil sinkt auf $\sim 60\%$ bei

Rotverschiebung $z = 1$.
In Kapitel 3 beschäftige ich mich mit der Leuchtkraftfunktion (LF) des SZE selektierten Haufen-Samples und vergleiche sie mit der bekannten Schechter-Funktion. Es werden die drei typischen LF-Parameter hinsichtlich ihrer Abhängigkeit von der Haufenmasse und Rotverschiebung untersucht. In allen Analysen wird das optische Band, welches sich rechtsseitig des typischen 4000 Å break (einem spektralen Merkmal) befindet, verwendet. Ich mache von oben genannten Rotverschiebungsintervallen Gebrauch, um die Leuchtkraftfunktionen der einzelnen Haufen zu schichten. Dadurch ergibt sich die typische Steigung α am schwachen Ende der LF innerhalb jedes Rotverschiebungsintervalls. Diese Werte von α ermöglichen eine genauere Bestimmung der anderen zwei Parameter, nämlich der charakteristische Magnitude m^* und der Galaxiendichte ϕ^*. Die Ergebnisse zeigen, dass die charakteristischen Magnituden, sowohl der gesamten, als auch der RS-Population, mit jenen des passiven Entwicklungsmodell übereinstimmen. Die optischen Daten weisen auf eine signifikante Veränderung der hellen Galaxiendichte in Bezug auf die gesamte Population hin. Jedoch zeigt sich ein gegenläufiger Trend in der RS-Population. Dies impliziert eine Reduktion des Anteils an RS-Galaxien im Haufen und damit eine Transformation von blauen Haufengalaxien zu RS-Galaxien. Die Steigung der LF der gesamten Population ist signifikant steiler im Vergleich zur RS-Population. Auch hier zeigt sich eine schwache Entwicklung bei ansteigender Rotverschiebung.
Ich untersuche die Veränderung der Halo Occupation Number (HON), welche die Anzahl an Haufengalaxien repräsentiert. Die Massenabhängigkeit weist eine Steigung $\mu < 1$ auf, und ist somit vergleichbar mit den üblichen Werten der Literatur. Die Entwicklung der HON verläuft gleich zur charakteristischen Galaxiendichte. Die Übereinstimmung zwischen Modell und Daten dient der Berechnung des Anteils an stellarer Masse im Haufen. Die totale stellare Masse wird durch das Verhältnis von Masse zu Licht und der gesamten Leuchtkraft des Haufens berechnet. Für dieses SZE selektierte Sample ist der typische Anteil an stellarer Masse 0,85%. Es kann hierbei keine signifikante Abhängigkeit von Haufenmasse oder Rotverschiebung festgestellt werden. Im letzten Kapitel fasse ich meine Ergebnisse zusammen und zeige künftige Forschungswege auf.

Summary

This thesis presents a study of the galaxy populations in massive galaxy clusters that have been selected by the Sunyaev-Zeldovich Effect (SZE) from the South Pole Telescope. The sample comprises 74 galaxy clusters that have multiband optical imaging data taken in the Science Verification phase from the Dark Energy Survey (DES). The selection via the SZE signature gives a redshift independent approximately mass-limited cluster sample. Each of these clusters has a robust mass estimate that derives from the cluster SZE detection significance and redshift; these masses include corrections for SZE selection effects and account for the remaining cosmological uncertainties and unresolved systematics. With the deep data from DES these clusters cover a redshift range between 0 and ~ 1.1. This makes it an ideal cluster sample suited for studying evolutionary trends of the cluster galaxy population with mass and redshift. The first part of the thesis introduces the physics of galaxy clusters and characteristics of the cluster galaxy population. I present the SZE selection, the South Pole Telescope and the Dark Energy Survey. The introduction furthermore includes the theoretical framework of cluster physics.

I then analyze the optical properties of the SZE selected clusters in detail. Chapter 2 studies the color distribution of galaxies as well as their radial profiles. In particular, both the full galaxy population and the red galaxy population, identified using Red Sequence (RS) color selection together with statistical background subtraction, are examined. To enable the RS selection and to measure cluster photometric redshifts, a composite stellar population (CSP) model with a burst beginning at $z = 3$ and an exponential decay time of 0.4 Gyr is adopted. I divide the sample into 8 redshift bins with approximately 10 clusters in each bin, and stack them in color-magnitude space to examine the RS location and width. It turns out that the RS location and tilt of our cluster sample are in good agreement with this passive evolution model. There is evidence for the intrinsic scatter of the RS to mildly evolve with redshift. I fit the radial profiles of the cluster galaxy population as well as stacked profiles with a Navarro-Frenk-White (NFW) profile. Thus I recover characteric concentration parameters of 3.89 ± 0.52 for the full population and 5.47 ± 0.53 for the RS population, which is consistent with various literature studies. The full and RS population show no significant redshift evolution of the concentration parameter, although there is a tendency for the concentration to increase with redshift. Using the stacked radial profiles, we also present results on the blue non-RS galaxy population. The radial profile is parametrized in terms of N_{200}, the number of cluster galaxies within the virial region. From these constraints red fraction measurements are derived. There is a mild evolution of the red fraction with a typical decrease of $\sim 80\%$ at redshift 0.1 down to $\sim 60\%$ at redshift ~ 1.1.

In chapter 3 I study the luminosity functions (LF) of the SZE selected clusters, also probing for mass and redshift variation of the characteristic magnitude m^*, the characteristic density ϕ^*, and the faint end slope α. All analyzes take the band redward of the 4000 Å break. I use stacked LFs to determine the characteristic faint end slopes α within each redshift range. These α's allow one to better constrain the evolution in the other 2 parameters on a single

cluster basis. The characteristic magnitudes of the LFs for both the full and red populations evolve in good agreement with the passive evolution CSP model out to redshift ~ 1.1. The data support significant variation of the bright galaxy population density with redshift for the full population, but provide weaker evidence in the RS population. Together, these trends suggest that there is a reduction of the number density of luminous galaxies over time coupled with a transformation of the blue members of this population into RS galaxies. The faint end slope of the full population is significantly steeper than in the RS population. The data suggest a mild increase with redshift. I then examine the evolution of the Halo Occupation number (HON) with mass and redshift. The typical mass slope $\mu < 1$ is consistent with various literature studies. The redshift evolution of the HON follows the trend of the characteristic density ϕ^* suggesting a mild evolution in the red fraction with cosmic time. Finally, given the good agreement between our high redshift burst CSP model and our cluster sample, I use the mass to light ratios of the CSP model together with the luminosity measured from our cluster populations to estimate the total stellar mass within the virial region for each of our clusters. The typical SPT cluster stellar mass fraction is 0.85% showing no significant mass and redshift evolution.

In the concluding chapter, I provide a summary of the results presented in this Thesis and outline future directions of research.

List of Figures

1.1 Image compilation of the Coma cluster 4
1.2 Photometric redshift measurement for Planck clusters 14
1.3 Limiting Redshift for Planck cluster candidate 442 15
1.4 Cluster mass function 16
1.5 DES filter transmission curves 18
1.6 Hubble Diagram from distant Supernovae measurements 19
1.7 The large-scale redshift-space correlation function 21
1.8 HST image of the galaxy cluster Abell 2218 22
1.9 Cosmic Microwave spectrum 24

2.1 Scatter distributions in repeatability and stellar locus for DES 32
2.2 Completeness function for DES bands 34
2.3 Comparison of photometric and spectroscopic redshift measurements 36
2.4 Redshift distribution of the SPT cluster sample 37
2.5 Mass distribution of the SPT cluster sample 39
2.6 Effective filter transmission curves within 8 different redshift bins 41
2.7 Stacked color-magnitude distributions for 8 different redshift bins 42
2.8 Stacked color distributions for 8 different redshift bins 43
2.9 Evolution of the intrinsic width of the Red Sequence 44
2.10 Evolution of the concentration parameter for the full and Red Sequence population 47
2.11 Stacked Radial Profile of all clusters in the sample 51
2.12 Stacked Radial Profiles of clusters within 8 different redshift bins 52
2.13 Evolution of the Number of galaxies with mass and redshift 53
2.14 Evolution of the Red Fraction with redshift 55
2.15 Geometric illustration for calculating the effective area 61
2.16 Geometric illustration for distinct cases of star masking 62

3.1 Individual LF for 'El Gordo' (SPT-CLJ0102-4915) at redshift $z = 0.87$ 66
3.2 Contour plot of stacked LFs for full and RS population 68
3.3 Contour plot of stacked LFs for full and RS population continued 69
3.4 Optical image of galaxy cluster SPT-CLJ2351-5452 71
3.5 Optical image gallery of RS selected galaxies 72
3.6 Evolution of the characteristic magnitude 73
3.7 Evolution of the characteristic galaxy density 75

3.8 Evolution of the faint end slope 77
3.9 Evolution of the Halo Occupation Number 79
3.10 Evolution of the Mass-to-Light ratio 80
3.11 Evolution of the stellar mass fraction 82

List of Tables

2.1 Properties of the color stacks 40
2.2 Mass and Redshift Trends for the Radial Profile parameters $M_{piv} = 6 \times 10^{14} M_{\odot}$, $z_{piv} = 0.46$ 50
2.3 Individual best fit RP parameters 63
2.4 Individual best fit RP parameters continued 64

3.1 Composite Luminosity Function Parameters 70
3.2 Mass and Redshift Trends for the Luminosity function parameters $M_{piv} = 6 \times 10^{14} M_{\odot}$, $z_{piv} = 0.46$ 76
3.3 Individual best fit LF parameters 87
3.4 Individual best fit LF parameters continued 88
3.5 Individual best fit LF parameters continued 89
3.6 Individual best fit LF parameters continued 90

List of Notations

ACT Atacama Cosmology Telescope
AGN Active Galactic Nucleus
BAO Baryon Acoustic Oscillation
BCG Brightest Cluster Galaxy
CMB Cosmic Microwave Background
DES Dark Energy Survey
DESSV Dark Energy Survey Science Verification
H_0 Hubble constant
HOD Halo Occupation Distribution
HON Halo Occupation Number
ICM Intra-Cluster Medium
MCMC Monte Carlo Markov Chain
Ω_m mean matter density
Pan-STARRS Panoramic Survey Telescope & Rapid Response System
PS1 Pan-STARRS1
photo-z photometric redshift
ρ_{crit} critical density of the universe
RS Red Sequence
RMS Root Mean Square
SDSS Sloan Digital Sky Survey
SN Type Ia supernovae
SPT South Pole Telescope
SZ Sunyaev-Zel'dovich
SZE Sunyaev-Zel'dovich effect

Contents

Zusammenfassung **v**

Summary **vii**

List of Figures **x**

List of Tables **xi**

List of notations **xiii**

1 Introduction **1**
1.1 Components and observables of galaxy clusters 1
1.1.1 Galaxies 2
1.1.2 Intra-Cluster Light 3
1.1.3 Intra-Cluster Medium 3
1.1.4 Dark Matter 5
1.2 The color-magnitude-relation 9
1.2.1 The overall picture of galaxy formation 10
1.3 Optical cluster finders 11
1.4 Galaxy clusters as cosmological probes 16
1.5 The Dark Energy Survey 17
1.5.1 Supernovae Type Ia 17
1.5.2 BAO 19
1.5.3 Weak Lensing 20
1.6 The South Pole Telescope 23
1.6.1 The SZ effect 23
1.6.2 Observation and cluster detection within SPT 26
1.6.3 Optical follow-up 26

Optical properties of SZ selected clusters

2 Radial profiles and color distributions **29**
This chaper is a paper draft within internal review in DES
2.1 Introduction . . . 29
2.2 Observations and Data reduction . . . 31
2.2.1 DECam Data Processing and Calibration . . . 31
2.2.2 Star-Galaxy Separation . . . 33
2.2.3 Completeness Estimates . . . 34
2.3 Galaxy Cluster Properties . . . 35
2.3.1 Redshifts . . . 35
2.3.2 Cluster Masses . . . 38
2.4 Color Selection and Radial Profiles . . . 40
2.4.1 Red Galaxy Selection . . . 40
2.4.2 Radial Distribution of Galaxies . . . 47
2.4.3 Halo Occupation Number . . . 53
2.4.4 Red Fraction . . . 55
2.5 Discussion and Conclusions . . . 57
2.6 Appendix . . . 59

3 Luminosity function and Halo Occupation distribution **65**
This chaper is a paper draft within internal review in DES
3.1 Introduction . . . 65
3.2 Luminosity Function . . . 65
3.2.1 Method for Measuring Luminosity Function . . . 67
3.2.2 Composite Luminosity Functions . . . 68
3.2.3 Mass and Redshift Trends . . . 71
3.3 Derived Properties . . . 78
3.3.1 Halo Occupation Number . . . 78
3.3.2 Stellar Mass Fraction . . . 80
3.4 Discussion and Conclusions . . . 84

4 Final remarks **91**

Bibliography **95**

Curriculum vitae **105**

Acknowledgments **107**

Chapter 1

Introduction

Astronomy was revolutionized in the course of the 20th century. Early in the 1920s Edwin Hubble discovered and published a classification scheme of extragalactic nebulae (Hubble 1926). Soon it was realized that our parent galaxy the Milky Way was not unique in the Universe and that there are over 10^{11} more galaxies out there. This was one of the most exciting breakthroughs in the view of the current Universe. Hubble's second major discovery in 1929 was that the Universe is expanding. This was indicated by the relation between recessional velocity of galaxies and their distance (Hubble 1929), which showed that the Universe was smaller in the past. Thus Einstein's view of a static universe had to undergo a major paradigm shift. Some years later Fritz Zwicky demonstrated the existence of unknown dark matter (Zwicky 1937). In 1937 he applied the Virial Theorem to estimate the mass of the Coma galaxy cluster. Note that clusters of galaxies were already known back in 1781, when Messier realized that some galaxies he observed on the sky tended to be grouped or clustered (Messier 1781). Zwicky showed that the average galaxy mass determined using the Virial Theorem and the galaxy velocities that had been measured with redshifts, differed significantly from the mass expected given the galaxy luminosities. This provided evidence for an existing large amount of non-luminous mass. Our closest neighboring galaxy clusters, namely the Coma and the Virgo cluster became the most intensively studied clusters over time. Nowadays galaxy clusters are of the important probes to establish an understanding of the dynamical nature of the Universe.

1.1 Components and observables of galaxy clusters

Galaxy clusters are the largest gravitationally collapsed structures in the Universe. Their typical masses range from $10^{13} - 10^{15} M_{\odot}$ and their sizes comprise a few Mpc. They have velocity dispersions ranging from $800 - 1000 km/s$ and typical X-ray luminosities of $10^{43} - 10^{45} erg/s$. Typically they contain about 50 to 1000 member galaxies, which differentiates them from galaxy groups. An optical shape classification divides them into *rich* and *poor* clusters, as well as *regular* and *irregular* systems. *Regular* clusters have (in contrast to *irregular* clusters) a spherical shape with a central high density region.
Phenomenologically they are made up of the following four components:

1.1.1 Galaxies

Clusters are unique places in the Universe to study galaxy populations because they provide a volume-limited galaxy sample compared to the field galaxy distribution. These galaxies contain baryonic matter in form of stars and cold gas. Although in the early times the galaxies were used to identify clusters, their total mass constitutes only about $2-5\%$ of the total cluster mass. The cluster population is made up of old (red and dead) galaxies, which already ended their star formation, as well as blue galaxies that are still actively star-forming. The observation of cluster galaxy populations differ from those in the field. Spitzer & Baade (1951) and Gunn & Gott (1972) concluded that there might be dynamical processes within a cluster that are responsible for transforming spiral galaxies into S0's and elliptical galaxies. In 1974 Oemler found that the cluster population behaved as a function of the cluster structure in general, as well as the location of the individual galaxy within the cluster (Oemler 1974). This means that dynamically relaxed clusters (which have a *regular* appearance) have large elliptical and SO (so called "early-type" galaxies) populations compared to the spiral galaxy component (so called "late-type" galaxies). Furthermore these clusters exhibit a population gradient with early-type galaxies becoming more numerous towards the center of the cluster. In contrast *irregular* clusters have much more spiral rich galaxy populations with no signs of significant radial population gradients. Some years later, Dressler (1980) established the well known *Morphology-Density-Relation* with a sample of thousands of galaxies inside low redshift galaxy clusters. This relation correlates the morphological type of an individual galaxy to the cluster properties and its spatial distribution. Similar to Oemler, Dressler found no sign of a radial galaxy type segregation inside *irregular* galaxy clusters. Both Oemler's and Dressler's picture of cluster populations hint to important environmental effects inside clusters that can alter the galaxy populations.
Moreover the galaxy population can be regarded as a mass tracer for the average galaxy cluster mass. A precise knowledge of the cluster mass is important for several astrophysical and cosmological questions (Schindler 1996). As an example, the derivation of gravitational mass profiles (e.g. from X-ray observations) is crucial for conclusions about dark matter in clusters. Another important parameter that relies on the precise determination of the gravitational mass is the gas mass to total mass ratio (ibid.). The baryon to dark matter ratio can help to constrain primordial nucleosynthesis models in cosmological simulations. Furthermore the cluster mass function can be used to constrain the power spectrum of the primordial density fluctuations. All these applications rely on a precise determination of the cluster mass.
When spectroscopic data are available, a direct cluster mass measurement can be done with the help of velocity dispersions. The underlying assumption is that galaxies act as collisionless particles and trace the clusters gravitational potential. Saro et al. (2012) conclude that the mass measurement with velocity dispersions can be used for a precise calibration of a cluster survey Mass - Observable relation. The scatter in mass has been found as $\sigma_{lnM} \sim 0.15$. Another cluster mass estimator is the optical cluster richness. Today's generation large optical surveys, like the DES or Pan-STARRS, are expected to generate galaxy catalogs with thousands of clusters having sufficiently deep optical data. A well constrained richness-mass relation can be then used to place tight constraints on cosmological parameters. Yet the scatter in mass at a fixed richness has been still quite noisy with $\sigma_{lnM} \sim 0.45$ (Rozo et al.

2009) based on the maxBCG cluster catalog, an optically selected cluster sample drawn from SDSS imaging data. A robust richness estimator with low scatter is still under development, but already improvements have been made to reduce the scatter to $\sigma_{lnM} \sim 0.2 - 0.3$ (Rykoff et al. 2012).

1.1.2 Intra-Cluster Light

Intra-cluster Light (ICL) is defined as optical light from stars that are gravitationally bound to the cluster potential, but not bound to cluster galaxies. Yet the properties of the ICL remain less well-determined and understood than the other cluster components. The following formation scenarios have been suggested (DeMaio et al. 2015): (1) the disruption of dwarf galaxies as they fall into the cluster potential, (2) the tidal stripping of the outskirts of L^* galaxies, (3) violent relaxation after major mergers between galaxies, including the central Brightest cluster galaxy (BCG), and (4) in situ star formation. The formation of ICL is closely related to the evolution of the BCG. Simulation and observational studies show that ICL can make up a significant fraction of the total cluster stellar content ranging from $10 - 40\%$ (Contini et al. 2014). Probing ICL may not only help us understand how BCGs evolve over time, but also stimulate knowledge about cluster dynamics and galaxy evolution in general.

1.1.3 Intra-Cluster Medium

The ICM consists mainly of hydrogen and helium and makes up between $11 - 15\%$ of the total cluster mass. It represents the ionized low-density form of the baryonic matter of galaxy clusters in contrast to the galaxies. Typical electron number-densities are on the order of $n_e \sim 10^{-4} - 10^{-2} cm^{-3}$. On large scales the gas is stably stratified and the density is decreasing with radius. The gas extends out to radii of the order of $\sim 1 Mpc$ (Sarazin 2008). The ICM reaches temperatures between $10^6 - 10^8 K$ in order to balance the gravitational pull of the potential well. At these high temperatures, the gas emits X-ray radiation. The physical processes here are collisional: we can distinguish between thermal *Bremsstrahlung* as free-free emission, recombination processes as free-bound emission and line radiation transitions as bound-bound emission. As the emissivity of the radiation scales with the square of the gas number-density, it is largest in the cluster core. As a result, clusters of galaxies are generally strong and luminous X-ray emitters with typical luminosities of the order of $L_x \sim 10^{43} - 10^{45} ergs/s$. An optical and X-ray image compilation of the Coma cluster can be seen in Figure 1.1.
The ICM has various other interesting physical mechanisms: It confines and distorts radio galaxies within the cluster core. The cosmic ray and magnetic field components of the ICM can furthermore produce diffuse radio emission (Sarazin 2008). Another process occurs especially in the center of clusters: Galaxies passing the core can be stripped off interstellar gas by the ICM. There happen to be radiative energy losses in the cores of galaxy clusters on timescales significantly shorter than the age of the system (e.g. Cowie & Binney 1977). With-

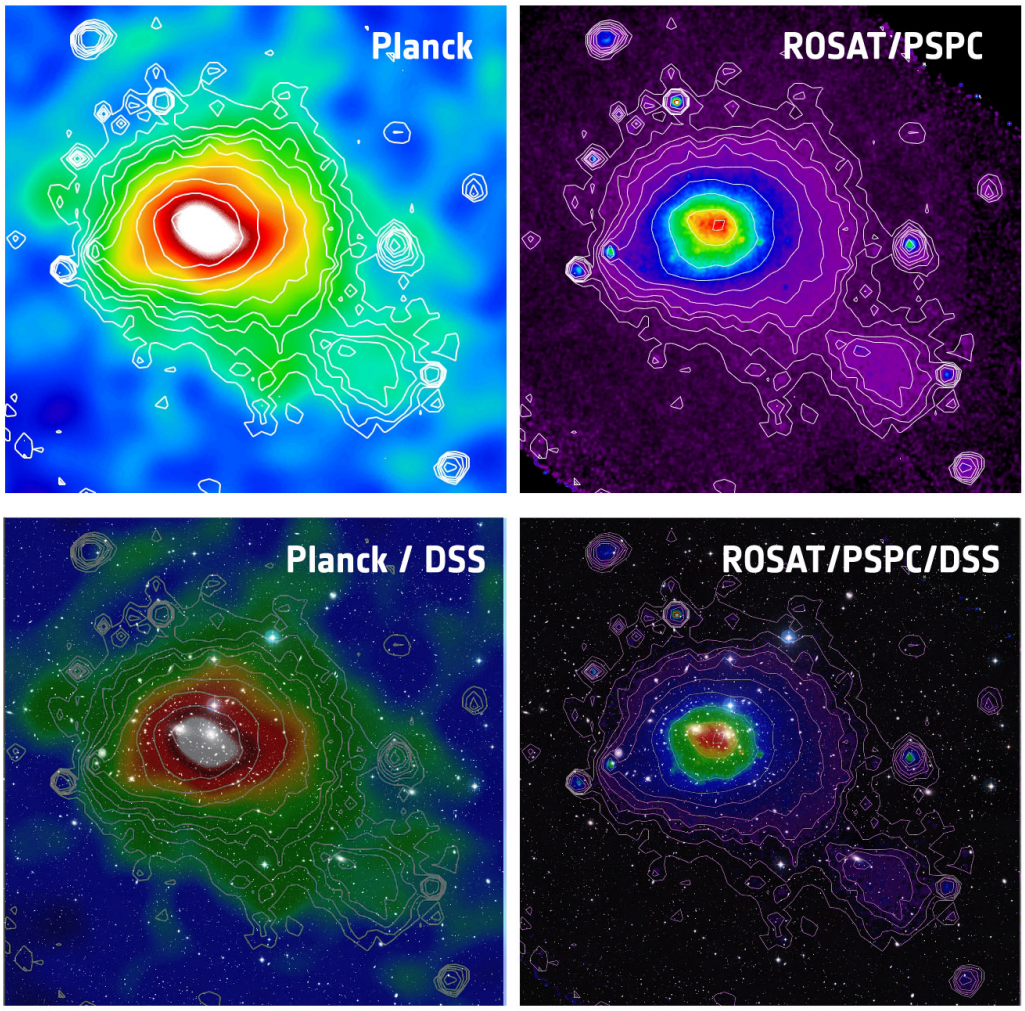

Figure 1.1 The top-left panel shows the SZ image of the Coma cluster produced by Planck, whereas the top-right panel shows the same cluster imaged in X-rays by the ROSAT satellite. In the two lower panels the SZ and X-ray image are overlayed with the optical image of the Coma Cluster from the Digitised Sky Survey. (Copyright: Planck image: ESA/ LFI and HFI Consortia; ROSAT image: Max-Planck-Institut fuer extraterrestrische Physik; DSS image: NASA, ESA, and the Digitized Sky Survey).

out compensation, this cooling would lead to a massive accumulation of cold gas in the cluster center and thus trigger vigorous star formation rates. However this expected significant star formation has not been justified by observations (e.g. Peterson & Fabian 2006). A promising explanation of a compensation of the energy loss has been heating by the supermassive black holes in the central cluster galaxies. Zhuravleva et al. (2014) presented a different plausible solution to this problem by analyzing Chandra X-ray observatory data. They found that

turbulent heating is sufficient to offset radiative cooling and appears to balance it locally at each cluster radius.
Like the richness of the cluster, the X-ray observables also provide a mass proxy. For example Arnaud et al. (2007) use the quantity Y_x (the product of the X-ray temperature and gas mass) as a robust low-scatter mass proxy for galaxy clusters. They find a scaling relation of $M \propto Y_x^{\alpha}$ with $\alpha = 0.548 \pm 0.027$, close to self-similar evolution. For the purpose of well constrained cosmological analyses the calibration of such scaling relations and low-scatter mass proxies is crucial. A further characteristic feature of the ICM, namely the Sunyaev-Zeldovich Effect will be discussed in detail in Section 1.6.1.

1.1.4 Dark Matter

Dark matter (DM) is a hypothetical form of mass that makes up $80 - 87\%$ of the total mass of galaxy clusters. Dark Matter cannot be directly measured or detected, yet its existence can be inferred from gravitational effects on visible baryonic matter or radiation. It is called dark matter as it does not emit nor absorb electromagnetic radiation.
Historically Oort (1932) was the first to discover the presence of an unknown matter in the Milky Way. He studied the stellar motions in the galactic neighborhood and calculated the velocities from Doppler shifts. Since he knew that the Milky Way was not flying apart, he realized that there had to be much more matter in the Galaxy then it was measured from the visible light. While Oort was carrying out his stellar motion measurements, Zwicky (1937) discovered the presence of dark matter on a much larger scale through his studies of galactic clusters. Shortly after Zwicky, Babcock (1939) analyzed the rotation curve of the Andromeda galaxy and found that it was flat out to large radii. This result was highly counterintuitive since, based on Newton's law of gravity, the rotational velocity would constantly decrease further away from the galactic center. An explanation for this flat rotation curve was the presence of unknown dark matter that speeds up the outer stars inside the galaxy. It was then generally accepted, that DM would have to be located in a massive, roughly spherical halo surrounding each galaxy.
Yet the nature of DM is still unsolved. Early speculations on the nature of DM encompassed massive compact halo objects (called MACHOs). These are for example supermassive black holes, neutron stars, white and brown dwarfs or ultra-faint dwarfs. Thus DM would consistent of hidden baryonic matter, which was complex to detect. Yet observational evidence proofed that this category of objects could contribute not enough mass to the total mass (Freese et al. 2000). Faint stars and brown dwarfs constitute only a few percent of the mass of the Galaxy and stellar remnants, including white dwarfs and neutron stars, are also insufficient in abundance to explain all the needed DM. As it was shown by the analysis of rotation curves or gravitational lensing, DM does not interact with the electromagnetic force. Consequently, this form of matter had to be non-baryonic. Today's view is that DM is made up of unknown elementary particles that were called WIMP's (Weakly Interacting Massive Particles). This generation of particles included neutralinos, axions, or sterile neutrinos. Several more particles have been proposed.
Dark matter candidates are in general divided into three classes, called cold, warm and hot dark matter (Schaeffer & Silk 1988). These adjectives are misleading as they do not refer to

the actual temperature of the DM, but rather to their speed of moving. Today, cold dark matter is the easiest explanation for most cosmological observations. It is composed of particles or candidate objects with a free-streaming length that is smaller than the scale of a proto-galaxy. Hot dark matter does not seem to be reasonably applied to galaxy formation, as well as cluster formation. Warm dark matter includes particle candidates with a free-streaming length comparable to the size larger than a proto-galaxy. Thus it is comparable with the size of a dwarf galaxy. Using warm dark matter can lead to cosmological predictions similar to cold dark matter on large scales. Yet it implies less density perturbations on small scales which will lead to a reduced number of dwarf galaxies.

Although the constitution of DM is still unresolved, the structure of DM haloes is well described. Navarro et al. (1996) used N-body simulations to examine the structure of DM halos in the cold DM cosmology scenario. The halos studied had a mass range from dwarf galaxy size up to cluster size. This comprises four orders of magnitude in mass. The generated spherically density profiles were well fitted by a "universal" profile called the Navarro-Frenk-White (NFW) profile. It is a two-parameter function that holds over a wide range of masses. The three-dimensional form is the following:

$$\frac{\rho(r)}{\rho_{crit}} = \frac{\delta_c}{x(1+x)^2} \tag{1.1}$$

Here $x = r/r_s$ is the radial coordinate parametrized in units of the profile scale radius r_s. The scale radius itself is a characteristic radius and can be written as $r_s = R_{200}/c$, where R_{200} is the virial halo radius where the halo-density reaches 200 times the critical density of the Universe. c is the concentration parameter of the profile. δ_c is a dimensionless parameter and can be written in terms of the concentration with

$$\delta_c = \frac{200}{3}\frac{c^3}{[ln(1+c) - c/(1+c)]} \tag{1.2}$$

It represents the characteristic over-density of the halo. The profile flattens towards the halo center but does not have a flat core. Cole & Lacey (1996) have shown that this universal profile provides excellent fits also to halos formed in other cosmogonies or from density fluctuations described by a variety of power-law perturbation spectra. Thus the NFW profile is not only restricted to cold DM as originally used in Navarro et al. (1996). Bartelmann (1996) de-projected the three-dimensional profile into two-dimensional space. The surface mass density can be written as

$$\Sigma(x) = \frac{2\rho_s r_s}{x^2 - 1} f(x) \tag{1.3}$$

Here $\rho_s = \delta_c \rho_c$ and $f(x)$ is given as:

$$f(x) = \begin{cases} 1 - \frac{2}{\sqrt{x^2-1}} arctan\sqrt{\frac{x-1}{x+1}} & \text{if } x > 1, \\ 1 - \frac{2}{\sqrt{1-x^2}} arctanh\sqrt{\frac{1-x}{x+1}} & \text{if } x < 1 \\ 0 & \text{if } x = 1 \end{cases}$$

Nagai & Kravtsov (2005) discuss the problem of the strong degeneracy between the concentration parameter and the normalization of the profile ρ_s. They suggest a re-expression of the amplitude in terms of the total number of galaxies contained within the virial cylinder, where the degeneracy can be reduced. The total number is simply an integral of the projected surface density and can be written as:

$$N_{cyl}(r) = \int\int \Sigma(x) d\theta dx = \int\int \frac{2\rho_s r_s}{x^2-1} f(x) r dr d\theta = \int 2\pi \frac{2\rho_s r_s}{x^2-1} f(x) x dx$$
$$N_{cyl}(r) = 4\pi\rho_s r_s^3 \int \frac{x}{x^2-1} f(x) dx$$

Solving the integral and assuming the radius is parametrized in units of R_{200}, we get the part-wise defined functional form

$$N_{cyl}(r) = 4\pi\rho_s r_s^3 \begin{cases} \frac{2}{\sqrt{(cr)^2-1}} arctan\sqrt{\frac{cr-1}{cr+1}} + ln(\frac{cr}{2}) & \text{if } x > 1, \\ \frac{2}{\sqrt{1-(cr)^2}} arctanh\sqrt{\frac{1-cr}{1+cr}} + ln(\frac{cr}{2}) & \text{if } x < 1 \\ 1 + ln(\frac{cr}{2}) & \text{if } x = 1 \end{cases}$$

Given a parametrization of the radial coordinate in terms of the virial radius R_{200}, the total number of galaxies within the virial cylinder is simply a function of the concentration c, namely:

$$N_{cyl}(R_{200}) = 4\pi\rho_s r_s^3 \begin{cases} \frac{2}{\sqrt{(c)^2-1}} arctan\sqrt{\frac{c-1}{c+1}} + ln(\frac{c}{2}) & \text{if } x > 1, \\ \frac{2}{\sqrt{1-(c)^2}} arctanh\sqrt{\frac{1-c}{1+c}} + ln(\frac{c}{2}) & \text{if } x < 1 \\ 1 + ln(\frac{c}{2}) & \text{if } x = 1 \end{cases}$$

As shown, the NFW profile has a fixed shape and can be parametrized by just two variables, that is the virial radius and a characteristic density. An equivalent description can be obtained with the virial halo mass and the concentration parameter. The spherically integrated mass inside the radial coordinate $r = xr_s$ can be written as (e.g. Coe 2010)

$$M(r) = 4\pi r_s^3 \int x^2 \frac{\rho_s}{x(1+x)^2} dx =$$
$$= 4\pi r_s^3 (ln(1+x) - \frac{x}{1+x})$$

Thus again within the virial sphere the mass is simply a function of the concentration c. Investigations into dark matter halo dynamics are pushed forward due to large-scale cosmological N-body simulations. Duffy et al. (2008) used a set of N-body simulations from the *Millennium Simulation* (Springel et al. 2005). Within this simulation a large number of Dark Matter particles were allowed to interact gravitationally inside a huge cosmological box. Duffy et al. (2008) analyzed the relation between the mass of the dark matter halo and its given concentration by fitting density profiles. Their simulated halos span four orders of magnitude in mass and redshift and are well described by a simple power law relation in mass

and redshift of the form

$$c_{200} = (5.71 \pm 0.12)(\frac{M_{200}}{M_{pivot}})^{-0.084\pm0.006}(1+z)^{-0.47\pm0.04}$$

for a pivot mass of $M_{pivot} = 2 \times 10^{12} h^{-1} M_{\odot}$. An alternative model, in particular the Einasto profile (Einasto 1965), was shown to represent the dark matter profiles of simulated halos as well. The Einasto profile is described by a power-law form with

$$\frac{dln\rho}{dlnr} = -2(\frac{r}{r_{-2}})^{\alpha}$$

Here r_{-2} is the radius at which the logarithmic slope of the density is isothermal, which is analogous to the scale radius r_s of the NFW profile. Duffy et al. (2008) found that Einasto concentrations decrease significantly more rapidly with both mass and redshift, compared to the NFW concentrations. Independent of the model profile, the conclusion is that the concentration is decreasing as a function of redshift and mass. This means that more massive haloes have higher concentrations than less massive halos.
However when comparing to observations there are still some discrepancies:
A recent study of Rasia et al. (2013) analyzed possible reasons for the observed discrepancy between X-ray concentration-mass relations and the ones predicted from DM only simulations. Given that DM is the dominant contributor to the total halo mass, one would naively think that simulations with only dark components properly describe the halo properties. Yet the X-ray observational results of Schmidt & Allen (2007) and Ettori et al. (2010) show significant differences in the normalization and mass-slope of the $c - M$ relation. Schmidt & Allen (2007) used a sample of 34 massive, dynamically relaxed galaxy clusters, spanning the redshift range $0.06 < z < 0.7$. These observed profiles were fit by an NFW model. The resulting $c - M$ relation turned out to be significantly steeper in the mass-slope. Ettori et al. (2010) used 44 X-ray luminous galaxy clusters observed with XMM-Newton in the redshift range $0.1 - 0.3$. They find an even steeper mass slope as well as a lower power-law normalization than the DM prediction from Duffy et al. (2008). Assuming the hierarchical scenario of structure formation in the Universe is valid, then smaller halos form at an early time in the Universe (Rasia et al. 2013). Over cosmic time, the accumulation of material at the center happens in an already-established high-density peak. In this way, an increasing concentration with time is expected by theory. It is not surprising then, that X-ray observations have proofed this decreasing trend with redshift. Yet the values differ significantly. Thus the question is: Are these differences real or artificial. To answer that Rasia et al. (2013) considered various aspects in the profile generation and the fitting procedure:
The main difference between observations and simulations is the limitation of the volume. While in simulations one can analyze the full profile from the center to the halo outskirts (including ALL particles, such as sub-clumps and sub-structures), observations are volume-limited, sometimes to a narrow radial range due to the Field-of-view of the telescope (ibid.). Furthermore the selection function of the halos is done in mass for the simulations, while it depends on "noisier" observables (such as X-ray luminosity) in most observational studies. Yet the most obvious difference is the inclusion of baryons. The influence of baryonic physics on the DM distribution was already been described by the model of 'adiabatic contraction'

in Blumenthal et al. (1986). It describes the contraction of a dark matter halo in response to condensation of baryons in its center. Consequently the DM is influenced by the extra baryonic matter in the potential well of the cluster center, that has been accreted. Later on Duffy et al. (2010) also included ICM physics into their simulations, such as radiative cooling and feedback mechanisms.
Rasia et al. (2013) also used a set of DM simulations including DM only, non-radiative physics as well as cooling physics and Star-formation and feedback mechanisms. Then they analyzed different radial ranges in the NFW fitting procedure, selection function biases as well as the different baryonic physics.
Concerning the radial range, they find an increase in the mass-slope and normalization of the $c - M$ relation when reducing the fitting range from the outskirts of the cluster close to the virial radius R_{200} down to cluster center regions. These changes are mild for the DM-only simulations, yet they are significant with baryonic physics included (changes in the mass-slope up to 100%, ibid.). Concerning selection effect they note that selecting clusters via their X-ray luminosity can introduce biases towards a higher normalization and slope contrary to the ones from the mass-selected DM simulations. Examining the different physics, baryonic simulations have always a larger normalization than those from the DM halos (ibid.). Star-formation and feedback simulations are characterized by steeper and higher $c - M$ relations, yet the inclusion feedback of Active Galactic Nuclei (AGN) physics reduces it again.
As a conclusion, it will be essential to carefully study selection biases and the overall effects of baryons on the halo concentrations.

1.2 The color-magnitude-relation

Early-type galaxies represent the dominant population in the centers of galaxy clusters with very few exceptions out to a redshift of ~ 1. The uniformity of their galaxy properties helps to constrain the cluster formation and evolution.
The first discovery of a tight correlation between color and magnitude for field elliptical galaxies was noted in Baum (1959). His findings suggested on the one hand that the colors for elliptical galaxies become bluer as they become less luminous and on the other hand that early-type galaxies are the reddest at a single redshift. This means that elliptical (early-type) galaxies form a red sequence (RS) in color-magnitude space with a well defined slope and small scatter. The color-magnitude-relation (CMR) shows a bimodal distribution with a tight RS and a more diffuse "blue cloud", which represents the late-type emission line galaxies. Later on this relation was also found in the well studied galaxy clusters Coma and Virgo by Bower et al. (1992). In addition to low redshift clusters, the study of Ellis et al. (1997) proofed the existence of the RS in clusters at redshift of ~ 0.54. This was also shown in Kauffmann & Charlot (1998), where they used hierarchical models of galaxy formation, and found that the models predict a substantial population of "evolved" ellipticals and a RS out to redshift $z \sim 1$. At that time the existence of the RS was explained with age and metallicity effects. Specifically, the existence of the RS at higher redshifts indicates that cluster elliptical galaxies are a passively evolving population in which the reddening of massive galaxies is the result of an underlying mass-metallicity relation. It indicates that star formation has been reduced,

or quenched, for most early-type galaxies. This gives an important clue to their evolution. A passive evolution of elliptical galaxies can be modeled with galaxies forming in a monolithic collapse at high redshift and then evolving passively after this initial starburst (Gladders et al. 1998). The origin of a mass-metallicity relation for the RS was explained the following (e.g Arimoto & Yoshii 1987): The heating of the interstellar medium from supernovae in the initial starburst is supposed to trigger the formation of a galactic wind. This happens when the thermal energy of the gas exceeds the gravitational binding energy. As low-mass galaxies have a shallower potential compared to high-mass galaxies, any galactic winds can eject gas more efficiently in low mass galaxies. This then results in a trend of increasing metallicity with mass, as the more massive galaxies are more likely to retain the enriched supernova ejecta. Due to this mass-metallicity relation, early-type galaxies of different masses can show slightly different colors with age. Coming back to a scenario of early type galaxy formation due to a monolithic collapse, this would cause a change in the slope of the RS with redshift. Precisely the expected slope of the RS at higher redshift (closer to the age of formation) is flatter compared to later times at lower redshift. Kauffmann & Charlot (1998) also provided an alternative origin of the slope of the RS. Using simulations they concluded that elliptical galaxies are formed hierarchically through merging processes. A mass-metallicity relation is used for the progenitor disk-like systems that have been already pre-enriched. Thus massive elliptical galaxies tend to form from the disk systems in hierarchical merging, building up a mass-metallicity relation for the early-type galaxies. Similar to Arimoto & Yoshii (1987) the RS is expected to have a shallower slope at high redshifts and steepening over cosmic time. This is due to the fact that the stellar populations in massive elliptical galaxies are on average younger and become bluer relative to low-mass systems as the formation epoch is approached (Gladders et al. 1998).
As a consequence the gradient of the slope of the RS with redshift can be used to gain knowledge on the formation epoch of the dominant stellar populations in early-type galaxies.

1.2.1 The overall picture of galaxy formation

As already mentioned in the current ΛCDM cosmological model, galaxies form via the hierarchical gravitational collapse of dark matter fluctuations. The cluster formation occurs on the peaks of these density fluctuations and they accrete surrounding groups and field galaxies. The dominant cluster population, namely the early-type galaxies, has formed in the dense dark matter cores and formed most of its stellar mass in a early short event of star formation (e.g. De Lucia & Blaizot 2007). This pristine galaxy population that formed in the cluster core represents one part of the RS inside clusters. The other part includes galaxies that migrate onto the RS over cosmic time. Two main processes appear responsible for building up the RS (Mei et al. 2009) over time: First, quenching of star formation in galaxies in the blue cloud, and second, merging of less luminous red galaxies. Observationally there has been a decrease in the S0 galaxy population seen in high redshift clusters (e.g. Postman et al. 2005; Desai et al. 2007). In many clusters it was found, that the galaxy population gradually develops a red, evolved, early-type population in the inner part of the clusters and a blue, later-type population in the extensive outer cluster envelope (e.g. Fujita & Goto 2004).

These observations suggest that the blue, normal spirals observed in high-redshift clusters were originally field galaxies. Over cosmic time they fell into clusters and evolved into the non-blue S0 galaxies observed in nearby clusters. Infalling galaxies onto the cluster potential have undergone quenching and a morphological transformation, thereby migrating onto the RS, most likely as S0 galaxies. There have been several mechanisms proposed that can lead to a morphological transformation and star-formation quenching for infalling field galaxies or even blue cluster member galaxies: galaxy mergers, tides from the cluster potential (e.g. Fujita 1998), tidal interactions between galaxies, ram-pressure stripping (e.g. Gunn & Gott 1972) or strangulation, which represents a gradual decline in the star-formation rate due to stripping of halo gas (e.g. Kodama & Bower 2001). Most of the morphological transformation and star formation quenching is thought to occur at redshifts $z < 1.0$, yet we do not fully understand their significant roles in the assembly of galaxy clusters and galaxy evolution.

1.3 Optical cluster finders [1]

The RS is a powerful tool to estimate photometric redshifts of galaxy clusters and can be used for cluster finding. The efficiency of using the RS as a cluster finding tool is due to two reasons: First, early-type galaxies inhabit a significant feature in their spectra, that is the 4000 Å break. This spectral feature provides the largest signal for photometric redshift estimation. By already pre-picking the reddest galaxies in a color-magnitude diagram, one only needs a single color to estimate a photometric redshift. The prerequisite is that this single color brackets the 4000 Å break. The second advantage is, that the RS (compared to the blue galaxy population) is composed of many red galaxies with a similar color. Hence when using a whole sequence instead of single spread galaxies, the measurement uncertainty becomes smaller (Yee et al. 1999). These galaxies are typically the brightest cluster galaxies and they are spatially clustered. Cluster finding based on the RS method has been successfully applied in various studies (e.g. Yee et al. 1999; Rykoff et al. 2014; Koester et al. 2007; Gladders & Yee 2005). Different optical cluster finder algorithms have been developed and can be applied to wide-field, multi band digital imaging surveys such as SDSS, Pan-STARRS and DES. Exploiting the typical properties of the RS galaxies can enable the generation of large, high-quality and highly complete cluster catalogs, whose selection function can be quantitatively determined (Koester et al. 2007). The RS method can be even applied on low richness group scale systems.
Rykoff et al. (2014) described the challenges in an optimal optical cluster finder:
– The algorithm has to detect galaxy clusters in a consistent way across a large redshift range. One has to be aware that at high redshifts the photometric uncertainties at faint magnitudes become larger and can cause biases. As the color for photometric redshift estimation has to bracket the 4000 Å break, one would need complementary near-infrared data as one explores redshifts above $z \sim 1$.
– The algorithm should include a spectroscopic training set to establish the quality of the photometric redshift measurement.

[1] This section includes a summary of the published paper Liu et al. (2015), where the author of this Thesis contributed as a Second-Author.

– The algorithm should be efficiently run on large survey datasets, covering nearly the full sky.
– The algorithm has to account for complex survey masks, such as bright stars, satellite trails or imaging artifacts. Also varying survey depth has to be taken into account.
– The algorithm should be tested for "false positive" contamination, e.g. on blank fields. Thus also large scale structure studies can be enabled.
– Offsets of the cluster center (such as X-ray or BCG or SZ centers) need to be modeled.

Most of these criteria have been fulfilled in a recent analysis by Liu et al. (2015). In this study we report results of an analysis of Planck SZE selected cluster candidates using Pan-STARRS optical data. The Planck SZE selected source catalog (Planck Collaboration et al. 2014) includes 1227 cluster candidates in total, where 366 are still unconfirmed cluster candidates. The SZ effect is a spectral distortion due to inverse Compton scattering of the CMB photons with the hot electrons from the ICM and will be described in more detail in Section 1.6.1. For detection of these SZE sources from the Planck CMB data, there exist 3 optimized pipelines with multi-frequency matched filter approaches (Melin et al. 2006). Given the measured purity of the Planck Survey with 83.7% (Planck Collaboration et al. 2014), there will be 200 expected noise fluctuations out of the remaining 366 unconfirmed candidates. The Planck Satellite has full-sky coverage and thus there is not a single survey available at present to provide full optical follow-up data. The Pan-STARRS survey footprint contains in total 237 unconfirmed candidates. For each candidate, we had the following supplementary information available: the coordinate position in degrees, the positional uncertainty, the best estimated angular size and the integrated SZE signal Y_{SZ}. The angular size had been converted to Θ_{500} using a concentration of $c_{500} = 1.177$ as described in the detection pipelines (Planck Collaboration et al. 2014). We note that this angular radius is the representation of the projected physical radius R_{500}, where the density is 500 times the critical density of the Universe.
For each cluster candidate we downloaded the single epoch detrended images from the Pan-STARRS data server and used those data to build deeper coadd images in each of the 4 optical bands g, r, i, z. This process includes cataloguing the single epoch images, inferring a relative calibration, combining them into coadd images and then finally cataloguing the coadds.
These multi band optical data with a median depths of 20.6, 20.5, 20.4 and 19.6 ($[g, r, i, z]$ respectively) are well suited for an optical cluster confirmation and photometric redshift estimation. In particular we used the RS galaxy over density in color-magnitude space that is correlated with the galaxy cluster population to identify an optical counterpart for the Planck candidates. Comprised is also the estimation of a photometric redshift. The full method is similar to the one that has been successively used in Song et al. (2012a). Instead of using a fixed search aperture, we applied a mass-observable-relation derived from SZE to calculate the cluster mass and characterized the scale of the virial region within which the red sequence search was carried out. In order to compare our data to a theoretical prediction, we modeled the evolutionary change of the color of cluster member galaxies by a composite stellar population model (Bruzual & Charlot 2003). This model has its initialization at a formation redshift of $z = 3$, followed by an exponential decay of $0.4Gyr$. The tilt of the RS is introduced with

6 models with different metallicities adjusted to follow the observed luminosity-metallicity relation in Coma galaxies. With the Pan-STARSS optical filter transmission curves we generated fiducial galaxy magnitudes in the 4 different bands and over a redshift range between 0 and 1.2 (Note that given the above mentioned depths of the Pan-STARRS survey, only a maximum redshift of 0.7 was probed). A local background annulus was used for statistical background subtraction. Then each galaxy within the radial search aperture was assigned two different weighting factors. These account for the consistency of the galaxy color with the model color at the redshift probed, and for the cluster centric distance. In this way, all galaxies physically close to the cluster center and with colors consistent with the red sequence at the redshift being probed are given higher weight. Conversely any galaxies in the cluster outskirts with colors inconsistent with the red sequence are given a small weight. For each cluster candidate we built histograms of the weighted number of galaxies as a function of redshift for the different color combinations tracing the 4000 Å break. The basic principle is that each object in an input galaxy catalog is assigned a likelihood that it is part of the RS at a certain redshift. This procedure was repeated on an array of redshifts, producing a photometric redshift -likelihood distribution. The peak of the likelihood in redshift space can be read off as the cluster redshift. We identified 3 distinct cases, where our method failed to estimate a reliable photometric redshift. Either the search aperture from Planck is too small, too large, or if there is a relatively large offset between the visually confirmed cluster centre and the Planck position. A validation sample of ~ 150 confirmed clusters was used to test the photometric redshift estimation. The performance of this method can be seen in Figure 1.2. After removal of the failures and the questionable clusters identified in Rozo et al. (2014), we were left with 135 Planck clusters. The RMS scatter of the full validation spectroscopic cluster sample is 0.023. Further discussion of the method and outlier fraction can be seen in Liu et al. (2015). As noted above, random superposition of groups or structures is one source of contamination in a photometric redshift analysis. Given the large search radius (compared to a fixed small aperture), the chance is high to associate a massive Planck cluster from the SZE detection towards a lower mass optical system in the fore- or background. Thus the cluster confirmation method has been successively tested on 60 random fields on the sky with a low contamination rate of 3%.

For cluster candidates, where we were not able to estimate a photometric redshift, there is the possibility that the candidate is a pure noise fluctuation, or the Pan-STARRS data are not deep enough to find it. Thus, for each of these undetected systems we calculated the minimum redshift limit beyond which the candidate would be undetectable in the Pan-STARRS imaging. In particular, for each of the unconfirmed systems we calculated the minimum redshift for a $10^{15} M_{\odot}$ cluster, beyond which the candidate would be impossible to detect in Pan-STARRS optical data. Therefore a model for the Halo Occupation Number for red galaxies is used to compute at each redshift the given number of red galaxies. This model reads:

$$N_{red}(z) = [1 + V\phi^*(z) \int y^{\alpha} e^{-y} dy] \times f_r(z) \tag{1.4}$$

where $\phi^*(z)$ is the characteristic number density of galaxies, α is the faint end slope, $y = L/L^*(z)$, where $L^*(z)$ is taken from the passive evolution model described above and V is the virial volume. We integrated down to the luminosity limit determined from the catalogue

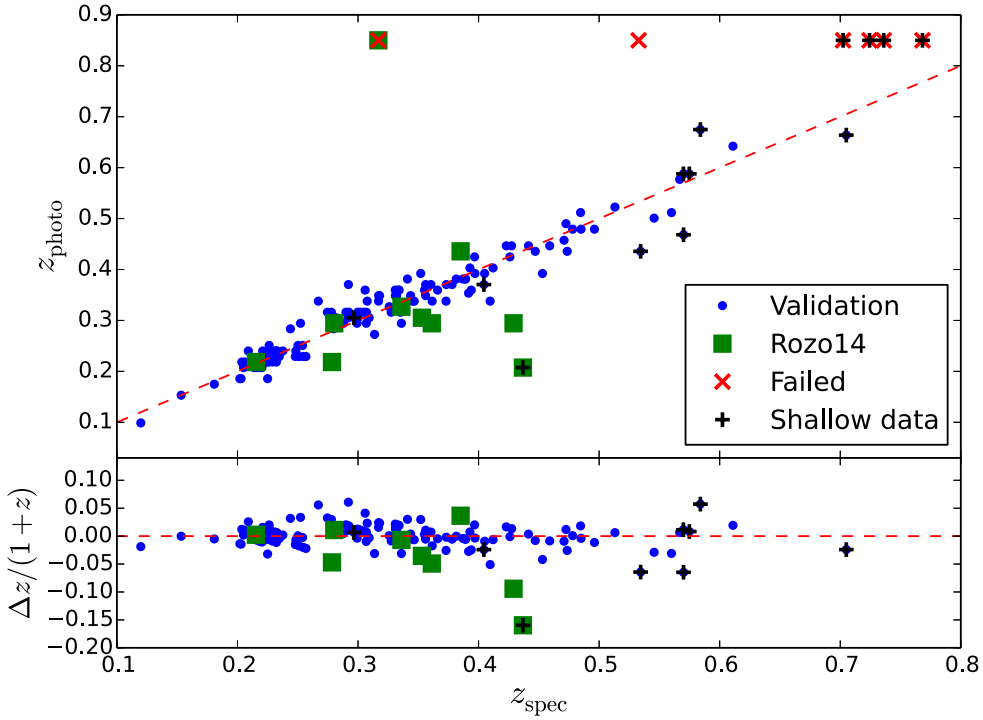

Figure 1.2 The photometric measurements for Planck confirmed clusters plotted against the spectroscopic redshifts (blue points). The red crosses mark the failures in our photometric redshift estimation. The black crosses present the clusters whose redshifts are higher then the redshift limits, and the green squares show outliers examined in Rozo et al. (2014).

depth for the candidate. In addition we multiplied by the evolution of the red fraction $f_r(z)$, which is characteristically decreasing as a function of redshift. The number one comes from the fact that the Brightest Cluster Galaxy is not included in this scaling relation, but needs to be counted in the Halo Occupation Number (HON). All these assumptions will be discussed and justified in more detail in Chapter 3.
Having the model, we directly measured the number of red galaxies from the candidate catalog. Inside R_{500}, the projected radius corresponding to a $10^{15} M_{\odot}$ candidate cluster, we summed up all galaxies with a likelihood of $> 5\%$ to be part of the RS. This likelihood is the same as described above in the photometric redshift estimation. The same was done inside a local background region. The method is illustrated in Figure 1.3. The expected Number of red galaxies from the model is shown with the black line. The measured number of RS galaxies is shown in red, the background number in blue, and the difference between both in green. The upper redshift limit for detection in Pan-STARRS fulfills the requirement that the predicted cluster galaxy population is detectable above the local background at a minimum of 2σ. With these limits, future follow-up surveys have a guidance for the required depths

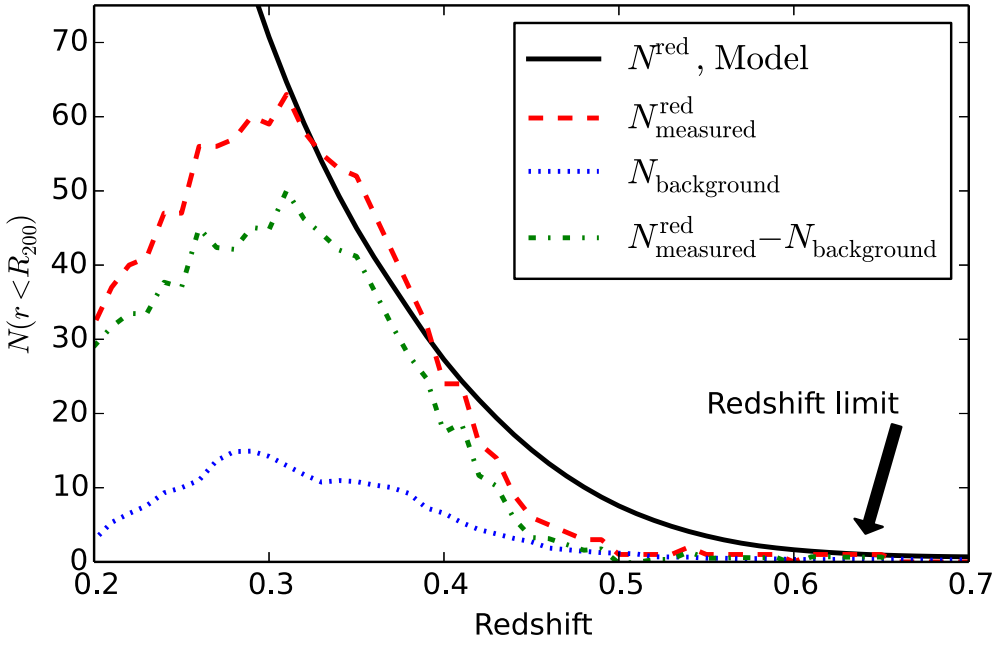

Figure 1.3 The observed number of red galaxies in the Planck confirmed cluster 442 at $z = 0.34$. The red dashed line is the red sequence galaxy number within R_{200}; the blue dotted line is the background number corrected to the R_{200} area of the cluster; and the green dash-dot line is the difference between those two. The black line is the predicted number of red sequence galaxies, which increases towards lower redshift as more and more faint galaxies in the luminosity function slide above the imaging detection threshold. We use this function together with the background to estimate a redshift lower limit in cases where no optical counterpart is identified (Liu et al. 2015).

of their follow-up data. In summary, we validated our approach on 150 confirmed Planck clusters and we were able to optically confirm and measure photometric redshifts for 60 Planck candidates. These brand-new confirmed clusters span a redshift range $0.06 < z < 0.69$. This is consistent with the redshift distribution expected for the previously confirmed sample of Planck selected clusters.

Our newly confirmed Planck clusters have been already used to update the full-sky Planck catalogue of SZ sources detected from the 29 month full-mission data (Planck Collaboration et al. 2015). The catalogue is the largest SZ-selected sample of galaxy clusters, as it contains 1653 detections, of which 1203 are confirmed clusters with identified counterparts. These confirmations have been made in external-data sets. With this large number of clusters, the Planck catalogue is supposed to be the first SZ-selected cluster survey having above 1000 confirmed galaxy clusters. This is an ideal sample for cosmological analysis.

1.4 Galaxy clusters as cosmological probes

The potential of galaxy cluster surveys as a cosmological probe has recently been demonstrated through the analysis of large X-ray and optically selected cluster samples spanning a wide range in redshift (e.g. Vikhlinin et al. 2009; Mantz et al. 2010; Rozo et al. 2010). Being the largest virialized structures in the Universe, galaxy clusters are important objects for cosmological studies. The current accepted ΛCDM cosmological model predicts the formation and evolution of galaxy clusters via hierarchical structure formation processes. Thus studies of their evolution as well as their cluster properties can place constraints on structure growth and the cosmological parameters. The abundance of galaxy clusters can be deduced from the geometry of the Universe and from the power spectrum of the initial density fluctuations. In particular, galaxy clusters are used to test cosmology by measuring their mass function, namely the number density of clusters as a function of their mass and redshift. Then this distribution in mass and redshift of the cluster counts is compared with theoretical models for the halo abundance, which are calibrated against N-body simulations of collision-less matter. An early result here is shown in Figure 1.4 with observational and simulation results from Bahcall & Cen (1992). They already found that a cosmological model with a mean matter density $\Omega_m = 0.25 - 0.35$ seems to match the data best. Instead a cosmology with $\Omega_m = 1$ can be ruled out by the observations. More precisely, the number density of clusters depends

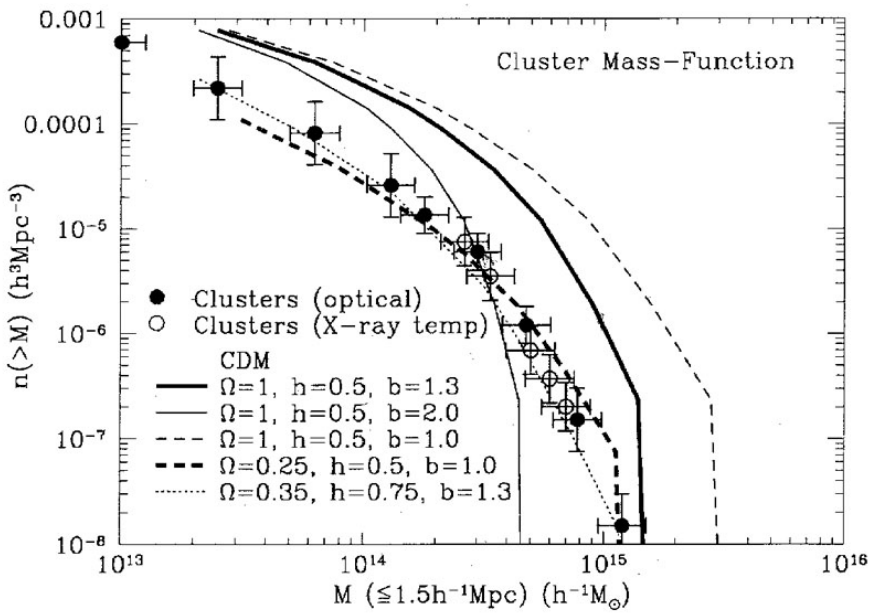

Figure 1.4 Cluster mass functions from observations and from CDM simulations. A cosmological model with a matter density $\Omega_m = 0.25 - 0.35$ seems to match the data best. Instead a cosmology with $\Omega_m = 1$ can be ruled out by the observations. Image credit: Bahcall & Cen (1992).

on the combination of Ω_m and σ_8, which is the normalization factor of the power spectrum.

σ_8 and Ω_m are degenerate with each other. Yet this degeneracy can be broken by considering the redshift evolution of the number density of clusters. Thus the redshift evolution of cluster counts can constrain the growth of structures and provides an independent measurement of Ω_m. A constrain on σ_8 can in principle be used to determine whether the dark energy density evolves with redshift.

As galaxy clusters are bright and sparsely distributed in the Universe, they are also tracers of large-scale structure. Such an analysis would then require large coverage of area on the sky. This will be reached by future surveys under way such as DES, LSST or EUCLID. Using cluster surveys that also provide distant cluster samples is even more relevant now, where we already have good cosmological constraints from local cluster samples within the Sloan Digital Sky Survey. Yet one needs to mention that unresolved cluster physics might be a limitation to applications of these methods to cosmology, and in particular for dark energy studies. The main problem is the mass determination of the clusters. The abundance of clusters is exponentially dependent on mass. Thus even a small error in mass induces a large error in abundance. The potential of galaxy clusters as cosmological probes is the driving engine for future steps of large surveys, simulations, cluster mass measurements and modeling of cluster physics in general.

1.5 The Dark Energy Survey

The Dark Energy Survey is an optical survey with the goal to understand the accelerating expansion of the Universe (Diehl et al. 2014). In 2012, the Dark Energy Camera (DECam), a 3 square-degree, 570-Megapixel CCD camera was installed on the 4-meter Blanco telescope at the Cerro Tololo Inter-American Observatory (CTIO) in the Atacama desert in Chile. The Dark Energy Survey will cover $\sim 5000 deg^2$ on the southern sky within 5 years survey time. DES started its first observing season on August 31, 2013 and observed for 105 nights through mid-February 2014. The survey plan is to image around 300 million galaxies within 5 different optical filters g, r, i, z, Y. The filter transmission curves can be seen in Figure 1.5. A smaller fraction of the observing nights will be used for tiny patches ($\sim 30 deg^2$) on the Sky to gather deep data for extensive supernovae studies. The Survey started with a Science Verification phase, where $\sim 200 deg^2$ have been observed to the nominal depth of the survey. DES is capable of combining 4 different probes for solving the Mystery of Dark Energy within one single facility. The constraining power of just one single cosmological probe is supposedly too weak to constrain simultaneously all different cosmological parameters. However, when combining different probes, one can reduce the degeneracy between them and reduce uncertainties on the parameters. In Detail DES will probe SN, BAO, Galaxy Clusters and Weak Gravitational Lensing (WL) (Mohr et al. 2012). The strength about galaxy clusters has already been mentioned in Sec 1.4. The others will be summarized in the following:

1.5.1 Supernovae Type Ia

Historically since 1998, surveys of cosmologically distant SN have shown that the expansion of the Universe is accelerating (Riess et al. 1998; Perlmutter et al. 1999). This means that

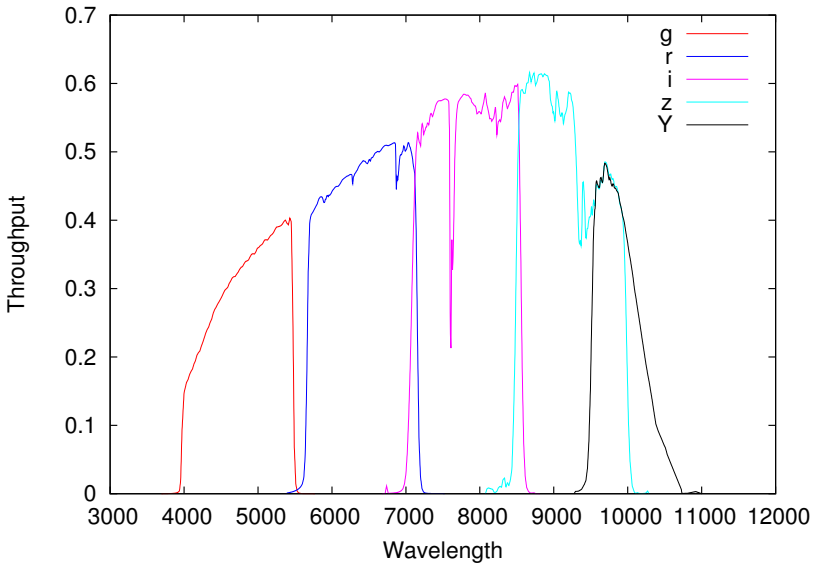

Figure 1.5 Filter transmission curves of DES including atmospheric corrections.

distant SN are measured to be fainter than expected in a decelerating Universe. An illustration can be seen in Fig 1.6. The underlying principle is the following: Since the Universe is expanding, it was smaller when the light from a very distant galaxy was emitted. If the expansion rate of the Universe is supposedly speeding up, then the size of the Universe increases faster with time than if the expansion was slowing down. If we know the distance to the galaxy and use the finite value of the speed of light from the theory of General Relativity, we know the age of the Universe when the galaxy emitted it's light. We then can compare the given distance to theoretical predictions and discriminate between different cosmological scenarios (e.g. acceleration or deceleration). In order to determine distances, astronomers use SN of Type Ia. These are the result of an exploding white dwarf that had accreted more matter than the Chandrasekhar mass limit. Among all known standard candles like Cepheids or Planetary Nebulae, SNIa are the most luminous ones. They have a characteristic luminosity which can be empirically standardized. Other Supernova Types have more complex physical processes during their collapse phase, which makes them less usable for standard candles. Due to the large brightness of SN, which is even more luminous than their host galaxy where they reside in, SN can be easily observed during their explosion phase, which can last a few days. By then comparing the brightness of two supernovae we can get the relative distance between them and thus measure the luminosity distance.
As a second step one needs to analyze the spectra of supernovae or their host galaxies in which they explode. Thus one can infer the redshift of the Supernova. To put it in a nutshell: Once we have the redshift of the SN we can use the relation between observed magnitude and the luminosity distance (which is a function of redshift and the underlying cosmology).
Under the assumption that the Universe is isotropic and homogeneous, this accelerated expansion implies either the existence of a fluid with negative pressure, which is referred to as

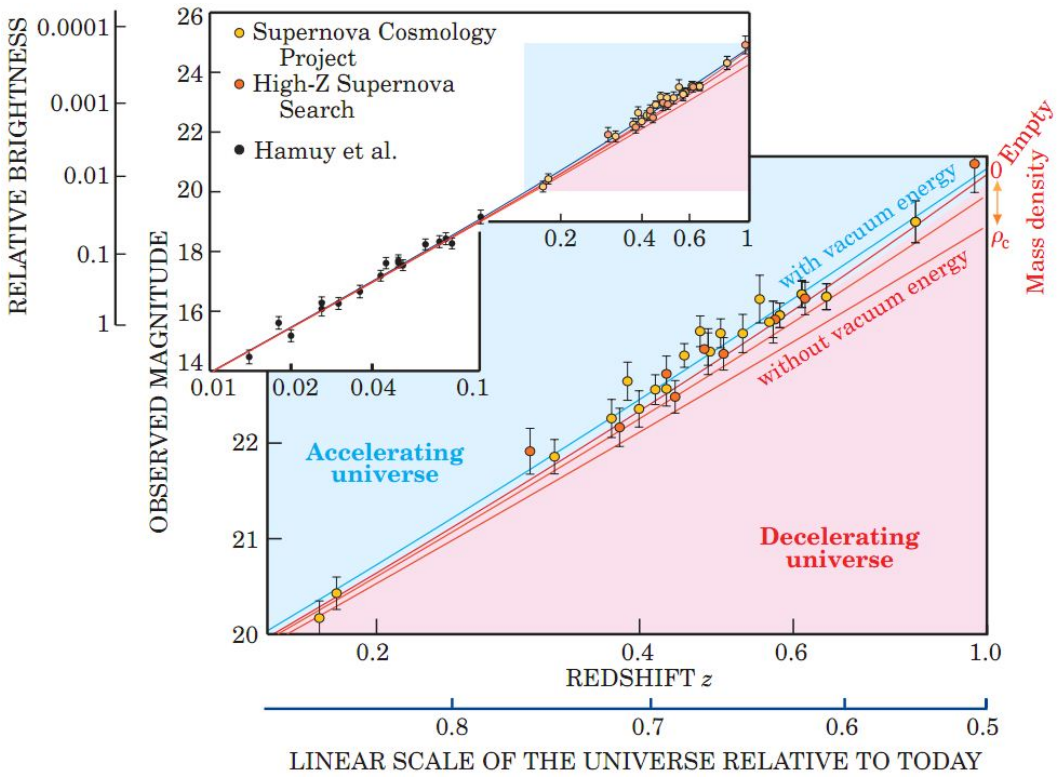

Figure 1.6 The plot shows the observed magnitude of distant Supernovae versus redshift (Perlmutter 2003), the so called Hubble-Diagram. Cosmological predictions for an accelerating and decelerating Universe are indicated with the solid lines. At redshifts beyond 0.1 the predictions start to diverge depending on the assumed vacuum energies. The red curves represent models with zero vacuum energy and mass densities from the critical density down to zero. The best fit (blue line) assumes a mass density of about 1/3 plus a vacuum energy density of about 2/3 of the of the critical density. This best fit implies an accelerating cosmic expansion.

dark energy, a cosmological constant, or modifications of gravity on cosmological scales (Guy et al. 2010).

1.5.2 BAO

After a period of inflation in the early Universe, there was a hot plasma of photons and baryons which were tightly coupled via Thomson scattering (Bassett & Hlozek 2010). At that time the photons were essentially trapped, as they could only travel short distances before interacting again with the baryonic matter. In this over dense plasma, radiation pressure was opposed by the gravitational collapse of matter. While an over dense region is gravitationally attracting matter towards it, the radiation pressure is directed outward of the dense region. These two competing forces generated oscillations, analogous to sound waves created

in air by pressure differences (ibid.). Such pressure waves are called Baryonic Acoustic Oscillations (BAO).
As the Universe is expanding the hot primordial plasma is cooling down. Electrons and protons inside the plasma can then combine to form neutral hydrogen. This happens at the period of Recombination at a redshift of $z \sim 1000$ (ibid.). Thus the pressure on the baryons is removed. Photons can propagate freely now, which means that the radiations is decoupled from the baryons. We identify these photons emitted after the period of Recombination with the *Cosmic Microwave Background* (CMB).
BAO have a characteristic scale known as the sound horizon, which represents the co-moving distance that a sound wave can travel between the big bang and recombination (Eisenstein et al. 2005). It has a dependency both on the expansion rate of the Universe as well as the sound speed of the primordial plasma. To be clear about the picture of the sound horizon: After recombination, photons are no longer interacting with baryonic matter so they radiate away. This process leaves a shell of baryonic matter at a fixed radius. This radius is often referred to as the sound horizon (ibid.).
BAO create a distinct oscillatory signature in the power spectrum of the large-scale structure of the universe (e.g. Holtzman 1989) , in the anisotropies of the cosmic microwave background (e.g. Hu & Dodelson 2002) and also in large galaxy redshift surveys (e.g. Eisenstein et al. 2005). The BAO signature has been measured by galaxy surveys as an over-density of galaxies at a characteristic co-moving scale of around $100h^{-1}Mpc$. In particular Eisenstein et al. (2005) used redshift-space correlation function of the Luminous Red Galaxies from the SDSS. His measurement can be seen in Fig 1.7, where different cosmological models are compared. The characteristic BAO bump is just reproduced by models which include baryons. With 3.4σ statistical detection, the BAO signature (as an imprint of the prediction of CDM cosmological theories) is significantly evident. The Eisenstein et al. (2005) detection confirmation comprises two aspects: first, that the oscillations occur at $z \sim 1000$, and second that they survive the intermediate time to be detected at low redshift. The small amplitude of the features requires that there exists matter at Recombination that does not interact with the photon-baryon fluid, which is DM.
The narrowness of the acoustic peak is an opportunity to measure distances out to higher redshifts. Eisenstein et al. (2005) noted that a given improvement in signal-to-noise ratio in the galaxy clustering statistic will make a significant improvement on the distance constraints. DES will be measuring the clustering of millions of galaxies at different redshifts. These measurements will determine the angular scale of the sound horizon. Combining those measurements together with SN measurements will then provide information on the history of the cosmic expansion rate of the Universe (Diehl et al. 2014).

1.5.3 Weak Lensing

This chapter presents the main thoughts from the review about gravitational lensing from Bartelmann & Schneider (2001), as well as the review about cosmic evolution from Voit (2005).
It is well known since Einstein's theory of General Relativity, that light rays which pass through an inhomogeneous gravitational field are deflected. The underlying assumption is

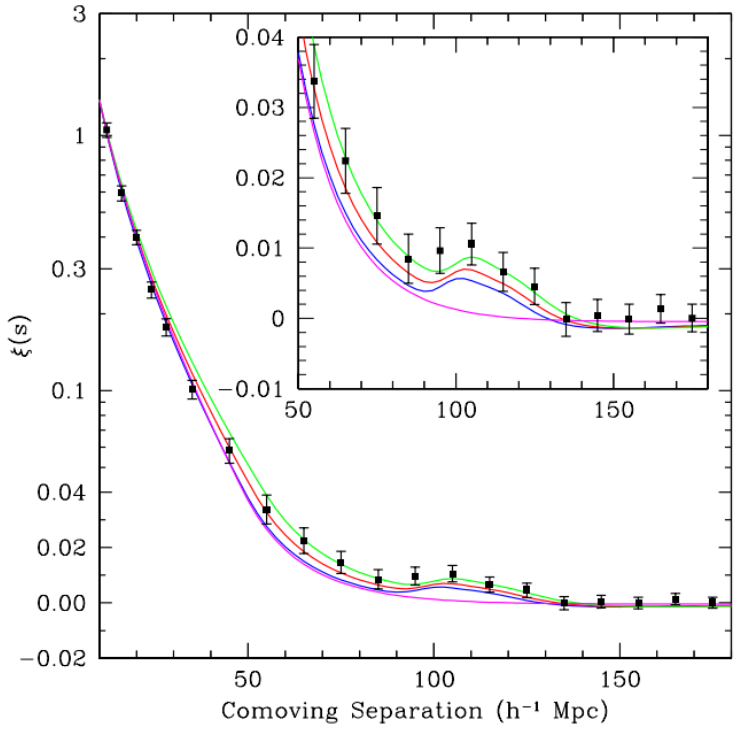

Figure 1.7 The large-scale redshift-space correlation function of the SDSS Luminous Red Galaxy sample. The models are $\Omega_m h^2 = 0.12$ (top, green), 0.13 (red), and 0.14 (bottom with peak, blue). The magenta line shows a pure CDM model ($\Omega_m h^2 = 0.105$), which does not include the acoustic peak. The bump at around $100h^{-1}Mpc$ is statistically significant. Image credit: Eisenstein et al. (2005)

that light rays behave like a stream of particles. Cosmic very massive structures can bend the light from a very distant galaxy that strong, so multiple light rays can reach a telescope. If we observe the image, then we see the galaxy source multiply imaged and with distorted shapes. An example is shown in Fig 1.8. The arc-like structures seen in Fig 1.8 are due to the so called *Strong gravitational lensing*. This effect can also produce multiple images (for point-like background sources) or even *Einstein rings* (for more extended background sources). The requirement for strong lensing to occur is that the projected lens mass density is greater than the critical density of the Universe. The cluster mass within a projected radius r_p will deflect all the photons toward our line of sight that pass through the cluster. Consequently the lensing effect is a function of the cluster mass. Already in 1937 Zwicky (1937) proposed in the study of the Coma cluster, that with the help of the gravitational lensing effect, the cluster mass should be possibly inferred. When the deflection angle is small compared to the background galaxy's distance to the cluster center, then we are in the regime of *Weak gravitational lensing*. Here we cannot see any multiple images or arcs, so we cannot discern any single background source. This is the more common effect in the Universe, compared to Strong lensing. Yet even in the weak lensing case, the presence of the

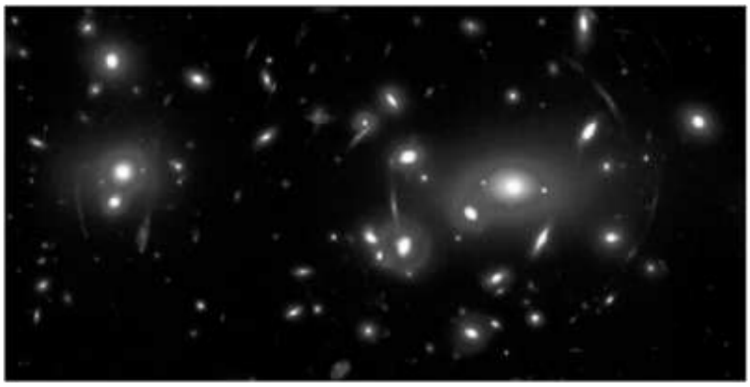

Figure 1.8 The image shows the galaxy cluster Abell 2218. It is an image of the central region of the cluster taken with the Hubble Space Telescope. We clearly see the bright elliptical cluster galaxies. Additionally there are distorted shapes of lensed galaxies behind the cluster, and we can see arc-like shapes that are due to the gravitational lensing effect. Image credit: Bartelmann & Schneider (2001)

foreground mass can be detected. Namely, the weak lensing effect is shifting each background source's image tangentially to a slightly larger distance from the cluster. Weak lensing thus acts like a coordinate transformation. The images of background sources are distorted and tangentially stretched. We can only observe the shear distortion, which presents the systematic alignment of all background galaxy sources around the cluster. It is not possible to reconstruct individual background galaxy shapes, as they are unknown.
Even in such low-signal effects, again we can detect the presence of a foreground mass, which is the galaxy cluster. Measuring the tangential shear distortion of the galaxies around a cluster and knowing their redshift distribution, it can be used to directly constrain the projected mass within an aperture (e.g. High et al. 2012). Weak lensing is a very promising method for measuring cluster masses, because it is independent of a cluster's baryon content, dynamical state, and mass-to-light ratio, which is needed in optical and X-ray mass measurements. DES will create a catalog of over 300 million galaxies looking for these alignments and slight galaxy distortions. The lensing effect will depend upon how clumped the distribution of dark matter is and upon the distances to the lensing structure. In this way, weak lensing will enable DES to simultaneously probe the growth of structure and the expansion of the universe over time.

Despite of solving the mystery of Dark Energy there is a variety of studies and projects than can be done with DES data.
Using the Science Verification Data Melchior et al. (2014) measured the weak-lensing masses and galaxy distributions of four massive galaxy clusters. Two of these clusters inhabited filamentary structures surrounding the clusters. This shows the potential of DES for detailed studies of degree-scale features on the sky and gathering insights on the environmental processes in the cluster outskirts and neighboring surrounding.
A recent study from Papadopoulos et al. (2015) found evidence for the first spectroscopically-

confirmed super-luminous supernova in the DES Year 1 data. They analyzed bolometric light curves and found that the model of a radioactive Ni^{56} decay, as well as a Magnetar-model fits the observed data well. In the future DES will find many more Supernovae of this type and their analysis will provide further insights of the underlying physical model.
The DES Collaboration et al. (2015) found evidence for eight new Milky Way companions in around $\sim 1800 deg^2$ DES first year data. Each of these new systems has been identified as a statistical significant over-density of stars on a consistent isochrone. They also show a luminosity function of an old and metal poor stellar population. If spectroscopically confirmed, these newly detected candidates may become the first ultra-faint dwarf galaxies identified outside the SDSS footprint, and would significantly increase the population of Local Group galaxies in the southern hemisphere.
Zhang et al. (in prep) uses a X-ray selected sample of 106 galaxy clusters out to redshift $z \sim 1.2$ to study the growth rate and evolution of BCGs. They find the BCG stellar mass growth rate to be slower than the common semi-analytical model simulations. As a reason they discuss a late formation of the ICL after a redshift of around 1.0.
On the optical studies of galaxy clusters DES has a unique overlap with the South Pole Telescope SZ survey providing a complete and homogeneously selected galaxy cluster sample with a well known selection function.

1.6 The South Pole Telescope

The South Pole Telescope is a 10 meter diameter telescope operating at the NSF South Pole research station (Carlstrom et al. 2011). It is located at the Amundsen-Scott South Pole station in Antarctica. The SPT survey goal is to observe a large area on the sky at 3 different frequencies, that is 95, 150 and 220 GHz bands. Therefore the SPT receiver includes a 966-pixel, multi-color, millimeter-wave, bolometer camera (ibid.) with a 1 arcmin resolution. Given this small resolution the SPT is designed to detect galaxy clusters at all redshifts and to measure the small-scale angular power spectrum of the CMB.
Why is the telescope built at the South Pole? The South Pole is a high, dry site with exceptional atmospheric transparency and stability at millimeter and sub-millimeter wavelengths which corresponds to the above mentioned frequencies. In this extreme frequency range, ground-based astronomy is challenged hard: there are tough requirements on the transmission and the stability of the atmospheric conditions. If otherwise, the bolometric camera would be loaded with too much additional noise, so the overall measurement will be distorted. For these reasons ground-based millimeter astronomy needs high altitude sites and stable atmospheric conditions (ibid.).
The SPT has been operating at the South Pole since February 2007 and was completed by the end of 2011. The coverage on the sky has a footprint of $\sim 2500 deg^2$.

1.6.1 The SZ effect

The following two sections contain thoughts from the cluster review paper of Voit (2005), which gives a general overview of galaxy clusters and their properties. In addition the SZ effect is well described in the reviews of Birkinshaw (1999); Rephaeli (1995); Carlstrom et al.

(2002).
As mentioned in Sec 1.1.3 the hot gas in galaxy clusters can be observed in the X-rays. Yet it can also be observed through its influence on the CMB. The CMB represents a perfect black body (Mather et al. 1990). Yet a perfect black-body spectrum is not expected in all directions and frequencies on the sky. It had been known, that locations in the Universe with energy transfers and releases can also affect the black-body spectrum. In order to cause a spectral distortion of the black-body there must occur radiative processes. These have to happen late in the evolution of the Universe, to prevent radiation from regaining their black body properties. As radiation is only weakly coupled to the given baryonic matter, it would thermalize and recreate a perfect Planck spectrum.

Already in the 1960's, Weymann (1966) analyzed, how Compton scattering would influence

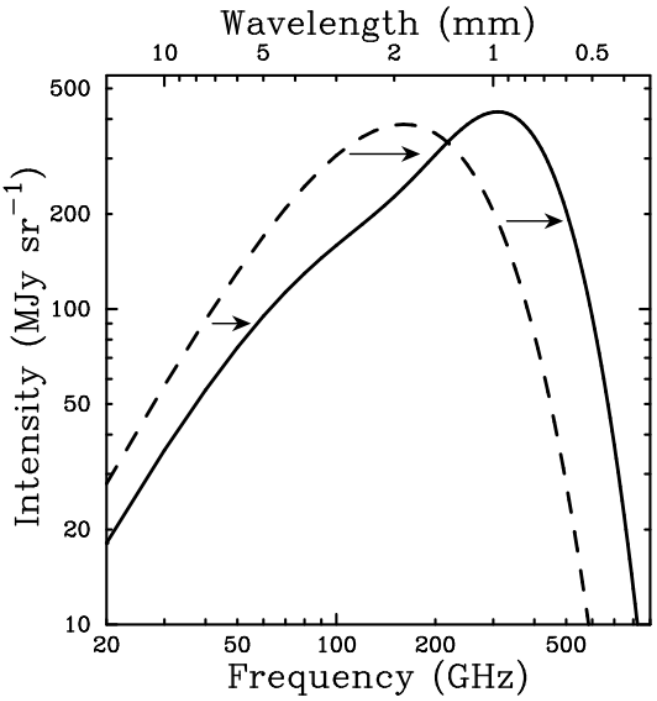

Figure 1.9 The figure shows the CMB spectrum as a perfect black body spectrum (solid line) and distorted by the SZE effect (dashed line). To illustrate the small effect, the SZE distortion shown here is for a fictional cluster 1000 times more massive than a typical massive galaxy cluster. The SZE causes a decrease in the CMB intensity at frequencies around 220 GHz and an increase at higher frequencies. Image credit: Carlstrom et al. (2002)

and distort the black body spectrum by shifting photons from the CMB to slightly higher energies. This effect happens when the photons from the CMB pass through the hot intergalactic gas. Since the 1970's it is known as the Sunyaev - Zeldovich - effect (Sunyaev & Zel'dovich 1972), who gave extensive calculations on it (see Fig 1.9). CMB photons passing through the center of a massive cluster have only a low chance of interacting with an energetic

ICM electron. Thus the SZ effect is rather a low-signal to Noise effect. Fig 1.9 shows the SZE spectral distortion for a fictional cluster that is over 1000 times more massive than a typical cluster to illustrate the small effect. The effect consists of a decrease in intensity of CMB photons at frequencies of around 220 GHz, and it has an intensity- increase at higher frequencies. We will just briefly summarize the basic formulae:
For a photon radiation field passing though an electron cloud in the hot ICM one can write the Comptonization parameter y as:

$$y = \int n_e \sigma_T dl \frac{k_B T_e}{m_e c^2} \tag{1.5}$$

where σ_T is the Thomson-cross section, n_e and m_e the electron-density and mass, k_B is the Boltzmann-Temperature, T the gas temperature and c the speed of light. The integral is over the line-of-sight of the cluster. The SZ effect can be divided into a thermal and a kinetic effect. The thermal SZ effect presents the spectral distortion of the CMB expressed as a temperature change ΔT_{SZE} at the dimensionless frequency $x = h/(k_B T_{CMB})$ and is given by

$$\frac{\Delta T_{SZE}}{T_{CMB}} = f(x)y = f(x) \int n_e \sigma_T dl \frac{k_B T_e}{m_e c^2} \tag{1.6}$$

The frequency dependence of the SZE is

$$f(x) = (x \frac{e^x + 1}{e^x - 1} - 4)(1 + \delta_{SZE}(x, T_e)) \tag{1.7}$$

where $\delta_{SZE}(x, T_e)$ is the relativistic correction to the frequency dependence.
The kinetic SZ effect produces additional distortion on the Planck spectrum due to the motion of the cluster with respect to the CMB.
The great benefit of the SZ effect for various cosmological studies is that the thermal SZ effect is independent of the distance of the cluster (i.e. the redshift) as seen in Equation 1.6. This implies that an SZ cluster survey is capable of detecting galaxy clusters out to an arbitrarily high redshift, in contrast to optical or X-ray surveys. Yet not all clusters (especially at high redshift) can be well resolved within the angular resolution. Thus SZ surveys measure an integrated Y parameter, which is defined as

$$Y = \int y dA \propto \int n_e T DV$$

The first integral is over the cluster's projected surface area dA and this is proportional to the second integral which is over the Volume. Thus the Y parameter describes the total thermal energy of the electrons, from which one can calculate the total gas mass times its mass-weighted temperature within a given region of space. If these regions can be chosen such that the gas mass is always proportional to the cluster's total mass, then the observable Y can be used a proxy of cluster mass. Yet this needs a careful calibration of the relation between Y and mass.

1.6.2 Observation and cluster detection within SPT

After the paper from Sunyaev & Zel'dovich (1972) there passed nearly 20 years until the first detections of the SZ effect were made (Birkinshaw 1991). Yet in the following years many clusters were detected with mm-arrays (e.g. Carlstrom et al. 2000). SZE observations have transformed from low S/N detections with limitations towards high confidence detections and detailed images with high quality. In order to extract complete cluster catalogs from the SZ survey, a matched filter approach is used. This method is described in Melin et al. (2006) and will be summarized here briefly.
The form of the spectral distortion due to the SZ effect is universal in the non-relativistic limit and the amplitude is given by the Compton -y parameter. In the SZ survey, galaxy clusters will have the appearance of extended sources with arcmin scales. They have a brightness profile that can be set into relation to the CMB brightness profile. The data from SPT are sky maps or set of maps at three different frequencies. A matched filter approach both needs spatial and spectral characteristics. The spectral characteristic is already given by the distorted black body spectrum. For the spatial characteristic, a beta-profile is used. Assuming this profile is the average valid one for all clusters, it just depends on one free parameter, that is the core radius. This spatial profile is then truncated at a reasonable radius. It is worthwhile to mention, that in reality the true underlying profile is not well known, and assumptions have to be made here.
In a first step, the observed frequency maps are convolved with matched filters that cover the expected range of core radii. Here different cluster sizes are used. In a second step cluster candidates are identified with a Signal-to-Noise ratio above a given threshold. In the brightest pixel of the maps, the cluster candidate is assigned a center. These steps are looped over where candidates are removed from the filtered maps. Consequently, clusters are added to the final cluster catalog while being subtracted from the maps one at a time, thereby de-blending the sources. Melin et al. (2006) note here, that the entire procedure relies heavily on the use of templates and that real clusters need not necessarily be described by them. Having a S/N ratio above 5, SPT will have a low contamination rate of false candidates with less than 2%. Yet this rate is still higher than expected from pure Gaussian fluctuations. This can be due to cluster-projection effects or residuals from cluster subtraction within the loops and cluster morphology. Furthermore point sources can contribute significantly to the contamination in galaxy clusters. The emission from point sources that lie within the line-of-sight of a cluster will fill in the SZE decrement and will lead to an underestimate. The radio point sources are variable and therefore must be monitored.
Yet the SPT SZ survey produces highly complete cluster catalogs even out to high redshifts. Any evolutionary studies will benefit from that.

1.6.3 Optical follow-up

As mentioned above, a sample selected by the SZE consists of clusters independent of redshift down to a limiting mass. Such a sample is the excellent prerequisite for cosmological analyses. Yet, as the SZ detection is independent of the cluster redshift, external cluster redshift measurements are required. This is primarily achieved with photometric redshifts

using optical and near infra-red broad band imaging observations. Ultimately all clusters are spectroscopically followed up to reduce the noise in the photometric redshift measurements. The completion of the SPT survey has significantly increased the number of clusters discovered with up to 80% new systems (Song et al. 2012a). Also there is an interesting high-mass sample at high redshift available.
The first big catalog paper, presented by SPT, is the one from Song et al. (2012b). They presented a sample of 224 cluster candidates that have been detected in the first $720 deg^2$ of the SPT survey which had been finished within the years 2008 and 2009. The optical follow-up was done using ground- and space-based optical and NIR telescopes (such as Spitzer, Magellan, Swope or Blanco). These were pointed observations of the SPT cluster candidates. 158 out of 224 SPT cluster candidates could be confirmed and photometric redshifts were measured with the multi band optical and NIR data. From these clusters lying at a median redraft of $z = 0.57$ (ibid.), the highest redshifted one was at $z = 1.35$. The photometric redshift measurement was based on the RS-galaxy over density in color-magnitude space. This method had been calibrated on a sub-sample of clusters with available spectroscopic redshifts.
For candidates without photometric redshift measurements, they calculated lower redshift limits. These limits were set by the available imaging depth. For some candidates, deeper data would be needed to confirm the cluster. Moreover catalog purity measurements are given: For a high S/N threshold of 6, the cluster catalog is fully complete. For lower thresholds like 5, the completeness drops to 95% and down to 70% for a S/N of 4.5 (Song et al. 2012b). As a typical cluster property BCG positions were determined. If there was no obvious visible BCG from the follow-up cluster image, then candidates were determined. They find that the distribution of SPT BCG center versus SZ center is similar to those found in X-ray surveys. This suggests that also the merger rates of SZ selected clusters are similar compared to the X-ray selected clusters.
The final catalog release is from Bleem et al. (2015) covering the full 2500 deg^2 of the SPT survey. This work presents the complete sample of clusters detected at high significance within the full SPT footprint that had been completed in 2011. 677 cluster candidates in total are detected above a S/N threshold of 4.5. 516 of these systems have been identified as real clusters with optical counterparts. The follow-up strategy has been changed since Song et al. (2012b). All cluster candidates have been now pre-screened using imaging data from the Digitized Sky Survey (DSS). Thus it was determined if a candidate is at low or high redshift. The low redshift clusters are observed at telescopes with 1-2m facilities, whereas higher redshifted targets have been observed with 4m-6.5m facilities. As in previous SPT publications, cluster candidates were to be confirmed if an excess of RS galaxies could be found at the SPT SZ location. Also photometric redshifts were estimated. In contrast to Song et al. (2012b), masses are given now for each confirmed cluster inside the full catalog. To estimate masses, the SZE mass-observable relation for a fixed flat ΛCDM cosmology was used. The purity of the final full SPT catalog is measured to be 75% for a S/N threshold of 4.5. To put it in a nutshell this combination of a clean and well-defined selection, large redshift extent, and high typical cluster mass enable a variety of cosmological and cluster physics analyses.

Thesis organization

This thesis is based on work done as part of the South Pole Telescope collaboration and the Dark Energy Survey collaboration. In Chapter 2 we present results on a sample of galaxy clusters selected from SPT using DES data from the Science Verification phase (SV). We briefly describe the sample properties, the data reduction and then analyze the radial profiles and color distributions of individual and stacked clusters. In particular we analyze the evolution of the red galaxy fraction compared to the total galaxy population. In Chapter 3 we extend the study of the SV sample looking at the Halo Occupation distribution and Luminosity Functions of these clusters. Finally in Chapter 4 we summarize our results and give an outlook for subsequent possible work in the future.

Chapter 2

Radial profiles and color distributions

This chapter is a paper draft that is under internal review within DES/SPT.

2.1 Introduction

Galaxy clusters were first systematically cataloged based on optical observations (Abell 1958; Zwicky et al. 1961). These clusters were primarily nearby systems, and they were mainly characterized by their richness, compactness and distance. Today, other techniques are widely used for detecting galaxy clusters. One of the most widely used is based upon an observational signature that arises through the interaction of the hot intra-cluster medium with the low energy cosmic-microwave-background (CMB) photons. This so-called thermal Sunyaev Zel'dovich effect (SZE) is a spectral distortion of the CMB due to inverse-Compton scattering of energetic galaxy cluster electrons from the CMB photons (Sunyaev & Zel'dovich 1972). The surface brightness of the SZE is independent of redshift and the integrated thermal SZE signature is expected to be a low-scatter mass proxy (e.g. Holder et al. 2001; Marrone et al. 2012; Planck Collaboration et al. 2011).

Using the SZE for cluster selection allows us to identify high completeness, approximately mass-limited cluster samples that span the full redshift range over which galaxy clusters exist (Song et al. 2012b; Reichardt et al. 2013; Bleem et al. 2014). Together with multi-band optical data, these cluster samples enable studies of galaxy cluster properties, including the luminosity function of the cluster galaxies, the stellar mass fraction, the radial profile and the distribution in the color space (e.g. Zenteno et al. 2011; Hilton et al. 2013; Chiu et al. 2014). These measurements allow us to gain insights into galaxy formation and evolution and to assess the degree to which these processes are affected by environment and vary over cosmic time (e.g. Butcher & Oemler 1984; Stanford et al. 1998; Lin et al. 2006; van der Burg et al. 2014a).

A picture of the galaxy populations inside and outside clusters has emerged where the mass functions (MFs) for the passive and star forming galaxies are independent of environment, but the mix of these populations changes as one moves from the field to the cluster (e.g. Muzzin et al. 2012; see also Binggeli et al. 1988; Jerjen & Tammann 1997; Andreon 1998). The redshift variation of the red fraction has been shown to provide constraints on the timescales on which infalling field galaxies are transformed to red sequence (RS) galaxies (McGee et al. 2009). Moreover, the scatter of the RS and its variation with redshift has been used to

constrain the variation in star formation histories and the timescale since the formation of the bulk of stars within RS galaxies (e.g. Mei et al. 2009; Hilton et al. 2009; Papovich et al. 2010).

The use of a homogeneously selected cluster sample extending over a broad redshift range and with relatively uniform depth, multi-band imaging then enables one to carry out a systematic study of the population variations as a function of redshift and cluster mass. This avoids the difficultly of accounting for differences in virial mass estimates, initial mass functions (IMFs) and analysis techniques when combining results from high redshift samples to previously published low redshift results. Moreover, with selection that does not directly depend on the galaxy population being studied, the interpretation of redshift trends is more straightforward.

In this paper, we report on our analysis of the color distribution and the radial profile of the full and the color selected RS component of the cluster galaxy population. Our primary goal in the following analysis is to understand how the cluster galaxy populations change with redshift and cluster mass. We are driven by our desire to better understand the formation of massive cluster galaxy populations through accretion of subclusters and direct infall from the field. In addition, we are interested in exploring the timescale for the transition of infalling field galaxies into RS galaxies, and also in examining whether the growth of the central galaxies over time leaves an imprint on the general cluster galaxy population. Rather than carrying out our analysis using stellar mass estimates extracted with SED fitting, we focus on magnitudes and colors that are extracted from the same portion of the rest frame spectrum over the full redshift range.

Our sample arises from the overlap between the Dark Energy Survey science verification (DES-SV) data and the existing South Pole Telescope (SPT) 2500 deg^2 mm-wave survey (SPT-SZ; e.g. Story et al. 2013). The sample of SPT-SZ cluster candidates overlapping the DES-SV data contains 74 clusters. Our analysis follows the optical study of the first four SZE selected clusters in Zenteno et al. (2011), and is complementary to an analysis of the 26 most massive clusters extracted from the full SPT survey (Zenteno et al, in preparation). We include not only a comparison to previous results from X-ray selected clusters but also to results from optical and NIR selected clusters.

This paper is organized as follows: Section 2.2 describes the DES-SV observations and data reduction as well as the SPT selected cluster sample. In Section 2.3 we describe the cluster sample properties, presenting the redshifts and masses. In Section 2.4 we present measurements of the radial and color distributions. We end with discussion and conclusions in Section 2.5.

In this work, unless otherwise specified, we assume a flat ΛCDM Cosmology. The cluster masses refer to $M_{200,c}$, the mass enclosed within a sphere of radius R_{200}, in which the mean matter density is equal to 200 times the critical density at the observed cluster redshift. The critical density is $\rho_{crit}(z) = 3H^2(z)/8\pi G$, where $H(z)$ is the Hubble parameter. We use the best fit cosmological parameters from Bocquet et al. (2014): $\Omega_m = 0.292$ and $H_0 = 68.6$ km $\mathrm{s}^{-1}\mathrm{Mpc}^{-1}$; these are derived through a combined analysis of the SPT cluster population, the WMAP constraints on the cosmic microwave background (CMB) anisotropy, supernovae distance measurements and baryon acoustic oscillation distance measurements.

2.2 Observations and Data reduction

There are 74 clusters detected by SPT that are imaged within the DES-SV data and have deep photometric coverage within at least $1deg^2$ around the cluster position. Below we describe how the sample of 74 multi-band coadds and associated calibrated galaxy catalogs are produced.

2.2.1 DECam Data Processing and Calibration

The DES-SV observations were acquired between November 1, 2012 to February 22, 2013. The data were processed with an improved version of the pipeline used to process the Blanco Cosmology Survey Data (Desai et al. 2012), which has its heritage in the early DES data management system (Ngeow et al. 2006; Mohr et al. 2008, 2012). Following a data flow similar to that adopted for the BCS processing, we process data from every night using the single epoch pipeline. The raw data from the telescope are first crosstalk corrected. For DECam, the crosstalk matrix includes negative co-efficients and also non-linear corrections for certain CCDs/amplifiers. Single-epoch images are then produced through a bias subtraction and dome flat correction. We implement a pixel scale correction to reduce the positional variation in the zeropoint or, equivalently, to flatten the zeropoint surface within the individual detectors. No illumination or fringe corrections are applied; we adopt a star flat procedure to photometrically flatten the images. In particular, we stack first season photometric stellar photometry in detector coordinates and determine for each band the persistent photometric residual in stellar photometry as a function of position. We use this to create a position dependent photometric scale factor that further flattens the zeropoint surface within each detector and also brings all detectors to a common zeropoint (see also Regnault et al. 2009; Schlafly et al. 2012).

First pass astrometric calibration is carried out exposure by exposure using the `SCAMP` Astromatic software (Bertin 2006) and by calibrating to the 2MASS catalog (Skrutskie et al. 2006). In this approach we use as input a high quality distortion map for the detector that we determine through a `SCAMP` run of a large collection of overlapping exposures. The residual scatter of our first pass astrometry around 2MASS is approximately 200 milli-arcseconds, which is dominated by the 2MASS positional uncertainties. In a second pass prior to the coaddition, we recalibrate the astrometry using `SCAMP` and the full collection of overlapping DECam images around a particular area of interest on the sky (i.e. where there is a known SPT cluster). This reduces the relative root mean square internal astrometric scatter around the best fit to 20 milli-arcseconds, which is a factor of a few improvement over the internal scatter in the first pass calibration. For the data used in these analyses we find the first pass astrometric solution to be adequate to our needs.

Scientific cataloging is carried out using the model-fitting engine of SExtractor (Bertin & Arnouts 1996), where we create position dependent point spread function (PSF) models for each image using PSFEx and then use use these PSF models to create a variety of customized, PSF corrected model magnitudes, object positions, morphology measures and star-galaxy classification.

Once all the data from each night are processed using the single epoch pipeline, we then

photometrically calibrate the data and build coadds centered around each of the SPT cluster candidates. We determine a relative photometric calibration using common stars within overlapping images. We create median-combined coadd images using PSF homogenization to a common Moffat profile (Moffat 1969) with a full width at half maximum (FWHM) tuned to be the median of all the input single epoch images for each band. For coadd cataloging we first create a chi-square detection image using the i and z band coadd images, and then we catalog in dual image mode, using a common detection image across all bands. We use only the catalogs extracted from the PSF homogenized coadd images, because we have identified failure modes in the star-galaxy classification in the non-homogenized coadds that are caused by discontinuities in the spatial variation of the PSF.

For absolute photometric calibration of the final catalog we calibrate the color differences among different band combinations using the DECam stellar locus, where we first calibrate $(g-r)$ vs $(r-i)$ and then keeping the $(r-i)$ offset fixed, we calibrate $(r-i)$ vs $(i-z)$. The absolute calibration comes from the 2MASS J band. We find that the stellar locus scatter in $gr-ri$ and $ri-iz$ is about 32 mmag and 17 mmag, respectively, which compares quite well to the scatter in the Pan-STARRS1 survey (29 mmag and 17 mmag, respectively; Liu et al. 2015) and is significantly better than the scatter in the Sloan-Digital-Sky Survey (40 mmag and 50 mmag, respectively; Desai et al. 2012). The final catalogs, which we create are thus calibrated to the DECam system. We do not use any data from the Y band for this analysis, although we do create Y-band coadd images for all the SPT cluster candidates.

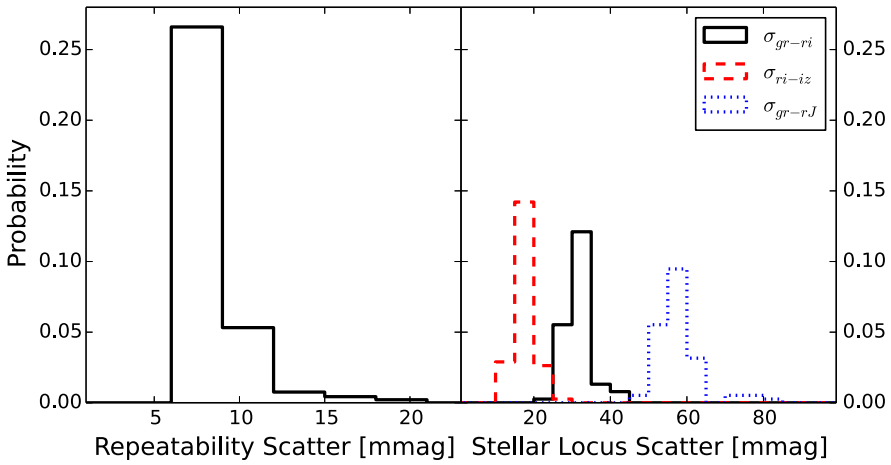

Figure 2.1 Distribution of single epoch photometric repeatability scatter (left) for multiple measurements of the same stars in our ensemble of 74 clusters. The bands *griz* have a median scatter of 7.6, 7.6, 7.7 and 8.3 mmag, respectively. The distribution of orthogonal scatter about the stellar locus is shown on the right for three color-color spaces. The scatter distributions for these three spaces have a median scatter of 17, 32 and 57 mmag.

To determine the stellar locus in the DECam system we bootstrap from calibrated SDSS photometry. We do this by determining the color terms between the DECam and SDSS

systems using DECam observations of calibrated stars within the SDSS system. The first order color terms we find are -0.088,-0.1079,-0.3080 and -0.0980 for g,r,i,z bands, respectively, where we use the color $g - r$ for g and r band and $r - i$ for i and z. With these color terms we then use calibrated SDSS photometry to predict the DECam stellar locus. In this step we restrict our analysis to those stars with colors that lie in the range where the linear color correction is accurate at the <1% level. We then use this predicted stellar locus to calibrate the offsets in an empirical DECam stellar locus that we extract from selected high quality observations of a portion of the survey.

For each calibrated tile we evaluate the quality of the images and catalogs using the scatter around the stellar locus and the scatter obtained from photometric repeatability tests. Figure 2.1 (right) contains a plot of the orthogonal scatter of stars about the stellar locus in three different color-color spaces r-i vs. i-z, g-r vs. r-i and g-r vs. r-J. The median scatter about the stellar locus in these three spaces is 17, 32 and 57 mmag, respectively. These values are comparable to the stellar locus scatter in a recent PS1 analysis (Liu et al. 2015) and better than values obtained from the BCS or SDSS datasets (Desai et al. 2012).

In the photometric repeatability tests we compare the magnitude differences between multiple observations of the same object that are obtained from different single-epoch images which contribute to the coadd tile. Figure 2.1 (left) contains a plot of the distribution of repeatability scatter for our 74 clusters. We find that the median single-epoch photometry has bright end repeatability scatter of 7.6, 7.6, 7.7 and 8.3 mmag in bands $griz$, respectively. This compares favourably with the PS1 repeatability scatter of 16 to 19 mmag (Liu et al. 2015) and is better than the characteristic BCS scatter of 18 to 25 mmag (Desai et al. 2012). Coadd tiles with repeatability scatter larger than 20 mmag were re-examined and recalibrated to improve the photometry.

Given the large offset strategy of the data acquisition for DES, each point on the sky is imaged from multiple independent portions of the focal plane. Thus, we expect the systematic floor in the coadd photometry to scale approximately as this single epoch systematic floor divided by the square root of the number of layers contributing to the coadd. Given that the bulk of the SV data used for this analysis have full DES depth, corresponding to 10 layers of imaging, we expect in principle to achieve a systematic error floor in the relative coadd photometry between 2 and 3 mmag.

2.2.2 Star-Galaxy Separation

Our photometric catalogs are produced using model fitting photometry on homogenized coadded images, and they therefore contain two different star-galaxy separators: class_star and spread_model. To examine the reliability of the separation we look at the values of those two classifiers as a function of magnitude (Desai et al. 2012). Class_star contains values between 0 and 1 representing a continuum between galaxy-like and star-like. At magnitudes of ~ 20 in the DES data the galaxy and stellar populations begin to merge, making classification with class_star quite noisy. Spread_model values exhibit a strong stellar sequence at spread_model ~ 0, whereas galaxies have more positive values. In the case of spread_model the two sequences start merging at roughly ~ 22 magnitude in each band, indicating that spread_model is effective at classifying objects that are approximately an order of magnitude fainter than

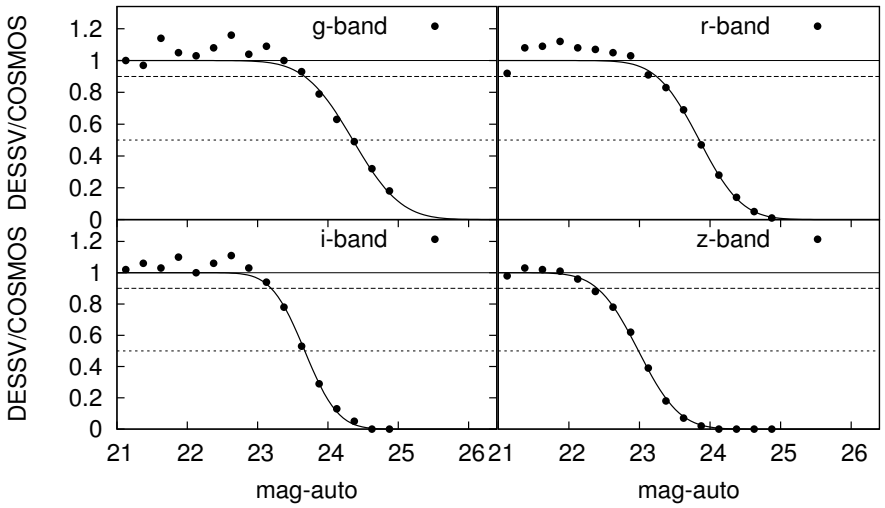

Figure 2.2 Completeness functions in each band for SPT-CLJ0423-6143. We compare the object counts observed toward the cluster to the counts from deeper data from the COSMOS survey. The resulting completeness curve is fit by an error function, which we use to estimate 50% and 90% completeness.

those that are well classified by class_star. For this reason, we use a spread_model cut for the star/galaxy classification in the z-band, as it is used as a detection band. Examining the cluster catalogs, we find that a reliable cut to exclude stars is spread_model> 0.002.

Note that spread_model is derived using a fit to the local shape of the PSF. Thus, locations where the PSF varies discontinuously will produce significant PSF errors in the PSF modeling and the spread_model classification will be unreliable. As mentioned above we produce PSF homogenized coadd images to avoid this problem.

2.2.3 Completeness Estimates

Following Zenteno et al. (2011) we estimate the completeness of the DES-SV tiles by comparing their *griz* count histograms for all objects against those from the Cosmic Evolution Survey (COSMOS; see e.g. Taniguchi et al. 2005). COSMOS was launched to study the relationship between formation of galaxies and large scale structure in the universe. COSMOS surveyed a 2 deg^2 equatorial field ($RA = 150.1167, DEC = 2.2058$) with the Advanced Camera for Surveys from Hubble Space Telescope (HST). These data have been supplemented by additional ground based images from the Subaru telescope, and these are the data we use here.

We extract a COSMOS source count histogram from the public photometric catalog including SDSS *griz* bands that are transformed to our DES catalog magnitudes and normalized to the appropriate survey area. The typical shifts in magnitude going from SDSS to DES are small compared to the size of the bins we employ to measure the count histogram. The

COSMOS counts extend down to a $10\,\sigma$ magnitude limit of around g ∼25.1, r ∼24.9, i ∼25, z ∼24.1.

Because the analyzed DES cluster tiles do not overlap with the COSMOS footprint, we measure the magnitude limits at 50% and 90% completeness levels by calculating the ratios between the DES area-renormalized number counts and the COSMOS ones. First, we fit the DES number counts at intermediate magnitudes where both surveys are complete with a power law, whose slope is fixed to that obtained for COSMOS number counts within a similar magnitude range. Note here that we ensure that the fit is done over a magnitude range with above ∼95% completeness. The ratio between these two power laws is used for renormalizing the DES number counts, effectively accounting for field-to-field variance in the counts.

We then fit an error function to the ratio of the renormalized DES and COSMOS counts to estimate the 50% and 90% completeness depths (see Figure 2.2). For the most part, this approach of estimating completeness works well, but due to mismatch between the power law behaviour of the counts in the region where both surveys are complete and also due to noise in the counts, the completeness estimate for DES can in some cases scatter above 1. In particular, we have encountered some difficulties with greater stellar contamination in the DES regions that are closest to the Large Magellanic Cloud.

The analysis is performed using mag_auto and a magnitude error cut of 0.3. We use a magnitude error cut to exclude unreliable objects at the detection limit from our analysis, and we do the same thing in our analysis of the science frames. Cutting at even larger magnitude errors does not change the depths significantly. Furthermore we exclude the cluster area within a projected distance of R_{200} from this analysis, because this region is particularly contaminated by the presence of cluster galaxies. The mean 50% completeness magnitude limit for the DES photometry in all 74 confirmed clusters is 24.2, 23.9, 23.3, 22.8 for *griz*, respectively, and the RMS (root mean square) variation around the mean is 0.05, 0.05, 0.05, 0.04. The scale of the variation is a reminder that not all SPT cluster fields have been observed to full depth.

2.3 Galaxy Cluster Properties

In our analysis we focus on the galaxy population within the cluster virial regions of an SPT selected sample of massive clusters. To define a common region within which to study the galaxy population we require a redshift and a mass estimate for each system. In this section we describe our method for measuring the cluster redshifts and for estimating the cluster masses.

2.3.1 Redshifts

For our cluster candidates we use the red sequence (RS) galaxy population to estimate a photometric redshift. Our approach is similar to the one used in Song et al. (2012a,b) and has been successfully applied to Planck Cluster Candidates in Liu et al. (2015). The method is based on the RS over-density in color-magnitude space. We model the evolutionary change in color of cluster member galaxies over a large redshift range by using a composite stellar population (CSP) model.

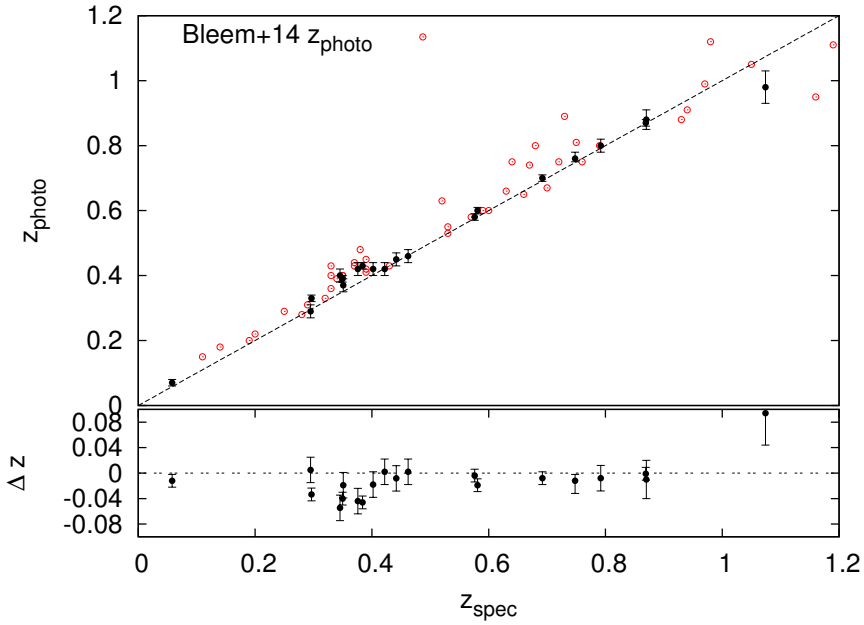

Figure 2.3 Photometric redshift z_{photo} versus spectroscopic redshift z_{spec} for the 20 clusters (top) where z_{spec} is available. The distribution of the photometric redshift residuals $\Delta z = z_{spec} - z_{photo}$ as a function of redshift z_{spec} is shown in the bottom panel. The characteristic error is $\Delta z/(1+z) = 0.02$. We additionally show a comparison of photometric redshifts derived from DES data to the ones from the SPT follow up program in Bleem et al. (2015) with red circles.

Stellar population evolutionary model

A range of previous studies have shown that early type galaxies within clusters have stellar flux that is dominated by passively evolving stellar populations formed at redshifts $2 < z < 5$ (e.g., de Propris et al. 1999; Lin et al. 2006). We adopt a model consistent with these findings. Specifically, our star formation model is an exponentially decaying starburst at redshift $z = 3$ with a Chabrier IMF and a decay time of 0.4 Gyr (Bruzual & Charlot 2003, hereafter BC03). We introduce tilt in the red sequence by using 6 different models, each with a different metallicity (Kodama & Arimoto 1997) adjusted to follow the luminosity - metallicity relation observed in Coma (Poggianti et al. 2001). Derived from the best fit metallicity-luminosity relation in Poggianti et al. (2001) for Z(Hg) the corresponding metallicities used are 0.0191 ($3L^*$), 0.0138 ($2L^*$), 0.0107 (L^*), 0.0084 ($0.5L^*$), 0.0070 ($0.4L^*$), 0.0047 ($0.3L^*$).

We use DES filter transmission curves derived from the DECal system response curves that account for telescope, filters and CCDs and that include atmospheric transmission. We use these filter transmission curves together with the *EzGal* Python interface (Mancone et al. 2012) to calibrate our BC03 CSPs and to create model galaxy magnitudes in the griz bands and within a luminosity range of $0.3L^* < L^* < 3L^*$.

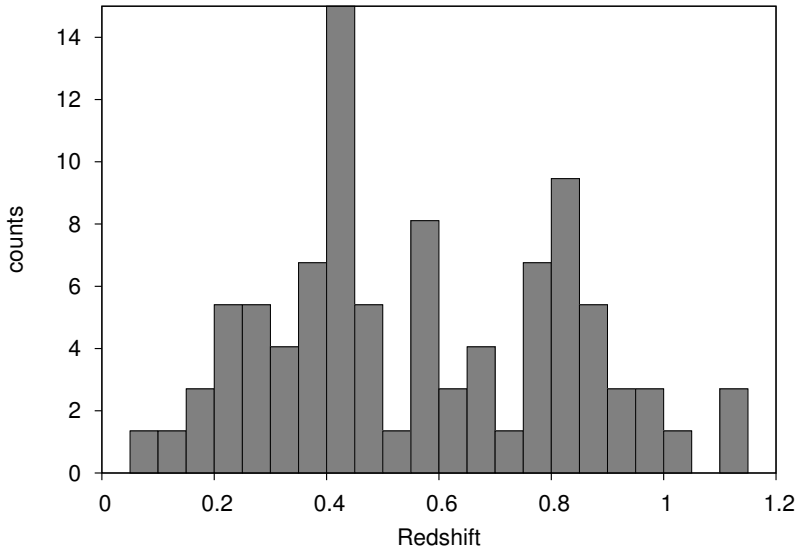

Figure 2.4 Redshift histogram of all cluster candidates in our sample. We use spectroscopic redshifts z_{spec} when available. The median redshift of our sample is $z = 0.46$.

Redshift Measurements

A cluster is confirmed by identifying an excess of galaxies at a particular location in color space within the color-magnitude space defined by magnitudes in different pairs of filters. We scan through redshift and obtain half the virial radius R_{200} at each redshift from the SZE mass proxy as (see discussion in Section 2.3.2). Following previous work on X-ray and SZE selected clusters (Song et al. 2012a,b), we define a search aperture for each cluster that is centered on the SPT candidate position and has a radius of $0.5 * R_{200}$. To measure the number of galaxies above background at each redshift, we adopt a magnitude cut of $0.4L^*$ together with a magnitude uncertainty cut $\sigma_{mag} < 0.1$ to exclude faint galaxies. Each galaxy within the radial aperture is assigned two different weighting factors, one accounting for the spatial position in the cluster area and one for the galaxy position in color-magnitude space. The color weighting L_{col} accounts for the orthogonal distance d of each galaxy in color-magnitude space from the tilted RS appropriate for the redshift being tested and has the form of a Gaussian:

$$L_{col} = \exp\left(-\frac{d^2}{2\sigma_{col}^2}\right) \tag{2.1}$$

Here $\sigma_{col}^2 = \sigma_{int}^2 + \sigma_{proj}^2$, where we adopt $\sigma_{int} = 0.05$ as the intrinsic scatter in the RS (initially assumed to be fixed) and σ_{proj}^2 is the combined color and magnitude measurement uncertainty projected on the orthogonal distance to the RS. The spatial weighting $L_{pos} \sim \frac{1}{x^2-1} f(x)$ has the form of the projected NFW profile (Navarro et al. 1997) and the profile is described in detail in Section 2.4.2. The final weighting is the product of both factors.

In this way, all galaxies close to the cluster centre and with colors consistent with the red sequence at the redshift being tested are given a high weight, whereas galaxies in the cluster outskirts with colors inconsistent with the red sequence are given a small weight. We use a local background annulus within $\sim 1.5-3R_{200}$, depending on the extent of the tile, to define the background region for statistical background correction. The background measurement is obtained by applying for each galaxy the color weight and a mean NFW weight derived from the cluster galaxies and then correcting for the difference in area.

We observe the color magnitude relation using the photometric band that contains the rest frame 4000 Å break and another band redward of this. The appropriate colors for low redshift clusters $z < 0.35$ are $g-r$ and $g-i$, for intermediate redshift clusters $0.35 < z < 0.75$ are $r-i$ and $r-z$ and for clusters at redshifts $z > 0.75$ are $r-z$ and $i-z$. These colors provide the best opportunity to separate red from blue galaxies (i.e. passive from star forming galaxies). For each of these color combinations we construct histograms of the weighted number of galaxies as a function of redshift. The weighted number of galaxies is defined as the sum of all galaxy weights within the cluster search aperture that has been statistically background subtracted. The cluster photometric redshift is then estimated from the most significant peak in the histogram. The photometric redshift uncertainty is the $1\,\sigma$ positional uncertainty of the peak, which is derived from fitting a gaussian to the peak, and then dividing the full width at half maximum (FWHM) of the peak by the square-root of the weighted galaxy number at the peak.

To test our photometric redshifts we use a sample of 20 spectroscopic redshifts available in the literature (Song et al. 2012b; Ruel et al. 2012). The performance of the method can be seen in Figure 2.3. The RMS scatter of $\Delta z/(1+z)$ using our small spectroscopic cluster sample is 0.02. Thus, the cluster photometric redshift performance is consistent with our expectation from studies of other SPT selected cluster samples (Song et al. 2012b) .

The redshift distribution for all confirmed clusters is shown in Figure 2.4, and the individual photometric redshifts are listed in Table 2.3 and Table 2.4. The mean redshift of our cluster sample is 0.56, the median is 0.46, and the sample lies between 0.07 and 1.11. For redshifts $z > 1$ it is better to use the optical data in combination with NIR data to estimate reliable photometric redshifts; nevertheless, with the few clusters we have in this redshift range our DES photometric redshifts perform reasonably well. We refer the reader to the appendix for more details about individual problematic cases.

2.3.2 Cluster Masses

The SPT-SZ survey consists of mm-wave imaging of 2500 deg^2 of the southern sky in three frequencies (95, 150 and 220 GHz) (e.g., Story et al. 2013). Details of the survey and data processing are published elsewhere (Schaffer et al. 2011). Galaxy clusters are detected via their thermal SZE signature in the 95 and 150 GHz SPT maps using a multi-scale and multi-frequency matched-filter approach (Melin et al. 2006; Vanderlinde et al. 2010). This filtering produces a list of cluster candidates, each with positions and a detection significance ξ, which is chosen from the filter scale that maximizes the cluster significance. We use this selection observable also as our mass proxy.

Due to observational noise and the noise biases associated with searching for peaks as a

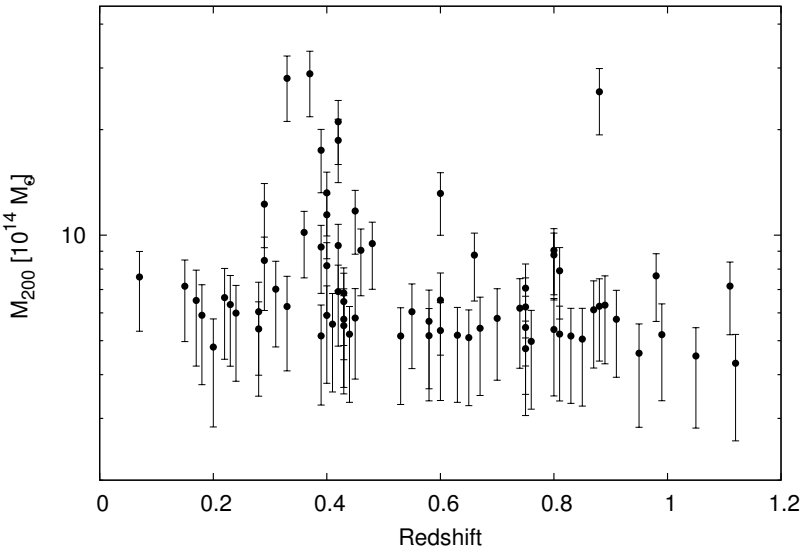

Figure 2.5 The cluster sample as a function of mass M_{200}. The error bars reflect the 1σ mass uncertainties. The median mass of the sample is $6 \times 10^{14} M_{\odot}$. We adopt these median values as pivot points in our joint mass and redshift power law fits to the observed galaxy population properties.

function of sky position and filter scale, we introduce a second unbiased SZE significance ζ which is related to the mass M_{500} in the following manner:

$$\zeta = A_{\rm SZ} \left(\frac{M_{500}}{3 \times 10^{14} M_{\odot} h^{-1}} \right)^{B_{\rm SZ}} \left(\frac{E(z)}{E(0.6)} \right)^{C_{\rm SZ}} \tag{2.2}$$

where $A_{\rm SZ}$ is the normalization, $B_{\rm SZ}$ is the slope and $C_{\rm SZ}$ is the redshift evolution parameter. An additional parameter $D_{\rm SZ}$ describes the intrinsic log-normal scatter in ζ at fixed mass, which is assumed to be constant as a function of mass and redshift. For $\xi > 2$, the relationship between the observed ξ and the unbiased ζ is

$$\zeta = \sqrt{\langle \xi \rangle^2 - 3}. \tag{2.3}$$

For our analysis we use the masses from the recent SPT mass calibration and cosmological analysis (Bocquet et al. 2014) that uses a 100 cluster sample together with 63 cluster velocity dispersions (Ruel et al. 2012) and 16 X-ray Y_X measurements (Andersson et al. 2011; Benson et al. 2013). The Bocquet et al. (2014) analysis combines this SPT cluster dataset with CMB anisotropy constraints from WMAP9 (Hinshaw et al. 2013) and distance measurements from supernovae (Suzuki et al. 2012) and baryon acoustic oscillations (Beutler et al. 2011; Padmanabhan et al. 2012; Anderson et al. 2012).

Briefly, the mass estimates (and associated uncertainties) for each cluster include bias corrections associated with selection (the so-called Eddington bias) and are marginalized over

cosmological and scaling relation parameter. The conversion from the M_{500} in Equation 2.2 to the M_{200} used here assumes an NFW model (Navarro et al. 1997) with a concentration c sampled from structure formation simulations Duffy et al. (2008). The mass–redshift distribution for the full cluster sample is shown in Figure 2.5, and the masses for all clusters are listed in Table 2.3 and Table 2.4.

All the details of the mass calibration can be found in Bocquet et al. (2014). For the purposes of this work we note that if we had adopted the *Planck* CMB anisotropy constraints instead of WMAP9 it would increase our masses by ∼6%. Also, our characteristic cluster mass uncertainty is ∼20%, corresponding to a virial radius uncertainty of ∼7%.

Table 2.1 Properties of the color stacks

Bin	z	depth	N_{clu}	color	band
1	0.07-0.23	$m^* + 2$	7	gr	r
2	0.24-0.33	$m^* + 2$	7	gr	r
3	0.33-0.42	$m^* + 2$	12	ri	i
4	0.42-0.48	$m^* + 2$	11	ri	i
5	0.53-0.70	$m^* + 2$	12	ri	i
6	0.74-0.80	$m^* + 1.7$	8	iz	z
7	0.80-0.88	$m^* + 1.7$	8	iz	z
8	0.89-1.12	$m^* + 1.2$	8	iz	z

Note – Descriptive information for the different color stacks. Here we list the bin number, the redshift range covered within the bin, the depth in terms of m^*, the number of contributing clusters as well as the color and band used within the bin. Note here that throughout the paper if not otherwise mentioned the depth corresponds to the 50 % completeness limit as derived in Sec 2.2.3. Bin 4 contains the cluster SPT-CLJ0330-5228, which has no i-band coverage and is therefore excluded in the stack.

2.4 Color Selection and Radial Profiles

In Section 2.4.1 we study the color distributions of our cluster galaxies to test whether our fiducial CSP model is a good description of the data and to explore whether the RS population is evolving over cosmic time. In Section 2.4.2 we examine the radial distribution of cluster galaxies.

2.4.1 Red Galaxy Selection

We wish to be able to study both the RS and non-RS galaxy populations as a function of redshift, and doing so means that we need to have a reliable way of selecting one or the

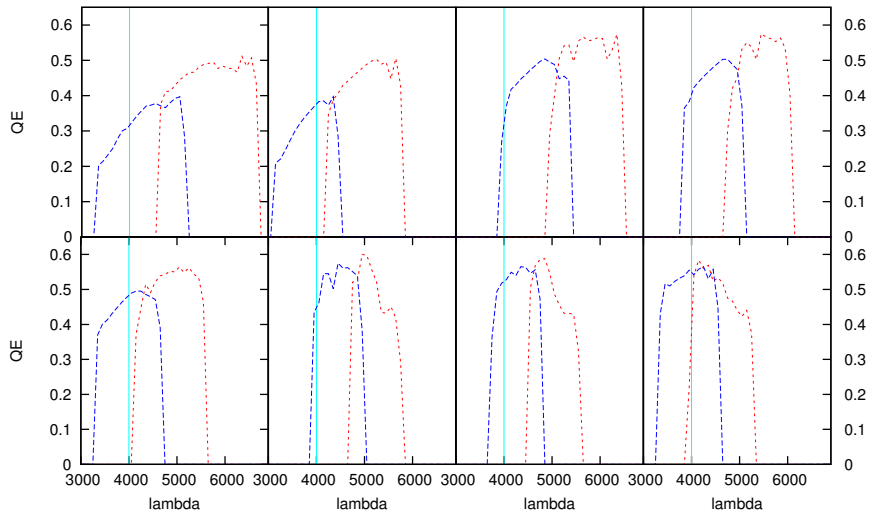

Figure 2.6 The plot shows the effective band coverage of the color combinations we use within the 8 different redshift bins as shown in Table 2.1. Each filter transmission curve for the appropriate color combination in the redshift bin is shifted towards the cluster redshift of the individual contributing clusters. The effective band coverage is then the average of the individuals. From top left to bottom right the redshift is increasing and shows the transition from $g - r$ in the first 2 panels, to $r - i$ in the following 3 panels and to $i - z$ in the last 3 panels. The blue and red lines always mark the band containing the 4000 Å break (light blue line) and the band redward of it. We note that in the highest redshift bin, the break is already included in the redward filter.

other. In the simplest case this means we need to know the typical color, tilt and width of the RS as a function of redshift. We have already shown in Section 2.3.1 that our fiducial CSP model produces photometric redshifts with no apparent biases (compared to the known spectroscopic redshifts), and that this serves as a confirmation that the color evolution of the RS in our CSP model is quite consistent with that in our cluster sample. To test the RS tilt and measure any evolution in width we combine information from subsamples of ~ 10 clusters within redshift bins and use these stacks to test our model. Stacking the clusters helps to overcome the Poisson noise in the color-magnitude distribution of any single cluster, allowing the underlying color distribution of the galaxies to be studied more precisely.

Table 2.1 contains a description of the different redshift bins within which we stack the clusters. The table shows the redshift range of the clusters in the bin, the depth to which we are able to study the color-magnitude distribution, the number of clusters in each bin, and the color and band combinations used. We attempt to study the color distribution to a fixed

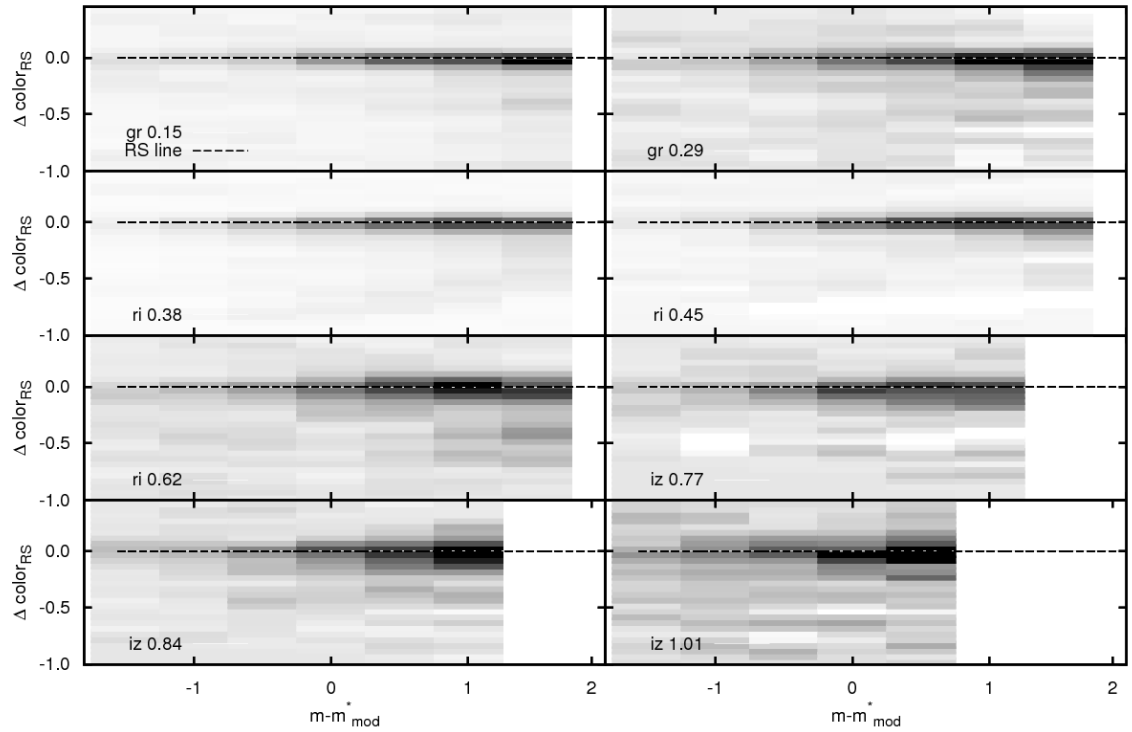

Figure 2.7 Stacked cluster galaxy color–magnitude distributions for the 8 different redshift bins defined in Table 2.1. The magnitude scale is defined relative to the $m^*(z)$ of our passive evolution model, and the color offset is defined with respect to our tilted RS model (see Section 2.3.1). The color coding describes the completeness corrected and background subtracted number density of galaxies per magnitude and color bin. A common grayscale was used for all redshift bins, where black refers to a high number-density of objects, whereas white presents a lower number-density. The RS is clearly apparent at all redshifts, extending cleanly to $m^* + 2$ in the lower redshift bins. At higher redshift the distribution of galaxies bluer than the RS grows more prominent, and the RS becomes weaker at magnitudes $m > m^* + 1.2$.

depth corresponding to 2 mag fainter than the characteristic magnitude $m^*(z)$. However, given the depth of the DES-SV data we are only able to study galaxies to $m^* + 1.2$ in the highest redshift bin and $m^* + 1.7$ in the two next to highest redshift bins. We also wish to study the same portion of the spectral energy distribution (SED) in each redshift bin, and therefore we focus in each bin on the band containing the 4000 Å break and the band redward of that band (see Figure 2.6). Here again, in the highest redshift bin we have to compromise and use $i - z$ even though a more appropriate band combination would be $z - J$.

To construct the individual cluster color-magnitude distributions, we measure the color of each galaxy relative to the color of the tilted RS at that redshift and its magnitude relative to the characteristic magnitude $m^*(z)$. We combine all galaxies that lie within a projected radius R_{200} and make a statistical background correction using the local background region inside an annulus of $1.5 - 3R_{200}$. The stacked color distribution is then the average of the color distributions of the individual clusters in the bin; we normalize this distribution to sum

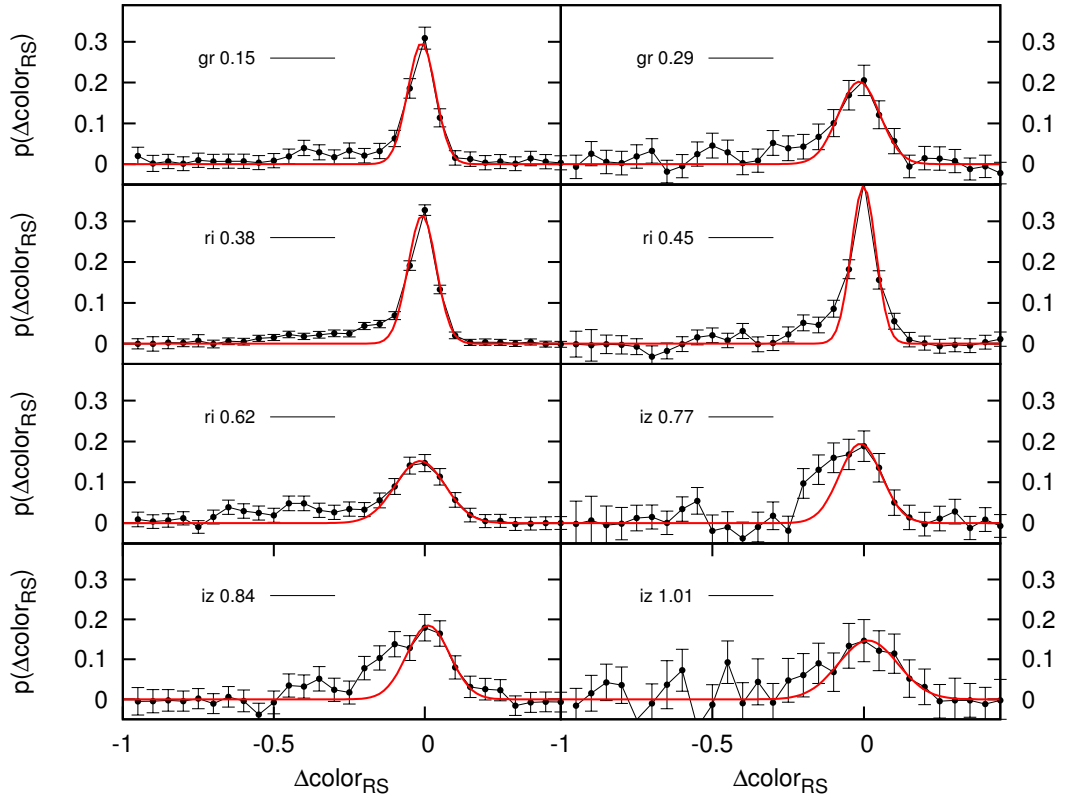

Figure 2.8 Stacked cluster galaxy color distributions for 8 different redshift bins defined in Table 2.1 and in same order as in Figure 2.7. The band combination and redshift of the stack are noted in the upper left of each panel. All distributions are normalized to unit area, and the color distributions are measured relative to the tilted RS of our fiducial model to a depth of $m^* + 2$ in all but the three highest redshift bins. The RS color distribution is fit to a Gaussian model. The RS population has high contrast out to redshift $z \sim 0.8$ and thereafter becomes more indistinct from the blue cloud at the highest redshifts probed here.

to 1.

The resulting normalized and stacked color-magnitude distributions are shown in Fig 2.7. The locations of high cluster galaxy density are shown in black and low density in white. All eight redshift bins have the same greyscale color range, allowing one to compare galaxy densities not only within a bin but across bins. The location of the RS as defined by our CSP model lies along the line where the color difference with the RS is zero. In all panels there is a strong RS with an associated bluer galaxy population. The contrast of the RS drops with redshift (note here that this drop is not due to incompleteness at that depth, as we correct each individual cluster according to its completeness as described in Section 2.2.3).

The observed contrast is sensitive both to the cluster galaxy population and the density of background galaxies in the relevant locations of color-magnitude space. Beyond $z \sim 0.8$ there appears to be a much more significant blue population than in the lower redshift bins. This is due to possible evolution of the red fraction, which we come back to in Section 2.4.4. In addition, the RS population extends over a range of magnitude to $m^* + 2$ in the lower redshift bins but shows up less strongly at the faintest magnitudes in the two highest redshift bins. Note that over the full redshift range there is no apparent tilt of the stacked color-magnitude distribution with respect to the tilt of our CSP model.

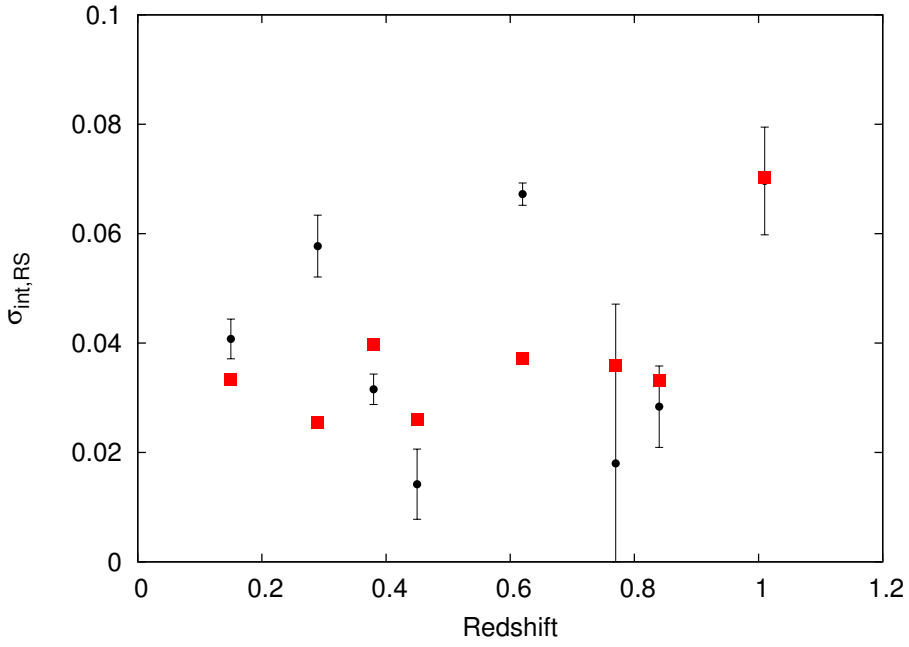

Figure 2.9 Evolution of the intrinsic width of the RS with redshift. The black points show the derived intrinsic scatters constrained from the measurements. The red points marks the scatter as it would be seen in a reference restframe, which is the $g - r$ color at redshift 0. The data allow for a mild increase of RS scatter with redshift.

To further increase the signal to noise ratio to study the color distribution of the cluster galaxies, we integrate over magnitude. Figure 2.8 contains these projected galaxy color distributions in each of the eight redshift bins. Points show the relative galaxy number-density and the RS is modeled as a Gaussian in red. We find that the offset of the RS gaussian is consistent with 0 within 1σ for most of the redshift bins or otherwise within the central bin. Thus the RS Gaussian is nicely centered at the RS color of our CSP model. There is evidence that the width of the RS gaussian grows larger to higher redshift, and its contrast relative to the blue galaxy population falls. As discussed below, this growth in RS width is due to both changes in the intrinsic width and increased measurement uncertainty in the fainter galaxies. The RS population is dominant at lower redshift, where the blue cloud

appears as an "extended wing" to the RS population, and at $z > 0.89$ the blue cloud and RS are roughly of comparable amplitude.

It is important to remember that this is the background subtracted galaxy population projected within R_{200}, and so galaxies associated with the cluster that lie in front and behind the cluster virial region are included. This makes it non-trivial to use the red Gaussian to constrain the red fraction within the cluster virial region. However, both of these figures provide a visual verification that the simple, fiducial BC03 CSP model we have adopted is providing a good description of the RS color and tilt over the full redshift range.

In the analyses that follow we examine the full cluster population and also the RS population. When examining the RS population we assign an individual galaxy in the j-th redshift bin a likelihood of being an RS member that depends on its color c_i and on the color distribution from the corresponding stack:

$$P_{i,j} = \frac{A_{r,j} \exp -\frac{(c_i - c_{r,j})^2}{2\sigma_{r,j}^2}}{P_{measured,i,j}} \tag{2.4}$$

where $A_{r,j}$ denotes the amplitude of the Gaussian, $\sigma_{r,j}$ the width and $c_{r,j}$ the central color offset of the RS. $P_{measured,i,j}$ denotes the measured color distribution at the given color i and in the j-th redshift bin. In the analyses that follow each galaxy is weighted with this likelihood, enabling us to carry out a meaningful study of the RS population over a broad redshift range accounting for variation in intrinsic scatter and also some changes in the color measurement uncertainties.

The stacked color distributions in Figure 2.8 provide constraints on the change of the intrinsic scatter of the RS. To extract the intrinsic scatter we determine the color measurement uncertainty σ_{col} to produce an estimate of the intrinsic width $\sigma_{int,j}$ of the RS within the j-th redshift bin

$$\sigma_{int,j}^2 = \sigma_{r,j}^2 - \sigma_{col,j}^2 \tag{2.5}$$

In order to get an idea of the systematic error in *mag_detmodel* colors for our coadd catalogs and to calculate $\sigma_{col,j}^2$, we processed 2 coadd tiles in the Supernova survey field with exactly the same position, but with each tile being constructed with different sets of exposures. Each of these tiles has about 10 exposures. We then compared the *mag_detmodel* colors from the two tiles as a function of *mag_auto*. Fitting a simple power law relation, we know the *mag_detmodel* color scatter as a function of magnitude $f(mag_i)$. We determine the 10σ depth for the 2 coadd tiles as well as for all the cluster tiles. Note that the 10σ depth represents the magnitude for which the median magnitude error equals 0.1. In order to account for the depth difference between the Supernova fields and the typical cluster field, we fit the power law as a function of $m - m_{10\sigma}$, where $m_{10\sigma}$ denotes the 10σ depth of the Supernova fields. Then for each redshift bin we determine the mean 10σ depth of the clusters contributing in the bin. From the color stacks in Fig 2.8 we have a measure of the number of galaxies in magnitude bins within the magnitude range between $m^* - 2$ and $\sim m^* + 2$. We define this as $N(mag_i)$ where mag_i is the magnitude associated with bin i. Then we estimate the measurement contribution to the color width as:

$$\sigma_{col,j} = \Sigma_i N(mag_i) * f(mag_i - m_{10\sigma,j}) / \Sigma_i N(mag_i) \tag{2.6}$$

where $m_{10\sigma,j}$ denotes the mean 10σ depth of all clusters within the j-th redshift bin. Thus the color measurement uncertainty is basically a weighted sum of the variances as a function of magnitude.

Figure 2.9 is a plot of the redshift variation of the intrinsic width of the RS. Note that we are measuring RS scatter in $g-r$, $r-i$ and $i-z$ over this redshift range. As mentioned earlier, this allows us to extract a measurement from a similar portion of the galaxy rest frame SED, independent of the cluster redshift. The 4000 Å break is included in the blueward color band in every bin (except for bin #8 where we would need $z-J$) as shown in Figure 2.6. Because the RS width reflects the diversity of the stellar populations and extinction within the passively evolving component of the cluster galaxy population, it provides a constraint on the variation in metallicity and star formation histories. Often the width of the red sequence is interpreted in terms of constraints on the age variation in the stellar populations (e.g. Hilton et al. 2009). In our case the contributions to the width include not only the intrinsic population and extinction variations but also the systematic color variations among clusters combined into a stack, photometric redshift uncertainties and mismatch of the adopted passive evolution model used to correct clusters within a redshift bin to a common color-magnitude space.

Characteristically, the RS intrinsic width increases mildly from about $\sim$40 mmag at $z = 0.15$ to about $\sim$70 mmag at $z = 1$. Increasing RS scatter has also been seen in other recent studies (e.g. Hilton et al. 2009; Mei et al. 2009; Papovich et al. 2010). As these studies correct to a restframe $U - V$ color and do not report an evolutionary fit on their individual cluster data, we restrict ourselves to a qualitative comparison. Summarized in Papovich et al. (2010), the RS scatter shows typical values of $\sim$25 mmag at $z \sim 0$ and increases towards $\sim$140 mmag at redshift 1.62; this trend is comparable to the behavior we measure in our SZE selected cluster sample. We want to measure a restframe color scatter and account for the scatter that is introduced from using different color combinations within the full redshift range. We thus need to additionally correct to one restframe color that is appropriate for our sample. We choose the $g - r$ color at redshift $z = 0$ as a reference restframe. We then build a library of template SEDs using the code `GALAXEV` from Bruzual & Charlot (2003). We use star formation models with an exponentially decaying starburst and explore different decay times. For each of these decay times we extract a set of $\sim$ 200 ages each. In total our library contains around 5000 template SEDs. Note that we exclude models with ages older than the age of the Universe. Then for each redshift bin we randomly extract template SEDs drawn from a gaussian with a mean $m*$ color and intrinsic width at the corresponding redshift. For this set of individual SEDs we then calculate the colors from a convolution of the SED with the reference filter transmission curve. This color distribution as seen in the restframe filters is then fit by a gaussian. We mark the difference between the scatter in the observed frame and the scatter in the reference-restframe by red points in Fig 2.9. We note that further increasing the library of template SEDs did not change the measured restframe scatters significantly.

The general trend of increasing scatter about the RS as a function of redshift is expected if the stellar populations are non-coeval and were formed at high redshift, evolving passively thereafter. In such a scenario the width increases as one approaches the redshift of formation. Additional theoretical modeling beyond the scope of our current paper would be required to interpret these observational constraints.

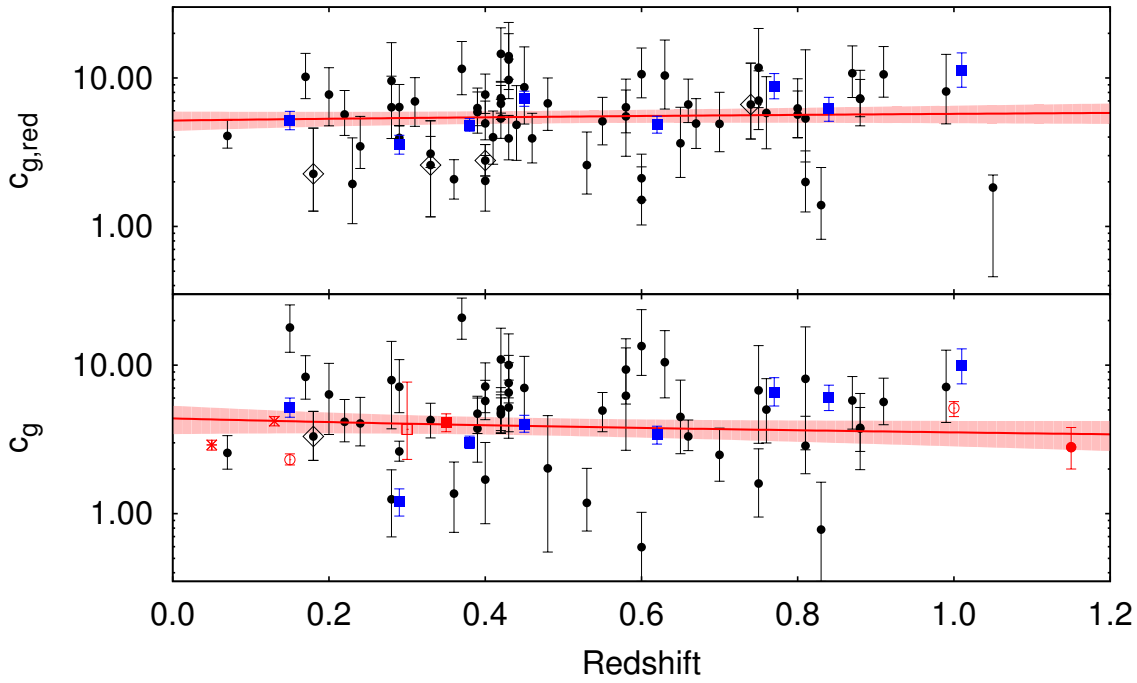

Figure 2.10 Evolution of the concentration parameter for the full and Red Sequence population. The black points show the best fit NFW concentration parameters for individual clusters, where c_g is for the full and $c_{g,RS}$ is for the RS population. All profiles are centered on the BCG. The line shows the best fit redshift trend (see Table 2.2) with 1σ uncertainty region (see Equation 2.11). The characteristic concentration for the full population is $c_g = 3.89 \pm 0.52$, less than that for the RS population $c_{g,RS} = 5.47 \pm 0.53$. The red points show various published results from Capozzi et al. (2012) (red cross), Popesso et al. (2006) (red cross), Lin et al. (2004) (red star), Carlberg et al. (1997) (red open square), Muzzin et al. (2007a) (red filled square) and van der Burg et al. (2014a) (red open circles). In addition, we mark the clusters close to the Large Magellanic Cloud ($\delta < -63°$) as black open diamonds. Blue points show the corresponding results from the stacked profiles.

2.4.2 Radial Distribution of Galaxies

We study the radial profile of the galaxies because it is one of the core properties of the population, but we also need the radial profile to enable a statistical correction for the cluster galaxies that are projected onto the cluster virial region but actually lie in front or behind it. To construct the radial profile we measure the number of galaxies lying within annuli centered on the cluster. We adopt the BCG position as the cluster center. For this analysis BCGs are selected manually through visual inspection of the pseudo-color images. If there is no clear, centrally located BCG we adopt the brightest galaxy within $0.5 * R_{200}$ that has a color within 0.22 mag of the RS color at that redshift and is located closest to the SPT center. In 8 cases, this BCG definition leads to the selection of a bright foreground galaxy,

and in these cases we exclude those galaxies and select a fainter BCG candidate.

The radial profile extends to between $\sim 4R_{200}$ and $\sim 14R_{200}$, given the $1^\circ \times 1^\circ$ or $2^\circ \times 2^\circ$ tiles we prepared for each cluster. Thus, in all cases it includes a background dominated region. We correct in the individual profiles for bright stars that contaminate the cluster and background areas. For each profile annulus we calculate an effective area by subtracting off the star areas that are contaminating the bin. Further details can be seen in the Appendix. Bright stars are selected from the 2MASS survey using a magnitude cut of $J < 13.5$. We use an empirical calibrated relation between the J-band magnitude and the masking radius of the star to exclude spurious objects. For the profile analysis we use galaxies that are brighter than $\sim m^*+2$ and the band redward of the 4000 Å break, except again in the highest redshift bins where our imaging depth does not allow analysis to the full depth and in the highest bin where z band contains the 4000 Å break. All profiles are completeness corrected as described in Section 2.2.3.

We fit these profiles to the NFW (Navarro et al. 1997) density profile with the concentration as one of the free parameters. The three dimensional NFW profile is given as:

$$\frac{\rho(r)}{\rho_c} = \frac{\delta_c}{(r/r_s)(1+r/r_s)^2} \tag{2.7}$$

where $\rho_c = 3H_0^2/8\pi G$ denotes the critical density of the Universe, δ_c is a characteristic density contrast and r_s is the typical profile scale radius. As mentioned above we use a density contrast of $\Delta = 200$ for the virial density. The concentration parameter for the NFW profile is obtained as $c = R_{200}/r_s$. For using the surface density we need to project the three dimensional profile along the line of sight (Bartelmann 1996).

Our model profile is the superposition of the cluster profile Σ_{cl} and a constant background Σ_{back}:

$$\Sigma(x) = \Sigma_{cl} + \Sigma_{back} \tag{2.8}$$

Consequently the formula for the projected NFW profile has 3 free parameters: the normalization, the flat constant background and the scaleradius r_s (or, equivalently, the concentration c). We follow Lin et al. (2004) in adopting the integrated number of galaxies within R_{200} as the normalization. This avoids the parameter degeneracy between the concentration and the central density and results in improved constraints on the concentration. For the errorbars on the number counts of galaxies per radial bin we use Cash (1979) statistics to represent the true underlying Poisson errorbar. The fitting of the profile is consequently done using the counts per bin, rather than the number-density per bin. We additionally avoid using the observed counts at the bin-center, but rather fit the model as $N(R_{up}) - N(R_{low})$, where $N(R_{up})$ is the integrated number of galaxies inside a projected cylinder with an outer radius of R_{up}, and $N(R_{low})$ is the equivalent inside a cylinder of Radius R_{low}. Due to the star-masking we are missing galaxies inside the radial bin and we need to correct the modelled number of galaxies with the ratio A_{eff}/A_{true}, where A_{eff} is the effective bin area (after star-masking), and $A_{true} = \pi(R_{up}^2 - R_{low}^2)$ represents the true bin area. As the measured number inside a radial bin is the superposition of cluster galaxies and background galaxies, we further need to add the background contribution with $N_{bg} * A_{eff}$. In each radial annulus we measure the

number of observed galaxies, calculate the effective area and fit a model that reads

$$N(r) = (N(R_{up}) - N(R_{low}))\frac{A_{eff}}{A_{true}} + N_{bg}A_{eff} \tag{2.9}$$

From integrating the Surface Density, $N(R_{up})$ becomes

$$N(R_{up}) = 4\pi\rho_s r_s^3 * g(x)$$

$$g(x) = \begin{cases} \frac{2}{\sqrt{(x)^2-1}} arctan\sqrt{\frac{x-1}{x+1}} + ln(\frac{x}{2}) & \text{if } x > 1, \\ \frac{2}{\sqrt{1-(x)^2}} arctanh\sqrt{\frac{1-x}{1+x}} + ln(\frac{x}{2}) & \text{if } x < 1 \\ 1 + ln(\frac{x}{2}) & \text{if } x = 1 \end{cases}$$

where $x = cR_{up}$. $N(R_{low})$ is calculated correspondingly.

The profile fitting is done with the Markov chain Monte Carlo (MCMC) Ensemble sampler from Foreman-Mackey et al. (2013). As the distribution for the concentration parameter is lognormal, we fit for $ln(c)$.

We test the profile generation and the fitting procedure on a sample of mock catalogs with a concentration of $c = 5$. We build a big mock with 500000 galaxies as a first start to see if our code returns unbiased results when having significantly strong signal. We then draw 100 individual realizations with different numbers of cluster galaxies, that is 100,500,1000,2000 and 4000 galaxies. We find that even in the low Signal-to-Noise regime with just 100 cluster galaxies (which is typical also for the SPT sample we probe here), we can fully recover the input concentration with an inverse variance weighted mean of 4.95 ± 0.16. The normalization is recovered as well within the 1σ errorbars. Using Cash (1979) statistics allows the radial bins to be infinitesimally small. Yet as the background determination is sensitive to the background binning, we use bins of 0.02 inside R_{200}, and start increasing the binsize outside. We find that an overestimation of the background leads to overestimated concentrations, and therefore it is very important to fit a region extending to large enough radius to constrain both the background and the cluster model. In particular, we find that it is important to go well beyond $2R_{200}$, which is fulfilled with the DESSV data. Consequently we have demonstrated that our profile fitting code and approach are unbiased to within the statistical uncertainties in our test.

We fit a simple power law to the concentration parameter of the individual cluster profiles simultaneously in mass and redshift. Because this approach is used in the other observables examined below, we define the relation here for a generic observable $O(M_{200}, z)$ as:

$$O(M_{200}, z) = A\left(\frac{M_{200}}{M_{piv}}\right)^B \left(\frac{1+z}{1+z_{piv}}\right)^C \tag{2.10}$$

where A is the normalization, B is the mass power law parameter and C is the redshift power law parameter. We choose a mass pivot point $M_{piv} = 6 \times 10^{14} M_\odot$, which is the median mass of our sample, and a redshift pivot point $z_{piv} = 0.46$, which is the median redshift of our sample. In addition to these three parameters we constrain the intrinsic scatter of these quantities by adopting an intrinsic scatter parameter σ_{int}. With this intrinsic scatter

the uncertainty on a given parameter measurement becomes the quadrature addition of the intrinsic and measurement uncertainties. We iterate our fit, adjusting the intrinsic scatter until the reduced χ^2 for the fit approaches 1.0. These best fit parameters and estimates of the intrinsic scatter are listed in Table 2.2.

Table 2.2 Mass and Redshift Trends for the Radial Profile parameters
$M_{piv} = 6 \times 10^{14} M_\odot$, $z_{piv} = 0.46$

Obs	A	B	C	σ_{int}
c_g	3.89 ± 0.52	-0.32 ± 0.18	-0.31 ± 0.45	0.55
$c_{g,stack}$	4.83 ± 1.16	-1.13 ± 0.65	0.78 ± 0.76	0.45
$c_{g,RS}$	5.47 ± 0.53	-0.01 ± 0.10	0.15 ± 0.30	0.38
$c_{g,RS,stack}$	6.14 ± 0.98	-0.32 ± 0.25	0.60 ± 0.35	0.22
N_{200}	74.3 ± 3.8	0.73 ± 0.09	-0.31 ± 0.29	0.05
$N_{200,red}$	46.5 ± 2.9	0.72 ± 0.13	-0.37 ± 0.38	0.10
f_{red}	0.67 ± 0.03	-0.09 ± 0.08	-0.30 ± 0.26	0.25

Note – Best fit mass and redshift trends for the galaxy concentration c, the Number of galaxies N_{200} within the virial sphere as well as the red fraction f_{red} from the full and RS population. The columns list the observable, as well as the best fit normalization, mass slope and redshift slope of the power law in Equation 2.10. The last column shows the intrinsic scatter of the best fit relation. Note that these scatters (except for the red fraction) are derived in log-space, and are thus fractional scatters.

Using the best fit parameters and parameter uncertainties we use Gaussian error propagation to express the uncertainties as:

$$\begin{aligned}\frac{\sigma_O^2}{O^2}(M_{200}, z) =& \frac{\sigma_A^2}{A^2} + \left(\log \frac{M_{200}}{M_{piv}}\right)^2 \sigma_B^2 \\ &+ \left(\log \frac{(1+z)}{(1+z_{piv})}\right)^2 \sigma_C^2\end{aligned} \tag{2.11}$$

where the parameter errors are extracted from the covariance matrix of the fit. We use this uncertainty to define a confidence region about the best fit relations when they are presented in the figures below.

Fitting this power law (Equation 2.10) to the concentration data, we find that the characteristic concentration for the full population is $c_g = 3.89 \pm 0.52$ at pivot mass $M_{piv} = 6 \times 10^{14} M_\odot$ and pivot redshift $z_{piv} = 0.46$. There is no significant evidence for a redshift and $\sim 1.8\sigma$ mass trend in this sample of similar mass clusters (see Table 2.2). Note here that we exclude clusters with declination $\delta < -63°$, which are close to the Large Magellanic Cloud (LMC), from the fit, as their virial area is significantly contaminated by stars. While the star-galaxy separation is effective at removing single stars, it fails for any binary stars that are present. These binary stars that leak into our galaxy sample can then impact our

results if their surface density varies over the field and background region of the cluster. In all cases we show results on these LMC clusters with black open diamonds in the following figures. Figure 2.10 (lower panel) contains a plot of the galaxy population concentration for each cluster versus the cluster redshift. Measurements from the literature are plotted in red with different point styles, and there is good agreement between the previous results and our own (Carlberg et al. 1997; Lin et al. 2004; Popesso et al. 2006; Muzzin et al. 2007a; Capozzi et al. 2012; van der Burg et al. 2014a). Measurements from the stacks are shown with blue squares.

We use the same technique to measure the profiles for the RS galaxy population, but in addition we assign each galaxy a probability of being a RS member as described in Equation 2.4. The concentration evolution is shown in Figure 2.10 (top panel). The characteristic concentration at our pivot mass and redshift is $c_{g,RS} = 5.47 \pm 0.53$. We do not find statistically significant mass and redshift trends for the RS galaxy population within the errorbars.

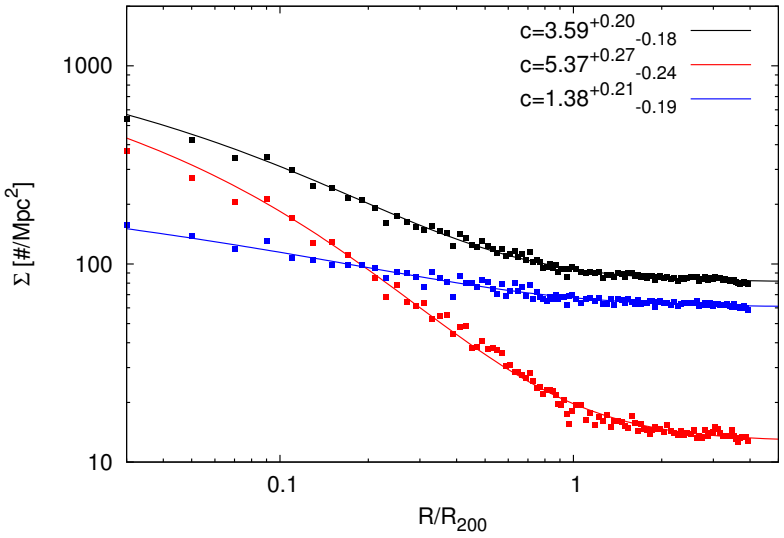

Figure 2.11 The black (and red) points show the stacked radial profile for the full (and red) population. These stacks contain all clusters in the sample except for SPT-CLJ0330-5228, which has no i-band coverage. The profile is in dimensionless units R/R_{200}. All individual profiles extend to $4R_{200}$. The full population is less concentrated with $c_g = 3.59^{+0.20}_{-0.18}$ compared to the RS population with $c_{g,RS} = 5.37^{+0.27}_{-0.24}$. We also show the "blue" non-RS population which is selected blueward of the RS and with a galaxy weight of $1 - P_{i,j}$ in Equation 2.4. The blue population is less concentrated with $c_{g,non-RS} = 1.38^{+0.21}_{-0.19}$.

We also study the radial profile of the stacked clusters for the full and the RS populations. For the stacks we sum the numbers of galaxies and the corresponding areas within each radial bin. This sum is then averaged by the number of contributing clusters inside the bins. In contrast to the individual cluster fits we also have enough signal to show results on the blue non-RS population. The blue non-RS population is selected to have a color that is blueward from the cluster RS and each galaxy is weighted with $1 - P_{i,j}$ as in Equation 2.4. These

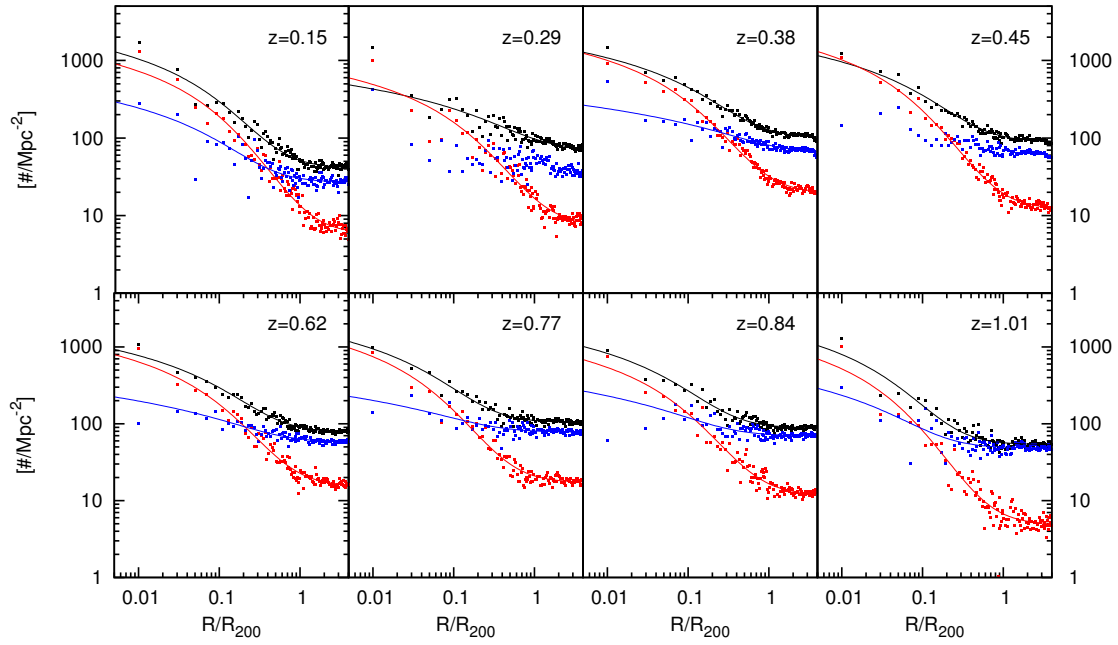

Figure 2.12 The color coding is similar to Fig 2.11, yet the stacks are shown within the 8 different redshift bins. Again all profiles extend to $4R_{200}$. The concentration results for the stacks are shown also in Fig 2.10 for the full and RS population. In each redshift bin we find that the blue non-RS population is less concentrated than the full population, which is less concentrated than the RS population. Yet the non-RS blue background is higher than the RS background. Note that the blue population in redshift bin 2 and 4 was unconstrained due to large scatter.

stacks are shown in Figure 2.11 and for the 8 different redshift bins in Figure 2.12 with black (red and blue) points for the full (RS and non-RS) population. All individual profiles extend to a common flat background out to $4R_{200}$. Again we find that the full population is less concentrated with $c_g = 3.59^{+0.20}_{-0.18}$ compared to the RS population with $c_{g,RS} = 5.37^{+0.27}_{-0.24}$. The blue population is even less concentrated with $c_{g,non-RS} = 1.38^{+0.21}_{-0.19}$ (see Figure 2.11). The same picture arises in each redshift bin as seen in Figure 2.12. Yet the non-RS blue background is higher than the RS background. Note that the blue population in redshift bin 2 and 4 was unconstrained due to large scatter. Furthermore half of the sample of individual blue RPs was unconstrained, which is why we do not report an evolutionary fit on the blue non-RS population. From a quantitative perspective we find an increase in the red fraction over cosmic time by looking at the decreasing blue background density between $\sim 0.8 - 4R_{200}$. The evolution of the red fraction will be discussed in further detail in Section 2.4.4. The best fit relation for the evolution of the concentration with the stacked data is

also shown in Table 2.2. The mass and redshift trends from the stacks are consistent with those from individual clusters within the 1σ error bars. (Note that for the mass constrain on stacked cluster data we use the mean mass of the clusters contributing to the redshift bin). Yet the stacked cluster data seem to prefer increasing concentration with redshift.

In summary, our data show that the red, early-type galaxies tend to have a more concentrated distribution, which is consistent with previous analyses where a higher concentration is seen in the red galaxy population (e.g. Goto et al. 2004). Spectroscopic studies of individual clusters also support this picture that there is a flatter distribution of emission line galaxies centered on the cluster whose virial region is strongly marked by a more concentrated distribution of absorption line systems (e.g. Mohr et al. 1996).

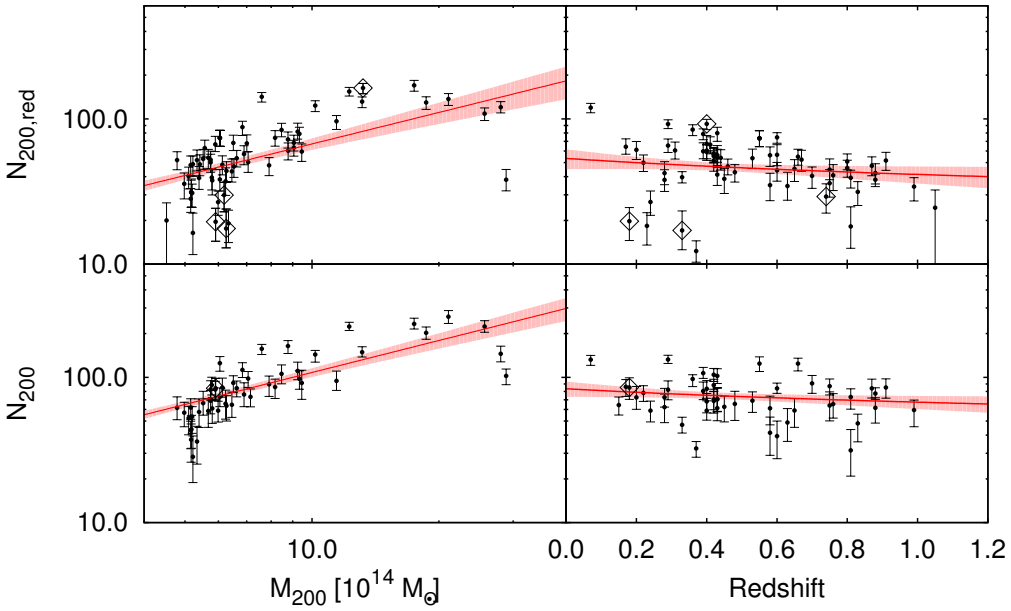

Figure 2.13 The HON from constraints of N_{200} is plotted versus mass (left panels), and the HON normalized to a mass of $6 \times 10^{14} M_{\odot}$ is plotted versus redshift (right panels). In both cases the full (RS) population appears on bottom (top), and both populations have $N_g \propto M^{\mu}$ where $\mu < 1$ (fit parameters in Table 2.2). We find no clear evidence of redshift evolution in the full and RS population. The 1σ region (Equation 2.11) for each fit is plotted in red. The LMC clusters with $\delta < -63°$ that are highly contaminated by stars are marked with black open diamonds.

2.4.3 Halo Occupation Number

The Halo Occupation distribution (HOD hereafter) describes the relation between galaxies and dark matter at the level of individual dark matter halos (Zheng et al. 2005). In particular,

the HOD provides an insight into how baryonic matter is distributed within each of the dark matter haloes. A key feature here is the relation between the Halo Occupation number (HON hereafter) and the given mass of the dark matter halo. A simple prediction based on galaxy formation efficiency would be that the number of galaxies formed is proportional to the baryonic mass within the halo. The HON-mass relation becomes $N_g \sim M^{\mu}$ with $\mu > 1$ if galaxy formation is more efficient in the more massive haloes, or $\mu < 1$ the other way around. Reasons for $\mu < 1$ might be that gas, which is heated through the collapse of the halo may not effectively collapse into galaxies. In addition, dynamical friction and tidal stripping can have an impact on the HON, which is typically measured above a magnitude threshold (Rines et al. 2004; Lin et al. 2004).

Here we calculate the HON directly from the N_{200} of the individual profile fits. We correct the measured N_{200} inside the virial cylinder to the virial sphere. Therefore we calculate the ratio C from the integration of the projected surface number density inside a cylinder and sphere as

$$C = \frac{N_{cyl}(R_{200})}{N_{sph}(R_{200})} \tag{2.12}$$

As our profiles have units of r/R_{200} these integrals are simply a function of the concentration c. For a concentration of 3 this factor is of the order of 1.3.

Figure 2.13 is a plot of the measured HON for each cluster versus mass (left) and redshift (right) for the full population (bottom) and RS population (top). The best fit power law parameters (Equation 2.10) describing these data appear in Table 2.2. The characteristic HON at our pivot redshift $z_{piv} = 0.46$ and mass $M_{piv} = 6 \times 10^{14}\, M_{\odot}$ is 74.3 ± 3.8 for the full population and 46.5 ± 2.9 for the RS population. This is an indication that the red fraction at the pivot mass and redshift to $m^* + 2$ is $63 \pm 8\%$. The mass trend for the full population $N_{200} \propto M^{(0.73 \pm 0.09)}$ is consistent with the RS population, where we find $N_{200,red} \propto M^{(0.72 \pm 0.13)}$. The full population shows weak evidence of $1\,\sigma$ to decrease with redshift. The RS population also shows a decrease in redshift, yet this trend is not statistically significant. Concerning outliers of the relation, we note that we examined the images of 5 clusters with an HON above 250 galaxies. In 3 cases the images show a comparable amount of possible cluster galaxies. In 2 other cases the clusters are in the vicinity of the LMC and have a medium star field contamination. It might be possible that the Star-Galaxy separation is not reliably distinguishing between binary stars that leak into the galaxy cluster catalog. Concerning 5 low HON outliers with a number of galaxies below 50, we note that 4 of these clusters looked sparsely populated in the pseudo-color-image and had redshifts above 0.6. The other cluster was in the SPT-west region, which was observed to shallower depth than SPT-East.

We find agreement at 1σ in the mass trend with $\mu = 0.70 \pm 0.09$ (Rines et al. 2004). Yet there are other studies who found a steeper mass trend with $\mu = 0.87 \pm 0.04$ in Lin et al. (2004) or $\mu = 0.92 \pm 0.03$ in Popesso et al. (2007). Comparing the normalization to the local sample at $z \sim 0.05$ of Lin et al. (2004), we have a normalization that is in 1.4σ agreement within our errorbars. Here we correct for the difference between $m^* + 3$ in the Lin et al. (2004) analysis and $m^* + 2$ in our dataset. Yet our lowest redshift cluster SPT-CLJ0431-6126 is in 1σ agreement within the errorbars of the local Lin et al. (2004) relation.

As with the other power law fits, we extract constraints on the variation of the HON from cluster to cluster for both the RS and full populations. We find a 5% intrinsic scatter in N_{200} around the best fit relation for the full population, and a 10% intrinsic scatter for the RS population. This evidence of scatter is corrected for the Poisson sampling noise and background correction uncertainties that are included in the RP parameters.

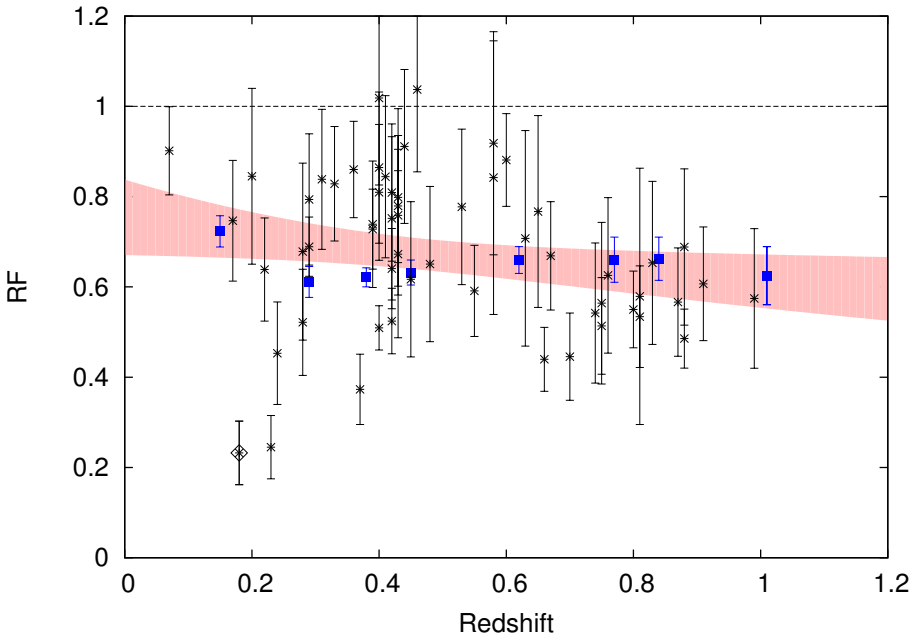

Figure 2.14 Red fraction within the virial sphere of radius R_{200} as a function of redshift. The red fraction f_{red}^{N} comes from the individual measurements of N_{200} from the RPs of the full and RS population. The typical galaxy red fraction at the pivot redshift $z_{piv} = 0.46$ with intrinsic variation at the 25% level is $67 \pm 3\%$. The best fit redshift trend is shown with the red band corresponding to the 1σ confidence region for the fit (Equation 2.11). The data suggest a mild evolution in red fraction over cosmic time within the errorbars. The blue points represent the projected red fraction extracted from the stacked radial profiles in Figure 2.12 within the 8 different redshift bins. The LMC clusters are marked with open diamonds.

2.4.4 Red Fraction

For studying the evolution of the red fraction, we look at the galaxy population out to $\sim m^* + 2$ that lies within the cluster virial sphere. Specifically, we calculate the ratio $f_{red}^{N} = N_{200,red}/N_{200}$, which describes the galaxy population near $m^* + 2$ from the constraints of the RP measurements. Note here that these measurements are corrected to the viriral sphere with Equation 2.12. As shown in Section 2.4.1 the RS galaxies are selected with a probabilistic approach based on stacked color distributions in 8 redshift bins. It is possible for the red

fraction estimate for a single cluster to scatter above 1, as the fits on the data may not necessarily be a good reflection of the integrated counts. Additionally we derive red fraction measurements from the stacked radial profiles within the 8 different redshift bins as seen in Figure 2.12.

A plot of the red fraction estimator versus redshift appears in Figure 2.14. The red area represents the best fit function, and the best fit parameters are given in Table 2.2. The blue points show the measurements from the RP stacks. We find that at $z = 0.46$, the median redshift of our sample, the red fraction is $f_{red}^{N} = (67 \pm 3)\%$, which is in agreement with the derived best fit values of the HON in Section 2.4.3. The red fraction is mildly evolving within the statistical errorbars at 1.2σ significance. We find a decrease in red fraction with $\sim 80\%$ at redshift 0.1 down to $\sim 60\%$ at redshift 1. We further note that the 3 clusters with the lowest red fractions below 40% are close to the LMC (declination < -61), where there is medium star field contamination.

The observed redshift trends in the red/blue fractions has been interpreted as an evolution in the galaxy population due to ram-pressure stripping (Gunn & Gott 1972), galaxy merging (Moore et al. 1996), or changes in the rate of infalling galaxies from the cluster outskirts and the field (Ellingson et al. 2001). The time evolution of the red fraction thus constrains the combined effects of infall of blue galaxies from the field and the transformation of these to passive, red cluster galaxies.

In a recent analysis, McGee et al. (2009) examine the buildup of cluster and group galaxy populations through accretion from the field and from subclusters within the standard hierarchical structure formation scenario. They find, for example, that $\sim 40\%$ of the galaxies within massive clusters like those we study here fall into the cluster as members of lower mass subclusters. The remainder of the population is accreted from the field. They examine various scenarios where once a field galaxy falls into a group or cluster halo it begins a transformation from a typical star forming field galaxy to a typical passively evolving RS cluster galaxy. Examining different timescales for this environmental change, they show that the evolution of red fraction over cosmic time is quite sensitive to the transformation timescale t_{trunc} (McGee et al. 2009, Figure 9). Examining these results, we estimate that the red fraction evolution in this SPT selected cluster sample indicates a relatively long timescale of $t_{trunc} \sim 2 - 3$ Gyr for environmental effects to transform the infalling star forming galaxies into passive RS galaxies. While the uncertainties in our red fraction evolution are significant and the intrinsic scatter is large with 25%, our sample exhibits very different character from the expectations for a transformation taking place on 1 Gyr or 4 Gyr timescales (McGee et al. 2009). In comparison to our results, the recent phase space analysis of the high redshift IR selected sample of groups and clusters (GCLASS) favors short quenching timescales of ~ 0.5 Gyr (Muzzin et al. 2014). This quenching is indeed only the first step in the transformation of a field galaxy to an RS galaxy, and therefore we would expect the transformation timescale to be longer. In combination, our results suggest rapid quenching upon first infall into the cluster and then the dying away of the last generation of massive young stars on a timescale of $\sim$2 Gyr.

It is important to note that there have been studies where the redshift evolution of the red/blue fraction was either weaker or not existent (e.g. Smail et al. (1998)), and various selection biases were considered as possible drivers for the trend. Cluster samples that are

uniformly selected using a property that does not involve their galaxy populations, that span a large redshift range, and that come with reasonably precise virial mass estimates are therefore desirable to provide maximal leverage to evolutionary studies. The precise and accurate cluster mass estimates are critical so that one is comparing similar portions of the cluster virial volume at different redshifts and masses. From this perspective the SPT selected sample we study here offers advantages over some previous studies. This analysis will benefit significantly from extension of the cluster sample when the DES survey is completed.

2.5 Discussion and Conclusions

We present results from a study of a sample of 74 SPT selected clusters within the DES-SV survey area whose redshifts extend to $z \sim 1.1$. The combination of the deep DES data and this SZE selected cluster sample provides a unique opportunity to systematically study the galaxy population and its redshift and mass trends in high mass clusters over a wide range of redshift. Each of these clusters has a robust mass estimate that derives from the cluster SZE detection significance and redshift; these masses include corrections for SZE selection effects and account for the remaining cosmological uncertainties and unresolved systematics in the combined X-ray and velocity dispersion mass calibration dataset (Bocquet et al. 2014). Our masses lie in the range of $4.3 \times 10^{14} M_{\odot} \leq M_{200} \leq 2.9 \times 10^{15} M_{\odot}$. Within the cluster virial region R_{200}, we study the redshift and mass dependencies of the galaxy radial profiles and the red fraction.

In our study we examine both the full galaxy population, identified through statistical background subtraction, and the RS galaxy population, identified using red sequence color selection together with statistical background subtraction. To enable the RS selection and to measure cluster photometric redshifts, we adopt a CSP model (Section 2.3.1) with a burst beginning at $z = 3$ and an exponential decay time of 0.4 Gyr; initially, we calibrate six models with different metallicities to the red sequence of the Coma cluster (Zenteno et al. 2011; Song et al. 2012a,b).

In section 2.4, we divide our sample into 8 redshift bins with approximately 10 clusters in each bin, and stack them in color-magnitude space to examine the RS location and width. We find that the red sequence location and tilt of our cluster sample are in good agreement with this simple model. The RS is quite prominent out to redshifts $z \sim 0.8$, beyond which it broadens and becomes less prominent as the cluster blue population becomes more significant. Even at low redshifts there is a significant non-RS galaxy population in our clusters. We build simple color distributions in each redshift bin, fitting the RS population with a Gaussian model. The intrinsic width of the red sequence mildly evolves from ~ 0.04 at $z = 0.15$ to ~ 0.07 at $z = 1$ (see Section 2.4.1, Figure 2.9). This broadening is likely evidence of a greater heterogeneity of the RS population at those early times. We note here that additional modeling of the RS width as a function of metallicity and age would be required for a detailed interpretation of this observational result. In the analyses that follow, we use the fit to the projected color distribution to assign a probability that each cluster galaxy is an RS member given its measured color and the cluster redshift.

We fit the radial profiles of galaxies in this SZE selected cluster sample to NFW models

and find evidence that the concentration varies slightly with redshift and mass. Our mean concentration for the full population $c_g = 3.89 \pm 0.52$ is consistent with various literature studies. The RS galaxy population is more concentrated with a mean of $c_{g,RS} = 5.47 \pm 0.53$. We find no significant redshift evolution from individual cluster results for the full and RS population, yet there is a tendency for increasing concentration with redshift based on the stacked cluster data. Evidence for a significant redshift evolution has recently been reported in van der Burg et al. (2014a) on stacked galaxy number density profiles. The typical concentration at low redshift $z \sim 0.15$ is $c = 2.31^{+0.22}_{-0.18}$, whereas at redshift $z \sim 1$ they find $c = 5.14^{+0.54}_{-0.63}$. The observed trends in the cluster galaxy profiles is quite different from the behavior seen in N-body simulations for the structure of the underlying dark matter halos; in that case N-body simulations indicate that one expects a decreasing concentration with increasing redshift (Duffy et al. 2008). Given the additional physics that the galaxy population is subject to, such as merging into a central giant galaxy, there is no strong expectation that N-body results would describe the evolution of the galaxy profiles. Indeed, dynamical friction and tidal stripping/disruption could plausibly act to reduce the concentration of the satellite distribution over cosmic time (Budzynski et al. 2012). Moreover, as suggested recently (van der Burg et al. 2014a), the growth of the central galaxy over cosmic time could result in redshift trends in the profile of the full population. With extending the SPT selected sample for the full survey area we will likely gain in statistics and might be able to constrain an evolutionary trend for the concentration. In our masslimited sample we find no clear evidence for a strong mass-dependency of the concentration parameter, although the data seem to suggest that the concentration is decreasing as a function of mass, as expected from the DM simulations (e.g. Duffy et al. 2008).

We examine the evolution of the HON with mass and redshift. Our result for the mass trend $N_g \propto M^{0.73\pm0.09}$ is somewhat shallower than previous results from the low redshift cluster population (Lin et al. 2004), yet it is consistent at 1σ in the mass trend with $\mu = 0.70 \pm 0.09$ (Rines et al. 2004). As summarized in Capozzi et al. (2012), a value $\mu < 1$ is expected from the theoretical point of view. They note that independent of the fact that hierarchical structure formation models predict a universal mass distribution of sub-haloes, the inclusion of baryons produces a decreasing number of galaxies per unit mass (Berlind et al. 2003). Several processes may be responsible for this behavior, such as an increased merger rate, an increasing galaxy destruction rate (Lin et al. 2004) or decreasing star formation and gas cooling efficiencies (Berlind et al. 2003). Yet each of these processes should leave their own mark in the properties of galaxy clusters.
Moreover, we examine the redshift trend of the HON at fixed mass, finding a 1σ significant hint for the HON to decrease with cosmic time in the full population $N_{200} \propto (1+z)^{-0.31\pm0.29}$. Our observational-based results indicate that low redshift clusters are richer than their high redshift counterparts when comparing clusters of the same mass. The picture from different results in the literature has not yet converged: For example at low redshift a K band study by Lin et al. (2006), where 27 clusters within a redshift range of $0 < z < 0.9$ together with the local X-ray selected sample yield a powerlaw slope in redshift of $C = -0.03 \pm 0.27$. Further evidence for non-evolution in the HON is found in Muzzin et al. (2007b); Andreon & Congdon (2014). Yet Capozzi et al. (2012) find evidence for significant correlations of the observed

number of cluster galaxies with redshift and mass. In particular their redshift evolution scales as $C = -0.61^{+0.18}_{-0.20}$. The RS population shows a decrease with $N_{200,red} \propto (1+z)^{-0.37\pm0.38}$, yet it is not statistically significant within the error bars. The slightly larger decrease of the RS population hints towards a mild increase in the red fraction over cosmic time.

We examine the red fraction using the measurements from N_{200} inside the virial sphere for the full and RS populations, as well as the projected color stacks. The characteristic red fraction at the pivot mass and redshift of our sample (see Table 2.2) is $(67 \pm 7)\%$ for the full population to $m^* + 2$. The measurement of the red fraction seems to prefer mild redshift evolution at $\sim 1.2\sigma$ with a typical decrease of $\sim 80\%$ at $z = 0.1$ to $\sim 60\%$ at $z \sim 1$. Examining the results from McGee et al. (2009), we estimate that the red fraction evolution seen in this SPT selected cluster sample indicates a relatively long timescale of $t_{trunc} \sim 2 - 3Gyr$ for environmental effects to transform the infalling star forming galaxies into passive RS galaxies.

In summary our results reveal that the characteristics of the cluster galaxy populations for the RP do not change significantly since $z = 1$ within the errorbars, but show mild tendencies of evolution. We find generally good agreement with previous studies, but owing to the redshift range and sample size we are able to present more precise measurements of the population evolution. The concentration in the full population and RS population from stacked cluster data fall with cosmic time, perhaps due to merging onto and growth of the giant central galaxies. One element of our population study remaining to be explained is the decrease in color width of the RS over cosmic time. The RS width presumably constrains the heterogeneity in age and metallicity at fixed galaxy luminosity of the old stellar populations that dominate in RS galaxies. Our full set of observational results provides a resource for confronting specific galaxy formation simulations; matching the mass and redshift trends presented here should lead to significant improvements in our understanding of this process.

2.6 Appendix

Photometric redshift estimation for special cluster cases

For the following clusters the photometric redshift distribution showed multiple significant peaks either within the color used for the photometric redshift or in the other color combinations: *SPT-CLJ0001-5440*, *SPT-CLJ0107-4855*, *SPT-CLJ0330-5228*, *SPT-CLJ0412-5106*, *SPT-CLJ0422-4608*, *SPT-CLJ0422-5140*, *SPT-CLJ0423-6143*, *SPT-CLJ0426-5416*, *SPT-CLJ0428-6049*, *SPT-CLJ0433-5630*, *SPT-CLJ0444-4352*,*SPT-CLJ0446-5849*, *SPT-CLJ0456-5623*, *SPT-CLJ0502-6113*, *SPT-CLJ0509-5342*, *SPT-CLJ0550-6358*, *SPT-CLJ2259-5431*. These multiple peaks may either come from foreground / background populations, small surrounding groups or nearby clusters that fall into the redshift scaled aperture. There might be also the possibility of a projected second cluster in the line-of-sight. Such neighboring systems are clearly off-centered from the SZ-center, but contaminate the photometric redshift estimation. Yet for those systems we were able to estimate a reasonable redshift compared to the optical images.
There were 3 cluster candidates where the estimated photometric redshifts seem to be unrea-

sonable compared to the optical images: *SPT-CLJ0458-5741* shows a pronounced peak at z=0.2. Yet this is consistent with the low-redshift cluster ACO 3298 (at a separation of 77") and discussed in (Song et al. 2012b). *SPT-CLJ0423-6143* showed a group close to the cluster center within 3.8 arcmin from the SZ-center. *SPT-CLJ0430-6251* is surrounded by bright galaxies within 3 arcmin. The cluster seems to be offset by 2 arcmin from the SZ position. The bright low redshift galaxies might cause the estimated photometric redshift of 0.23 to be low compared to the published photometric redshift of 0.38 (Song et al. 2012b).
The following cluster candidates are covered within the DESSV survey footprint, but had a noisy photometric redshift distribution with no significant peak compared to the background noise in all color combinations. From a visual inspection of the equivalent images, we did not find an overdensity of galaxies within $\sim 5'$ from the SZ center position. Thus we attributed this candidates to be likely without an optical counterpart, or with a counterpart above $z \sim 1.2$ and did not use them in the analysis: *SPT-CLJ0416-4938*, *SPT-CLJ0420-5245*, *SPT-CLJ0445-4926*, *SPT-CLJ0447-5041*, *SPT-CLJ0500-4713*, *SPT-CLJ0502-5451*, *SPT-CLJ0536-6109*, *SPT-CLJ2301-5520*, *SPT-CLJ2353-5512*.
The following cluster candidates were not used due to photometric catalog problems (e.g. holes near the cluster center, cut-out regions or shallow observations) : *SPT-CLJ0008-5440*, *SPT-CLJ0332-5304*, *SPT-CLJ0357-4521*, *SPT-CLJ0404-4418*, *SPT-CLJ0408-4456*, *SPT-CLJ0501-4455*, *SPT-CLJ0634-5949*, *SPT-CLJ0643-4535*, *SPT-CLJ2242-4435*.

Radial profile generation

Given that we choose the radial annulus binsize as small as 0.02 R/R_{200}, a big star lying within the bin, can cover a significant fraction of the area with up to 10%. Especially in the cluster center, where the number of objects is small, an error in the area can potentially bias the concentration estimation. We thus try to analytically solve for the masked area to calculate an *effective* bin area.
Starting from the simple case where two circles are crossing each other the intersection area A_{int} can be calculated as

$$A_{int} = A_1 + A_2$$
$$= \frac{r^2}{2}(\beta - sin\beta) + \frac{R^2}{2}(\alpha - sin\alpha)$$

A_1 and A_2 are circular segments. The relevant angles and distances are shown in Fig 2.15. D is the relative distance between the cluster center and the central coordinates of the star (Note here that all distances are given in R/R_{200}). r represents the star-radius, R the cluster radius and α and β are the relevant angles within the triangle of these three distances. Using the law of cosines we find α and β to be calculated as:

$$\alpha = 2cos^{-1}(\frac{-r^2 + R^2 + D^2}{2RD})$$
$$\beta = 2cos^{-1}(\frac{-R^2 + r^2 + D^2}{2rD})$$

We then distinguish between four different cases as illustrated in Fig 2.16. Given the stellar

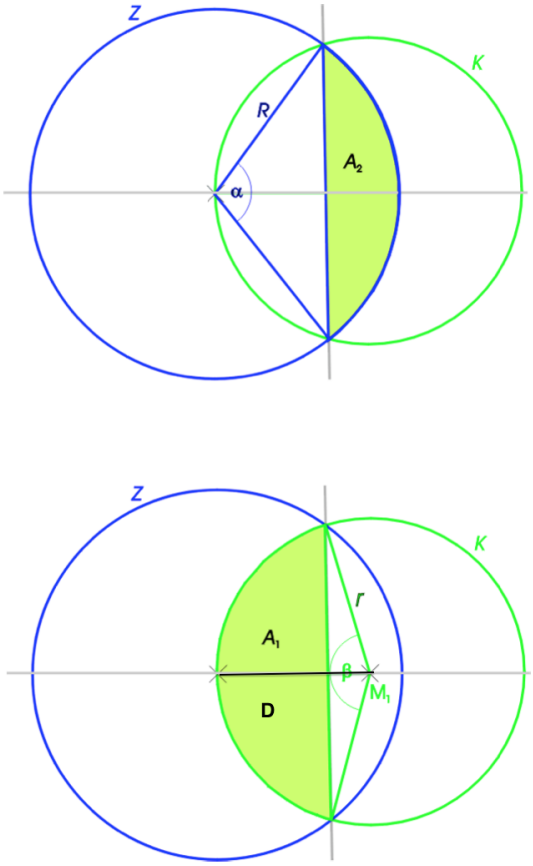

Figure 2.15 The figure illustrates how to calculate the intersection area between circle Z (seen as the cluster) and circle K (seen as an exaggerated huge star for illustration purposes). D is the relative distance between the cluster center and the central coordinates of the star (Note here that all distances are given in R/R_{200}). r represents the star-radius, R the cluster radius and α and β are the relevant angles within the triangle of these three distances.

masks from 2MASS, we then calculate for each radial bin whether the area is affected by a star 1) lying fully within the bin, 2) crossing the outer annulus, 3) crossing the inner annulus and 4) crossing the full bin. In the first case, the masked area is simply given as $A_{mask} = \pi r^2$, which is the area of the star that lies fully within the bin. In the second case, the masked area is calculated from $A_{mask} = A_{int}$ as shown above. When the star crosses the inner radius of the annulus then $A_{mask} = \pi r^2 - A_{int}$. For the last case we calculate an upper $A_{int,up}$ and lower intersection area $A_{int,low}$ based on the outer and inner radius of the bin. Then the masked area is given as $A_{mask} = A_{int,up} - A_{int,low}$.

We use this analytic expression within the maximum bin radius R_{max} that fits into the rectangular cluster tile. Yet within the rectangle we can exploit as much cluster and back-

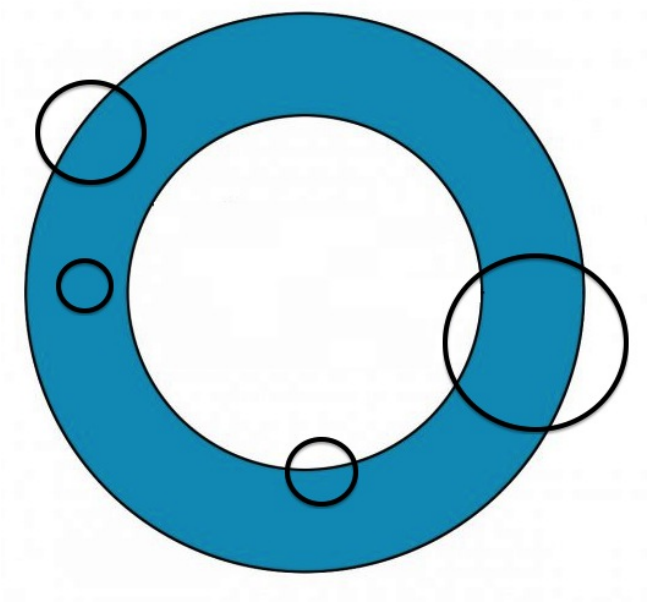

Figure 2.16 The figure illustrates the four different cases how a star can affect the area of a radial bin: the star can be 1) lying fully within the bin, 2) crossing the outer annulus, 3) crossing the inner annulus and 4) crossing the full bin.

ground area as possible by switching over to a pixel grid. We divide the given rectangular tile into small squared pixels. Then the effective radial bin area is calculated as the Number of pixels (that fall into the bin and are not part of a star-mask) times the pixel area. This will extend the cluster profile even further. Yet from our testing on mock simulated cluster profiles we choose a maximum profile radius where the fractional area loss due to star masks inside the rectangle is reaching 10%. Going even to smaller areas with a fractional loss of 50% or more, we find that the approximation with pixels is starting to bias the recovered input concentration by $\sim 40\%$.

Table 2.3 SPT Cluster Properties

clustername	RA	DEC	M_{200}	z_{photo}	c_g	$c_{g,RS}$
SPT-CLJ0001-5440	0.4071	-54.6704	$6.32\ ^{+1.47}_{-1.89}$	0.89 ± 0.03		
SPT-CLJ0001-5440	0.4071	-54.6704	$6.32\ ^{+1.47}_{-1.89}$	0.89 ± 0.03	–	–
SPT-CLJ0008-5318	2.0685	-53.3004	$5.16\ ^{+1.26}_{-1.78}$	0.39 ± 0.02	–	–
SPT-CLJ0012-5352	3.0649	-53.8736	$5.90\ ^{+1.38}_{-2.01}$	0.40 ± 0.02	$5.77^{+2.18}_{-1.46}$	$7.75^{+2.90}_{-1.98}$
SPT-CLJ0036-4411	9.1758	-44.1849	$6.13\ ^{+1.41}_{-1.82}$	0.87 ± 0.01	$5.74^{+2.59}_{-2.06}$	$10.73^{+5.65}_{-3.36}$
SPT-CLJ0040-4407	10.2048	-44.1329	$17.46\ ^{+2.91}_{-3.90}$	0.39 ± 0.01	$3.34^{+1.03}_{-0.89}$	$5.45^{+1.55}_{-1.30}$
SPT-CLJ0041-4428	10.2513	-44.4785	$10.18\ ^{+1.72}_{-2.42}$	0.36 ± 0.02	$1.15^{+0.73}_{-0.52}$	$1.94^{+0.69}_{-0.51}$
SPT-CLJ0102-4915	15.7294	-49.2611	$25.66\ ^{+4.74}_{-5.82}$	0.88 ± 0.03	$2.37^{+0.88}_{-0.73}$	$6.01^{+2.07}_{-1.48}$
SPT-CLJ0107-4855	16.8857	-48.9171	$5.34\ ^{+1.18}_{-1.86}$	0.60 ± 0.02	$13.97^{+10.59}_{-5.12}$	$10.76^{+5.42}_{-3.30}$
SPT-CLJ0330-5228	52.7287	-52.4698	$11.72\ ^{+1.94}_{-2.66}$	0.45 ± 0.02	–	–
SPT-CLJ0412-5106	63.2297	-51.1098	$6.05\ ^{+1.41}_{-1.94}$	0.28 ± 0.03	$1.25^{+0.72}_{-0.55}$	$6.35^{+3.92}_{-2.44}$
SPT-CLJ0417-4748	64.3450	-47.8139	$13.15\ ^{+2.19}_{-2.90}$	0.60 ± 0.01	$0.46^{+0.33}_{-0.20}$	$1.90^{+0.86}_{-0.55}$
SPT-CLJ0422-4608	65.7490	-46.1436	$5.42\ ^{+1.34}_{-1.83}$	0.67 ± 0.02	–	$4.99^{+2.36}_{-1.60}$
SPT-CLJ0422-5140	65.5923	-51.6755	$6.53\ ^{+1.40}_{-1.85}$	0.60 ± 0.03	–	$1.49^{+1.00}_{-0.48}$
SPT-CLJ0423-6143	65.9352	-61.7177	$5.18\ ^{+1.14}_{-1.74}$	0.63 ± 0.02	$10.99^{+6.91}_{-4.67}$	$10.59^{+7.75}_{-4.30}$
SPT-CLJ0426-5416	66.6764	-54.2763	$4.52\ ^{+1.01}_{-1.62}$	1.05 ± 0.04	–	$1.90^{+0.40}_{-1.42}$
SPT-CLJ0426-5455	66.5160	-54.9229	$8.77\ ^{+1.54}_{-2.11}$	0.66 ± 0.03	$2.93^{+0.85}_{-0.58}$	$6.31^{+3.03}_{-1.55}$
SPT-CLJ0428-6049	67.0305	-60.8292	$5.45\ ^{+1.35}_{-1.83}$	0.75 ± 0.02	–	–
SPT-CLJ0429-5233	67.4323	-52.5608	$5.16\ ^{+1.15}_{-1.77}$	0.53 ± 0.02	$1.24^{+0.87}_{-0.44}$	$2.65^{+1.77}_{-0.96}$
SPT-CLJ0430-6251	67.7094	-62.8548	$6.34\ ^{+1.46}_{-1.98}$	0.23 ± 0.01	–	$1.92^{+2.01}_{-0.88}$
SPT-CLJ0431-6126	67.8417	-61.4350	$7.60\ ^{+1.54}_{-2.13}$	0.07 ± 0.01	$2.38^{+0.73}_{-0.53}$	$3.95^{+1.10}_{-0.69}$
SPT-CLJ0432-6150	68.0525	-61.8497	$4.31\ ^{+0.99}_{-1.64}$	1.12 ± 0.04	–	–
SPT-CLJ0433-5630	68.2541	-56.5025	$5.79\ ^{+1.36}_{-1.82}$	0.70 ± 0.03	$2.52^{+1.29}_{-0.85}$	$4.93^{+3.12}_{-1.72}$
SPT-CLJ0437-5307	69.2599	-53.1206	$5.40\ ^{+1.16}_{-1.82}$	0.28 ± 0.03	$8.22^{+6.77}_{-4.36}$	$9.70^{+7.82}_{-4.28}$
SPT-CLJ0438-5419	69.5749	-54.3212	$18.65\ ^{+3.13}_{-4.16}$	0.42 ± 0.02	$3.34^{+1.04}_{-0.83}$	$5.78^{+1.88}_{-1.26}$
SPT-CLJ0439-4600	69.8089	-46.0141	$9.25\ ^{+1.60}_{-2.24}$	0.39 ± 0.01	$3.25^{+1.97}_{-1.32}$	$5.56^{+2.53}_{-1.54}$
SPT-CLJ0439-5330	69.9290	-53.5037	$6.46\ ^{+1.45}_{-1.92}$	0.43 ± 0.02	$6.37^{+4.99}_{-3.23}$	$13.90^{+9.52}_{-4.18}$
SPT-CLJ0440-4657	70.2307	-46.9654	$8.18\ ^{+1.50}_{-2.09}$	0.40 ± 0.01	$1.53^{+1.19}_{-0.76}$	$1.95^{+0.94}_{-0.73}$
SPT-CLJ0441-4855	70.4511	-48.9190	$8.78\ ^{+1.53}_{-2.07}$	0.80 ± 0.02	–	$5.93^{+3.46}_{-2.17}$
SPT-CLJ0442-6138	70.7489	-61.6418	$4.60\ ^{+1.07}_{-1.68}$	0.95 ± 0.04	–	–
SPT-CLJ0444-4352	71.1687	-43.8735	$5.68\ ^{+1.41}_{-1.92}$	0.58 ± 0.02	$9.51^{+5.84}_{-3.93}$	$6.40^{+3.49}_{-2.10}$
SPT-CLJ0444-5603	71.1136	-56.0576	$5.20\ ^{+1.27}_{-1.73}$	0.99 ± 0.04	$7.46^{+5.75}_{-3.16}$	$8.26^{+6.43}_{-3.26}$
SPT-CLJ0446-5849	71.5156	-58.8228	$7.16\ ^{+1.37}_{-1.81}$	1.11 ± 0.03	–	–
SPT-CLJ0447-5055	71.8445	-50.9227	$6.90\ ^{+1.45}_{-1.94}$	0.42 ± 0.01	$10.44^{+6.52}_{-4.14}$	$14.26^{+7.13}_{-5.06}$
SPT-CLJ0449-4901	72.2742	-49.0246	$9.06\ ^{+1.56}_{-2.11}$	0.80 ± 0.02	–	$5.37^{+2.36}_{-1.61}$
SPT-CLJ0451-4952	72.9661	-49.8796	$5.57\ ^{+1.36}_{-1.89}$	0.41 ± 0.04	–	$4.03^{+2.01}_{-1.38}$
SPT-CLJ0452-4806	73.0034	-48.1102	$5.22\ ^{+1.14}_{-1.78}$	0.44 ± 0.02	–	$4.92^{+4.14}_{-2.08}$
SPT-CLJ0456-4906	74.1212	-49.1056	$6.27\ ^{+1.37}_{-1.77}$	0.88 ± 0.02	$3.68^{+2.67}_{-1.73}$	$7.19^{+4.00}_{-2.45}$
SPT-CLJ0456-5623	74.1753	-56.3855	$5.10\ ^{+1.12}_{-1.74}$	0.65 ± 0.02	$4.72^{+3.65}_{-2.05}$	$3.71^{+2.77}_{-1.53}$
SPT-CLJ0456-6141	74.1475	-61.6838	$5.52\ ^{+1.31}_{-1.88}$	0.43 ± 0.02	$10.30^{+6.38}_{-4.12}$	$13.46^{+6.63}_{-5.00}$
SPT-CLJ0458-5741	74.6121	-57.6919	$4.79\ ^{+1.07}_{-1.86}$	0.20 ± 0.01	$6.83^{+4.22}_{-3.16}$	$7.97^{+4.11}_{-3.07}$

Table 2.4 SPT Cluster Properties continued

clustername	RA	DEC	M_{200}	z_{photo}	c_g	$c_{g,RS}$
SPT-CLJ0500-4551	75.2108	-45.8564	$5.99^{+1.31}_{-2.04}$	0.24 ± 0.02	$4.05^{+2.02}_{-1.19}$	$3.47^{+2.05}_{-1.01}$
SPT-CLJ0500-5116	75.2428	-51.2708	$7.15^{+1.49}_{-2.04}$	0.15 ± 0.02	$16.94^{+7.11}_{-5.41}$	–
SPT-CLJ0502-6048	75.7229	-60.8113	$5.16^{+1.13}_{-1.74}$	0.83 ± 0.02	$0.82^{+0.89}_{-0.46}$	$1.42^{+1.12}_{-0.58}$
SPT-CLJ0502-6113	75.5450	-61.2320	$5.38^{+1.32}_{-1.80}$	0.80 ± 0.02	–	–
SPT-CLJ0504-4929	76.0069	-49.4854	$6.63^{+1.54}_{-2.08}$	0.22 ± 0.01	$4.02^{+1.67}_{-1.07}$	$5.61^{+2.52}_{-1.56}$
SPT-CLJ0505-6145	76.3966	-61.7505	$8.47^{+1.57}_{-2.20}$	0.29 ± 0.01	$6.40^{+3.35}_{-2.12}$	$6.09^{+2.55}_{-1.53}$
SPT-CLJ0508-6149	77.1637	-61.8188	$5.75^{+1.39}_{-1.96}$	0.43 ± 0.02	$5.26^{+2.78}_{-1.65}$	$3.95^{+1.68}_{-1.12}$
SPT-CLJ0509-5342	77.3374	-53.7053	$9.06^{+1.54}_{-2.16}$	0.46 ± 0.02	–	$3.71^{+1.77}_{-1.18}$
SPT-CLJ0509-6118	77.4741	-61.3067	$11.43^{+1.90}_{-2.64}$	0.40 ± 0.03	$5.83^{+2.58}_{-1.94}$	$4.55^{+1.87}_{-1.02}$
SPT-CLJ0516-5430	79.1512	-54.5108	$12.26^{+2.02}_{-2.80}$	0.29 ± 0.02	$2.09^{+0.36}_{-0.30}$	$3.59^{+0.75}_{-0.49}$
SPT-CLJ0516-5755	79.2398	-57.9167	$5.75^{+1.32}_{-1.71}$	0.91 ± 0.02	$5.73^{+2.56}_{-1.70}$	$10.64^{+5.75}_{-3.18}$
SPT-CLJ0516-6312	79.0861	-63.2083	$5.91^{+1.43}_{-2.04}$	0.18 ± 0.01	$3.33^{+1.58}_{-1.03}$	$2.27^{+2.34}_{-1.00}$
SPT-CLJ0517-6119	79.2844	-61.3181	$7.91^{+1.47}_{-1.99}$	0.81 ± 0.02	$2.62^{+1.51}_{-0.92}$	$1.92^{+1.19}_{-0.71}$
SPT-CLJ0517-6311	79.4087	-63.1990	$6.26^{+1.50}_{-2.03}$	0.33 ± 0.01	–	$2.58^{+2.54}_{-1.43}$
SPT-CLJ0529-6051	82.3493	-60.8578	$6.24^{+1.44}_{-1.88}$	0.75 ± 0.07	$6.68^{+6.69}_{-3.75}$	$11.66^{+9.75}_{-5.38}$
SPT-CLJ0534-5937	83.6082	-59.6257	$5.17^{+1.11}_{-1.70}$	0.58 ± 0.01	$6.54^{+7.18}_{-3.73}$	$5.63^{+2.85}_{-2.60}$
SPT-CLJ0539-6013	84.9558	-60.2251	$5.05^{+1.23}_{-1.70}$	0.85 ± 0.04	–	–
SPT-CLJ0540-5744	85.0043	-57.7405	$7.06^{+1.36}_{-1.83}$	0.75 ± 0.02	$1.51^{+1.08}_{-0.61}$	$6.90^{+4.03}_{-2.50}$
SPT-CLJ0543-6219	85.7564	-62.3252	$9.46^{+1.62}_{-2.27}$	0.48 ± 0.01	$1.74^{+2.21}_{-1.26}$	$6.35^{+3.07}_{-2.18}$
SPT-CLJ0546-6040	86.7342	-60.6723	$5.22^{+1.16}_{-1.75}$	0.81 ± 0.03	$8.46^{+10.47}_{-5.65}$	$5.43^{+10.33}_{-2.66}$
SPT-CLJ0549-6205	87.3344	-62.0858	$21.06^{+3.59}_{-4.73}$	0.42 ± 0.02	$3.11^{+0.91}_{-0.79}$	$6.20^{+1.83}_{-1.28}$
SPT-CLJ0550-6358	87.6827	-63.9742	$6.19^{+1.45}_{-1.89}$	0.74 ± 0.02	–	$6.60^{+5.94}_{-2.73}$
SPT-CLJ0555-6406	88.8662	-64.1032	$13.21^{+2.19}_{-2.99}$	0.40 ± 0.02	–	$2.51^{+0.70}_{-0.53}$
SPT-CLJ0655-5541	103.9137	-55.6931	$7.01^{+1.55}_{-2.07}$	0.31 ± 0.01	–	$6.82^{+3.03}_{-2.18}$
SPT-CLJ0658-5556	104.6317	-55.9466	$28.02^{+4.98}_{-6.34}$	0.33 ± 0.01	$2.59^{+0.77}_{-0.62}$	$2.52^{+0.78}_{-0.49}$
SPT-CLJ2248-4431	342.1907	-44.5269	$28.86^{+5.21}_{-6.51}$	0.37 ± 0.02	$12.54^{+4.50}_{-3.56}$	$9.37^{+4.95}_{-3.11}$
SPT-CLJ2256-5414	344.0023	-54.2431	$4.74^{+1.04}_{-1.59}$	0.75 ± 0.04	–	–
SPT-CLJ2259-5431	344.9817	-54.5297	$5.80^{+1.35}_{-1.80}$	0.45 ± 0.01	$7.11^{+4.49}_{-3.18}$	$8.70^{+7.58}_{-3.78}$
SPT-CLJ2300-5616	345.0171	-56.2807	$6.51^{+1.57}_{-2.15}$	0.17 ± 0.01	$8.13^{+3.14}_{-2.38}$	$10.07^{+4.42}_{-2.88}$
SPT-CLJ2301-5546	345.4659	-55.7760	$4.98^{+1.23}_{-1.69}$	0.76 ± 0.02	$5.33^{+3.28}_{-2.15}$	$5.95^{+4.50}_{-2.54}$
SPT-CLJ2332-5358	353.1057	-53.9676	$9.34^{+1.58}_{-2.20}$	0.42 ± 0.02	$4.37^{+1.75}_{-1.34}$	$5.04^{+1.74}_{-1.34}$
SPT-CLJ2342-5411	355.6880	-54.1890	$7.65^{+1.35}_{-1.83}$	0.98 ± 0.05	–	–
SPT-CLJ2351-5452	357.8975	-54.8828	$6.84^{+1.36}_{-1.86}$	0.43 ± 0.01	$7.26^{+2.69}_{-1.92}$	$9.53^{+3.64}_{-2.39}$
SPT-CLJ2354-5633	358.7129	-56.5548	$6.05^{+1.34}_{-1.76}$	0.55 ± 0.01	$4.94^{+1.59}_{-1.38}$	$5.11^{+2.30}_{-1.56}$

Note – The columns are summarized the following: We present for each SPT cluster, the coordinates in right ascension RA and declination DEC, the mass M_{200} in $[10^{14} M_{\odot}]$, the photometric redshift z_{photo} as well as the best fit concentration c_g (full population) and $c_{g,RS}$ (RS population). Note that for clusters where the RP was unconstrained or showed multiple peaks in the likelihood distribution we do not report a best fit.

Chapter 3

Luminosity function and Halo Occupation distribution

This chapter is a paper draft that is under internal review within DES/SPT.

3.1 Introduction

In this chapter, we report a detailed analysis of the luminosity function, halo occupation number (HON) and stellar mass fraction of the full and the color selected red sequence (RS) component of the cluster galaxy population. We examine mass and redshift trends similar to that presented in Chapter 2. We are driven by our desire to better understand the formation of massive cluster galaxy populations through accretion of subclusters and direct infall from the field. In addition, we are interested in examining whether the growth of the central galaxies over time leaves an imprint on the general cluster galaxy population.

3.2 Luminosity Function

The SPT SZE selection produces an approximately mass limited sample of clusters extending over a broad redshift range from 0 to ~ 1.1; such a sample is ideally suited for a study of the mass and redshift dependence of the luminosity function (LF). The LF $\phi(m)$ can be described by the three parameter Schechter function (Schechter 1976)

$$\phi(m) = 0.4 * ln(10)\phi^* 10^{0.4(m^*-m)(\alpha+1)} e^{[-10^{0.4(m^*-m)}]} \tag{3.1}$$

where m^* is the characteristic cut off magnitude, ϕ^* is the spatial density of galaxies [Mpc $^{-3}mag^{-1}$] and α describes the faint end power law behavior.

We restrict our study to the same portion of the LF at all redshifts to enable meaningful tests of evolution; given the depths of our data this corresponds to roughly $m < m^* + 2$ for all redshift bins except for the last, in which we can only study the LF to $m^* + 1.2$. Moreover, we use the light from a common region of the galaxy SED, choosing the band redward of the 4000 Å break. This approach follows that used above in the study of the evolution of the color distribution of cluster galaxies (see Table 2.1).

Simulations from Zenteno *et al., in prep* show that it is not possible to reliably constrain all 3 LF parameters simultaneously on individual cluster basis given the magnitude range over which we fit $(m^* + 2)$ and the number of galaxies per cluster. Thus, we approach the LF study in two stages. First, we carry out 3 parameter fits to stacked luminosity functions within 8 redshift bins listed in Table 2.1. To do so we use the MCMC Ensemble sampler from Foreman-Mackey et al. (2013). This provides characteristic m^*, ϕ^* and α in ensembles of $\sim$10 clusters as a function of redshift. Second, we study the individual clusters with 2 parameters, taking the 3rd parameter from the results of the stacked LF in the same redshift range.

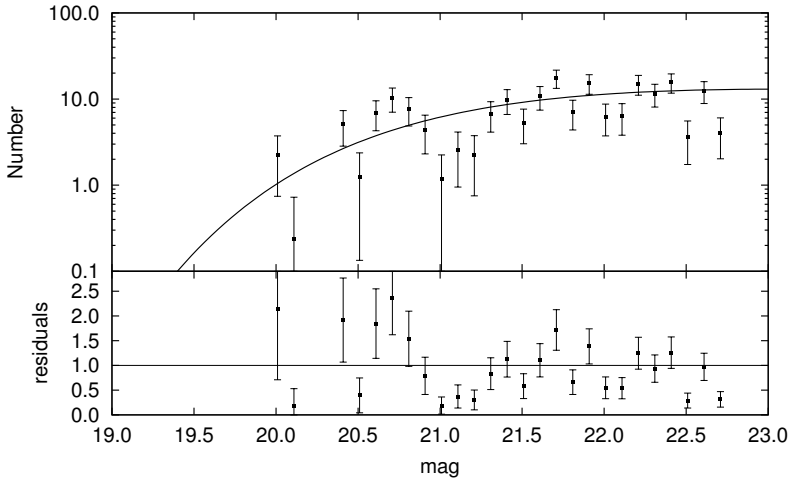

Figure 3.1 Individual cluster LF for the galaxy cluster SPT-CLJ0102-4915 at a redshift of $z = 0.87$. The upper panel shows the Number of galaxies per magnitude bin. This number includes all correction factors and the background contribution. The black line shows our best fit Schechter function when setting a prior on the faint end slope from the corresponding stacked redshift bin. We find that our model is a good fit to the data. In the lower panel we plot the residuals between data and best fit. Note that for illustration of the error bars we use $\sqrt{N}$ as the gaussian approximation.

We note that the CSP passive evolution model described in Section 2.3.1 has been validated to be consistent with the galaxy populations over the range $0 < z < 1.1$ through (1) the good performance of the red sequence redshifts (Section 2.3.1) and (2) the direct test through stacks of the color-magnitude distributions of the cluster galaxies within redshift bins (Section 2.4.1 and Figures 2.7 and 2.8). These tests indicate that the color and tilt of our model is consistent with the RS population in these clusters. Using the LFs in Section 3.2.1 below, we show that the m^* evolution of this model is also a good description of the cluster galaxy populations over this redshift range.

3.2.1 Method for Measuring Luminosity Function

We measure the LF as a superposition of cluster galaxies and background galaxies projected within the virial radius R_{200}. We exclude the BCG and all galaxies that are brighter, and we adopt a faint end limit of $\sim m^* + 2$ ($m^* + 1.2$ for the highest redshift clusters as noted in Table 2.1). When the completeness is below 100%, we apply a correction using the measured completeness as described in Section 2.2.3. Note here that this correction becomes important above $z \sim 0.9$, as the completeness can drop to ∼50%. The uncertainties for the LF reflect the underlying Poisson errors of the total number counts in each magnitude bin.

Following this approach, the number of galaxies within each magnitude bin N_{bin} is given as

$$N_{tot} = \phi * V_{200} * \Delta_{mag} * C(mag) * C_{star} * C_{cylsphere} + N_{bg} * \frac{A_{cl}}{A_{bg}} \frac{1}{C_{cont}} \tag{3.2}$$

where N_{tot} is the measured number of galaxies within R_{200} that we fit with MCMC (Foreman-Mackey et al. 2013). V_{200} represents the virial cluster volume and ϕ is the Schechter Function as described in Eq 3.1 within the magnitude bin Δ_{mag}. As we use Cash (1979) statistics for the true underlying Poisson errors, the magnitude bins can be chosen small. We use a binning of 0.1 in magnitude space. The measured number of galaxies inside the virial radius contains a contribution from the background with $N_{bg} * \frac{A_{cl}}{A_{bg}}$, where N_{bg} is the measured number of galaxies outside $1.5R_{200}$ which is rescaled to the cluster area with the ratio $\frac{A_{cl}}{A_{bg}}$. $C(mag)$ denotes the completeness correction as a function of magnitude. We further use three additional correction factors: $C_{cylsphere}$ is the correction between the virial cylinder and the virial sphere. We calculate it from integrating the NFW projected surface density profile inside the cylinder and sphere (see Equation 2.12). Therefore we assume a fixed concentration of 3.59 for the full population and 5.37 for the RS population which we have determined in chapter 2 from the stacked cluster data. The correction C_{star} accounts for missing galaxies due to star masks. The central density of galaxies is larger than in the cluster outskirts. Thus a star mask close to the cluster center implies a larger loss of galaxies. Using the star masks from 2MASS we assume an NFW profile with the above given concentrations for full and RS population and calculate the fraction of missed galaxies. This correction factor is typically on the order of $\sim 5 - 10\%$. The third correction factor accounts for cluster contamination inside the background region. We do expect cluster galaxies located outside $1.5R_{200}$, although their numbers are small. This correction is as well calculated with an NFW profile and fixed concentration within the limits of $1.5R_{200}$ and R_{max}, where R_{max} is the maximum radius inside the rectangular tile. Typically as we can exploit the large DESSV tiles with $1x1deg^2$ each, this correction factor is small with $< 5\%$.

We probe for biases in our code using a sample of 100 mock catalogs (Zenteno et al., in prep). The simulated LF has a faint end slope of -1.2 in all bands, a normalization $\phi^* = 3.3\, Mpc^{-3} mag^{-1}$, which corresponds to a halo occupation number (HON) of 335 for a cluster of mass $M_{200} = 1.3 \times 10^{15} M_{\odot}$. The characteristic magnitude is set using our CSP passive evolution model. The magnitude limit extends down to $m^* + 2$. Our tests show that our method returns an unbiased estimate of the input parameters within the statistical uncertainties either using a prior on alpha or m^*. Yet we find that when using a prior on the characteristic magnitude the constrain on the other parameters is improved within the

errorbars.

LFs for the RS population use the same method, but each galaxy is weighted according to its probability of lying within the red sequence (Equation 2.4). An example LF with the best fit can be seen in Figure 3.1.

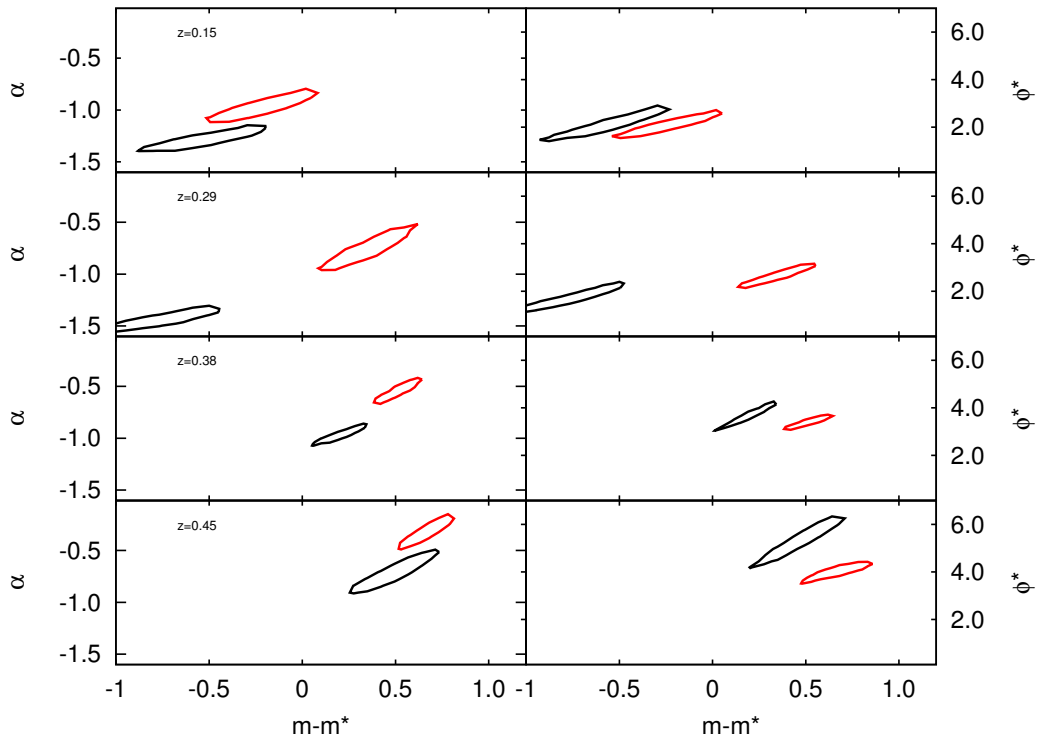

Figure 3.2 This figure shows the best fit 1σ contours in the space of α and $m - m^*$ on the left and in the space ϕ^* and $m - m^*$ on the right. The 4 rows represent the first 4 redshift bins from 0.15 to 0.45. The black line represents the full population and the red line the RS population. We note that the faint end slope is flattening with increasing redshift. Additionally the characteristic galaxy density is increasing with redshift.

3.2.2 Composite Luminosity Functions

We construct composite LFs by stacking the individual cluster LFs within each of the 8 redshift bins defined in Table 2.1. Given the number of clusters in each redshift bin, this improves the signal to noise relative to the single cluster LF by approximately a factor of three. Within each redshift bin we stack the individual LFs in the space of $m - m^*$. Stacking in $m - m^*$ accounts for K-corrections, intrinsic evolution and increasing distance with redshift. But this stacking requires that the CSP passive evolution model is accurate in a relative sense over the redshift width of the bin, which ranges from $\delta z = 0.06$ up to $\delta z = 0.23$ in the highest

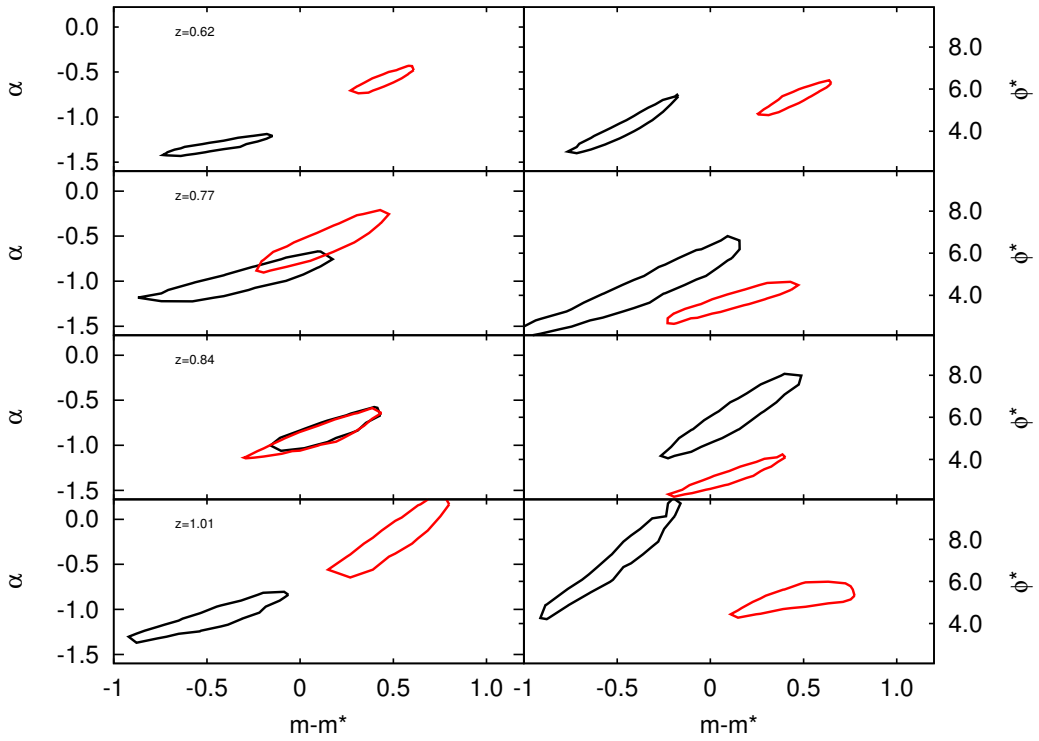

Figure 3.3 This figure presents the other 4 redshift bins ranging from 0.62 to 1.01. It is continued from Fig 3.2. The color coding of this figure is in analogy to Fig 3.2. Again we see that the characteristic galaxy density seems to increase with redshift. Especially for the RS population the faint end slope seems to steepen over cosmic time.

redshift bin. A larger cluster sample would allow for narrow redshift bins over the full redshift range of the sample.

In the stacked LF analysis we have adequate signal to perform a 3 parameter fit on the data. We get the best fit on the stacked LF by summing up the logarithmic Likelihoods from the individual clusters and use that as a probability distribution for MCMC.

Figure 3.2 and Figure 3.3 contain the results of the LF within each of the redshift bins. Both the best fit 1σ contours of the full population (black line) and the RS population (red line) are shown. The derived composite α values for the full population lie in the range of [-1.48; -0.77] and are consistent with those from the literature (-1.50; -0.58, see summary in Popesso et al. 2006). The mean faint end slope of all composite LFs for the full population is $\alpha = -1.14$. De Propris et al. (2013) conclude that their derived composite LFs are consistent with passive galaxy evolution and a faint end slope of $\alpha \simeq -1$ using 11 HST I-band imaged clusters at $0.2 < z < 0.6$, which is comparable with our result.

The results in Table 3.1 of the fits to the composite LFs indicate that the evolution of m^* in both the full and the RS populations is largely consistent with the passive evolution model

Table 3.1 Composite Luminosity Function Parameters

bin	z	$m^* - m^*_{mod}$	ϕ^*	α
1	0.15	$-0.60^{+0.26}_{-0.45}$	$2.01^{+0.70}_{-0.88}$	$-1.31^{+0.12}_{-0.15}$
1-RS		$-0.25^{+0.25}_{-0.37}$	$2.04^{+0.59}_{-0.63}$	$-0.99^{+0.15}_{-0.18}$
2	0.29	$-0.85^{+0.25}_{-0.45}$	$1.50^{+0.63}_{-0.69}$	$-1.48^{+0.10}_{-0.15}$
2-RS		$0.31^{+0.19}_{-0.29}$	$2.55^{+0.54}_{-0.66}$	$-0.80^{+0.20}_{-0.21}$
3	0.38	$0.18^{+0.14}_{-0.18}$	$3.62^{+0.57}_{-0.62}$	$-0.98^{+0.10}_{-0.11}$
3-RS		$0.50^{+0.12}_{-0.15}$	$3.37^{+0.29}_{-0.37}$	$-0.56^{+0.13}_{-0.13}$
4	0.45	$0.43^{+0.18}_{-0.29}$	$5.16^{+0.86}_{-1.27}$	$-0.77^{+0.17}_{-0.25}$
4-RS		$0.66^{+0.15}_{-0.19}$	$3.99^{+0.32}_{-0.44}$	$-0.34^{+0.18}_{-0.21}$
5	0.62	$-0.50^{+0.19}_{-0.34}$	$3.94^{+1.07}_{-1.45}$	$-1.34^{+0.09}_{-0.12}$
5-RS		$0.43^{+0.14}_{-0.21}$	$5.49^{+0.71}_{-0.76}$	$-0.61^{+0.15}_{-0.17}$
6	0.77	$-0.56^{+0.30}_{-0.84}$	$3.47^{+1.61}_{-2.71}$	$-1.13^{+0.19}_{-0.43}$
6-RS		$0.12^{+0.36}_{-0.37}$	$3.78^{+0.82}_{-0.97}$	$-0.58^{+0.36}_{-0.33}$
7	0.84	$0.02^{+0.27}_{-0.51}$	$5.51^{+1.42}_{-2.61}$	$-0.94^{+0.23}_{-0.36}$
7-RS		$-0.02^{+0.22}_{-0.49}$	$2.78^{+0.83}_{-1.38}$	$-0.99^{+0.23}_{-0.33}$
8	1.01	$-0.60^{+0.32}_{-0.54}$	$6.22^{+2.72}_{-3.55}$	$-1.19^{+0.22}_{-0.34}$
8-RS		$0.48^{+0.31}_{-0.34}$	$5.34^{+1.00}_{-0.57}$	$-0.24^{+0.50}_{-0.45}$

Note – Descriptive information for the different stacked LFs. Here we list the bin number, the redshift of the bin, the difference between $m - m^*$ for our model, the characteristic density ϕ^* and the faint end slope. All these parameters are derived from a 3 parameter fit using MCMC.

described in Section 2.3.1, although we note that the full population seems to be brighter than the model with a small offset of ~ 0.3 mag. In addition, the characteristic magnitude m^* of the RS galaxies tends to be fainter, on average, by $\Delta m^* \sim 0.6$. There is also a mild tendency for the faint end slope α to be steeper at lower redshift. At all redshifts the LF of the RS population lies below that of the full population, and there is a tendency for the RS population to have a less steep faint end slope. The characteristic density ϕ^* of m^* galaxies increases with redshift, and the tendency for the RS population to have a lower ϕ^* than the full population seems to increase with redshift. We examine these trends in detail in the following section, where we extract constraints from individual clusters.

Additionally to test our RS selection we create region files and pseudo-color images of our color-selected galaxy population as shown in Fig 3.4 and in Fig 3.5. Red circles mark galaxies with at least 40% chance to be part of the cluster RS population. Blue circles present non-RS galaxies; this population is primarily made up of blue galaxies, but it can also include galaxies

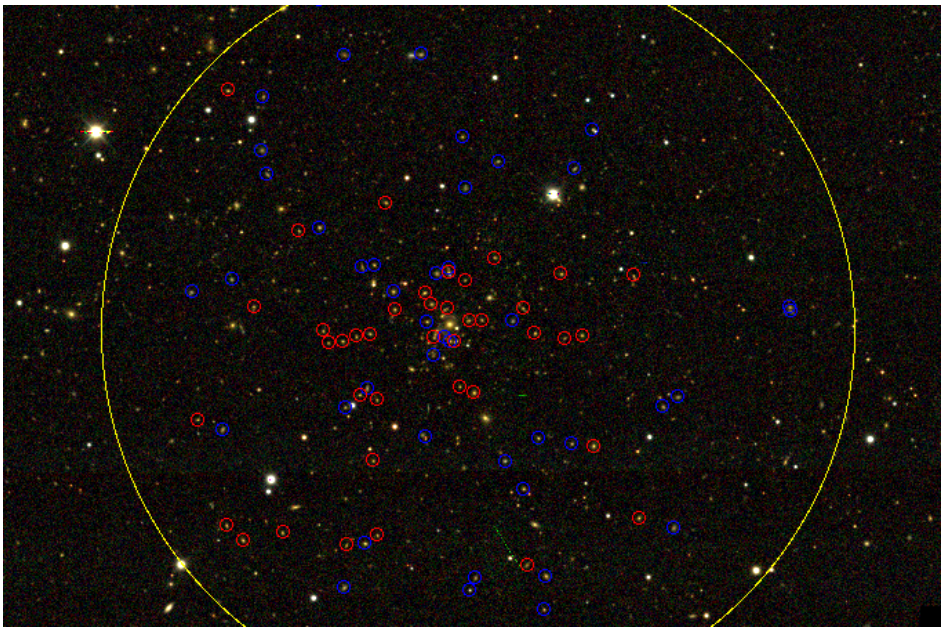

Figure 3.4 Optical pseudo-color image of SPT-CLJ2351-5452 at redshift 0.43. The yellow circle marks the cluster virial region defined by R_{200}. Small red circles mark galaxies with more than 40% likelihood of being RS galaxies. Blue circles mark galaxies with less than 40% chance to be part of the RS. Note that these galaxies can be either bluer than the given cluster RS or redder. We find that the RS galaxies tend to be centrally concentrated and that the majority of non-RS blue galaxies is located in the outskirts of the cluster, suggesting that this population is currently infalling into the cluster. All marked galaxies are within a magnitude limit of $[m^* - 0.8; m^* + 0.6]$.

redder than the RS. Furthermore we identify a population of brighter non-RS galaxies, that might still migrate towards the RS. The yellow circle in Fig 3.4 marks the R_{200} region. We confirm by visual inspection that the color selection based on the projected color stacks in Sec 2.4.1 is reasonably separating the RS population from the blue cluster population. For the majority of clusters, we find that the RS galaxies are more centrally concentrated. Looking at the spatial distribution of the non-RS population we find that blue galaxies tend to be more numerous in the outskirts of the cluster. This suggests that this population is produced by ongoing infall from luminous field galaxies into the cluster.

3.2.3 Mass and Redshift Trends

In the following three subsections we use individual cluster LF parameter measurements to constrain mass and redshift trends in the LF parameters for both the full galaxy population and the RS galaxy population. We use the same power law relation in mass and redshift introduced in Equation 2.10, and the results are presented in Table 3.2.

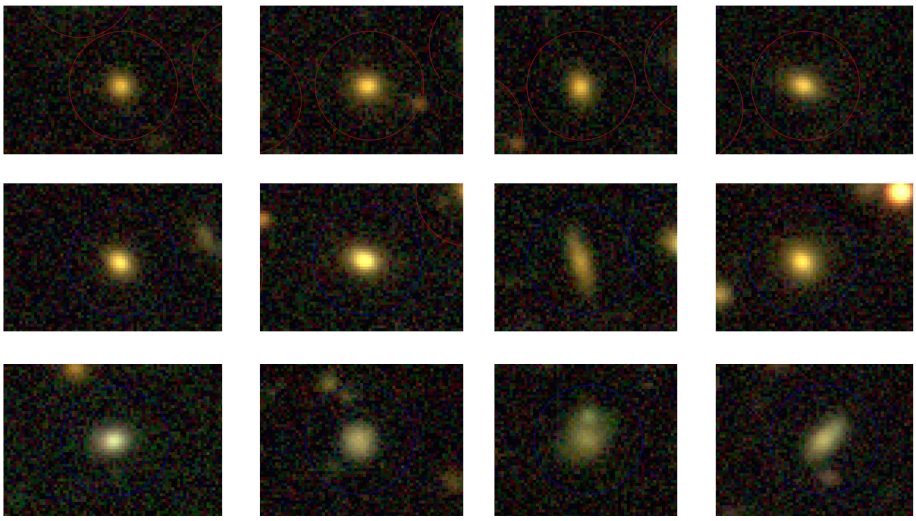

Figure 3.5 Image gallery of galaxies selected with Equation 2.4. These galaxies are in the field of SPT-CLJ2351-5452 inside R_{200}. The top row shows 4 examples of highly probabilistic RS galaxies with a likelihood above 90%. All galaxies show the same color which are consistent with the cluster RS. The second row shows galaxies with a chance of around 40% to be part of the RS. We note that these represent a bright "blue" galaxy population with galaxies that are similar to S0 galaxies, but whose colors are just not red enough to be part of the RS. We might describe them as part of a migrating population towards the RS. In the third row we show galaxies with a likelihood of below 20% change to be on the RS. The majority of these galaxies are either blue spirals or red faint objects.

Characteristic Magnitude m^*

We study the evolution of m^* in our sample using a two parameter fit, where we set a gaussian prior on the faint end slope α as the best fit value from the composite luminosity function in that redshift bin. Figure 3.6 is a plot of our results. The four panel figure contains (top panels) the best fit m^* versus redshift and (bottom panels) the difference between the best fit and the predicted m^*_{mod} for our passive evolution model (described in Section 2.3.1). The left panels show results for the full population, and the right panels show results for the RS galaxy population, which is selected according to Equation 2.4. In the top panels the lines correspond to the m^*_{mod} for each band $griz$. Individual cluster results are shown with small black (bottom) or color-coded (top) dots, fits to the composite LFs appear as blue squares with error bars.

In the top panel one can see that both the full and RS populations exhibit characteristic luminosities that track the passive evolution model we have adopted. It's also clear how with a multiband survey like DES we are able to follow a similar rest frame portion of the galaxy SEDs — light redward of the rest frame 4000 Å break — by switching from r to i to z over the redshift range $0 < z < 1.1$. Moreover, the depth and dynamic range in DES allow us to study characteristic magnitudes from 14.5 to 22, corresponding to a factor of 10^3 change in

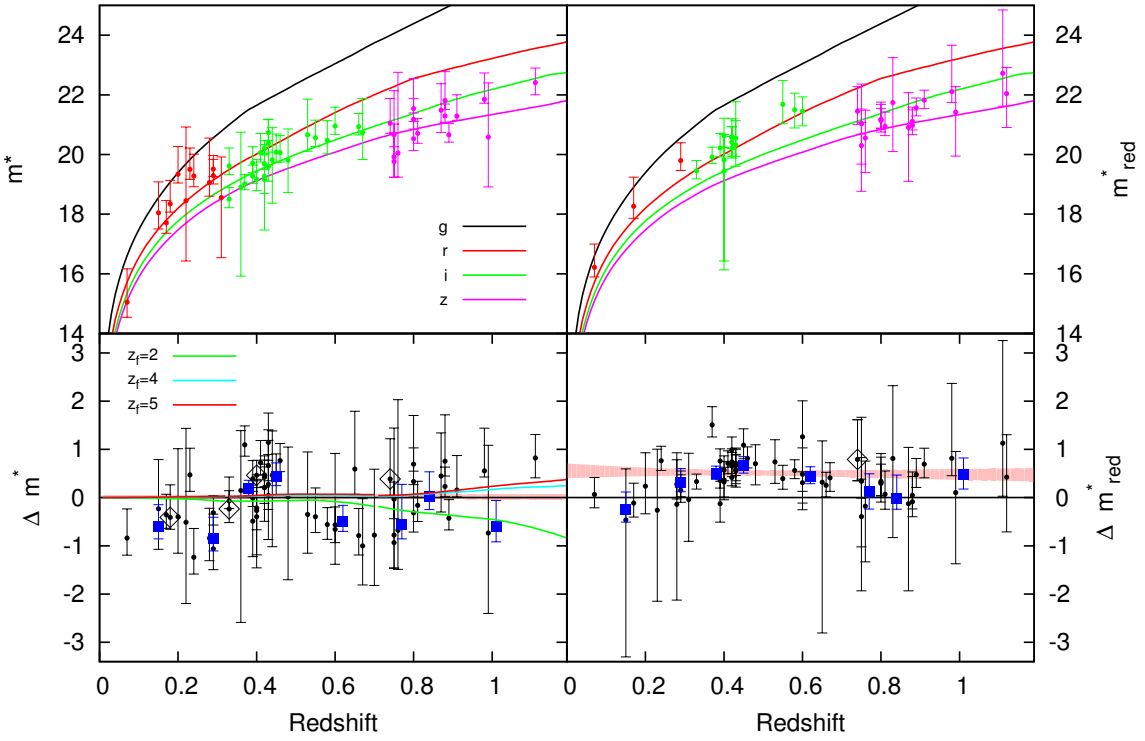

Figure 3.6 Measurements of m^* for our cluster sample appear for the full galaxy population (left panels) and the RS population (right panels). At each redshift we report m^* for the band that lies redward of the rest frame 4000 Å break, allowing us to study similar portions of the rest frame SED over the full redshift range. Individual cluster results appear as black points (bottom) or color-coded by band (top) with error bars; results from the composite LFs appear as blue squares. The LMC clusters with $\delta < -63°$ that are highly contaminated by stars are marked with black open diamonds. The top panels show m^* versus redshift along with color coded lines corresponding to the $m^*_{mod}(z)$ from our passive evolution model with formation redshift $z_f = 3$. The bottom panel contains a plot of $\Delta m^* = m^*_{fit} - m^*_{mod}$ versus redshift. Passive evolution models with different formation redshifts are also plotted. We find that the passive evolution model with a formation redshift of $z_f = 3$ is a good description of the galaxies in our SZE selected sample over the full redshift range, but we cannot distinguish between $z_f = 3-5$ within the errorbars. The best fit power law (Table 3.2) and 1σ uncertainty region (Equation 2.11) are shown in red.

flux.

Note that the original normalization extracted from comparison to Coma produced an offset between our data and the model of $< m^* - m^*_{mod} >= +0.51 \pm 0.05$ for the RS population (see Table 3.2) . This indicated that the Coma normalized model was brighter than the actual ensemble of LFs over this broad redshift range. The most interesting result is that neither the full nor the RS populations show evidence of redshift evolution in the difference between the

measured and modeled characteristic magnitudes (see Table 3.2 and red area in Fig 3.6). This is an indication that the simple passively evolving CSP performs remarkably well, showing no signs of breaking down to redshift $z \sim 1$. We note here that the evolution of the characteristic magnitude m^* is not due to incompleteness as we correct for that.

Previous studies have demonstrated that the bulk of the stars in the cluster galaxy population must have formed at high redshifts (e.g., de Propris et al. 1999). Specifically, the study of Mancone et al. (2010) found that for a passively evolving model using a Salpeter IMF, the formation redshift is strongly constrained to lie at redshifts $2 < z < 3$, whereas Lin et al. (2006) showed that that K band luminosity functions of the full galaxy population in a cluster sample extending to $z \sim 1$ prefer a formation redshift $z \sim 1.8$. Capozzi et al. (2012) in contrast to that found a good agreement with the data using a formation redshift of $z \simeq 5$.

Here we examine additional formation redshifts within $z_f = [2, 4, 5]$ for our model with $z_f = 3$ but leave the exponential decay time unchanged (see Section 2.3.1). Figure 3.6 shows the relative magnitude difference of these models compared to our primary $z_f = 3$ model. We find that out to $z \sim 0.6$ the different models show roughly the same behavior for m^* evolution, but beyond that they begin to depart from one other. The $z_f = 2$ model predicts brighter magnitudes at high redshift compared to the $z_f = 3$ model, whereas the $z_f = 4$ and 5 models predict fainter magnitudes. Performing a simple χ^2 fit on the data we find for $z_f = [2, 3, 4, 5]$ a reduced χ^2 of $\chi^2 = [1.59, 1.28, 1.28, 1.29]$. Thus within the errorbars of the individual cluster measurements the current data do not fully allow to distinguish among $z_f = 3 - 5$.

Characteristic Density ϕ^*

We extract individual cluster ϕ^* measurements with a 2 parameter MCMC LF fit using a gaussian prior on α from the composite LF fits. Given the consistency between the m^* evolution of our cluster sample and our passive evolution model (Section 2.3.1), we also study the characteristic density ϕ^* using a two parameter LF fit where we set a prior on m^* from the composite LF's. We find no significant differences between these two approaches.

Note that we extract a physical galaxy density $[Mpc^{-3}mag^{-1}]$, which we can do because the virial volume V_{200} and the virial mass M_{200} are directly related through the critical density ρ_{crit}. Because we define the virial region to be that region where the mean overdensity is 200 with respect to the critical density, and because the critical density evolves with redshift $\rho_{crit} = 3H_0E^2(z)/8\pi G$, cluster virial regions at high redshift are denser than those at low redshift. If the galaxy number per unit halo mass does not evolve with redshift, which we could adopt as the simplest self-similar evolution, then the characteristic density would evolve as $\phi^*(z) \propto E^2(z)$. Thus, rather than studying the evolution of ϕ^* directly, we study the evolution of $\phi^*/E^2(z)$.

Figure 3.7 contains a plot of our ϕ^* measurements as a function of redshift. The results from the full population appear on the bottom and the RS population on top. Black points show the results on individual clusters where α is taken from the fit to the composite LF in the same redshift bin. Blue points show the results of the three parameter fits to the composite LFs.

The best fit of these data to a power law relation in mass and redshift (Equation 2.10)

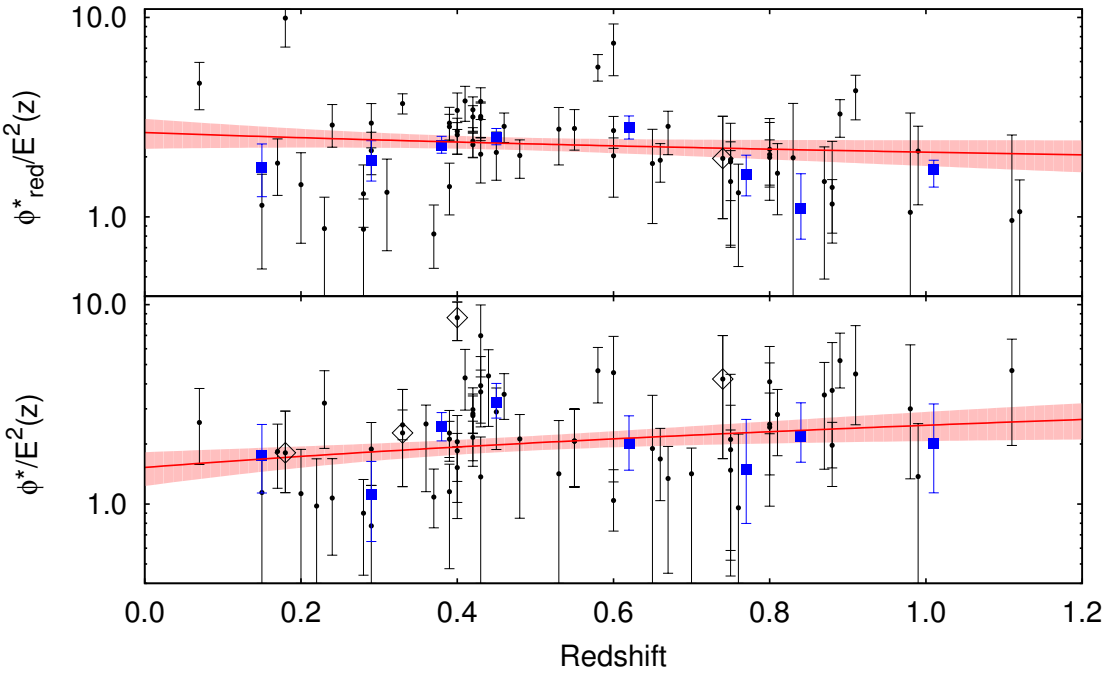

Figure 3.7 Evolution corrected characteristic densities ϕ^* $[Mpc^{-3}mag^{-1}]$ (bottom) and ϕ^*_{red} (top) extracted using α from the composite LFs are plotted versus redshift for the full and RS populations. The best fit power law (Table 3.2) and 1σ uncertainty region (Equation 2.11) are shown in red. Individual cluster results appear as black points. Results from the composite LFs appear as blue squares. The LMC clusters with $\delta < -63°$ that are highly contaminated by stars are marked with black open diamonds.

is recorded in Table 3.2. The typical density in the full population at $z_{piv} = 0.46$ is $\phi^*/E^2(z) = 1.99 \pm 0.16\, Mpc^{-3}mag^{-1}$, and the typical density for the RS population is $2.34 \pm 0.17\, Mpc^{-3}mag^{-1}$.

Interestingly, the data show a preference for ϕ^*_{red} in the RS population to increase over cosmic time, which may suggest an ongoing process of quenching of star formation underway even in the luminous galaxy population from $z = 1$ to the present. Yet within the error bars, this trend is not statistically significant. We find that the density of luminous galaxies ($m \sim m^*$) in the full galaxy population, once corrected for the evolution of the critical density, increases with redshift with 1.5σ significance. This might imply that high redshifted clusters have a higher galaxy density compared to their low redshift counterparts which can be a sign of ongoing merger activities in massive clusters. The mass trend for the RS population is not significant within the error bars, and the mass trend for the full population has only a week significance with $\sim 1.3\sigma$. As we have a mass limited sample from the SZ selection, we do not expect significant mass trends in our analysis. As seen in Figure 3.7 the results from individual clusters and the stacked LFs are in good agreement.

Table 3.2 Mass and Redshift Trends for the Luminosity function parameters $M_{piv} = 6 \times 10^{14} M_{\odot}$, $z_{piv} = 0.46$

Obs	A	B	C	σ_{int}
Δm^*	0.01 ± 0.04	2.28 ± 2.32	0.67 ± 3.61	0.27
Δm^*_{RS}	0.51 ± 0.05	-0.10 ± 0.16	-0.20 ± 0.67	0.00
$\phi^* E^{-2}$	1.99 ± 0.16	0.15 ± 0.11	0.70 ± 0.46	0.54
$\phi^*_{RS} E^{-2}$	2.34 ± 0.17	-0.11 ± 0.14	-0.33 ± 0.41	0.85
α	-1.19 ± 0.06	-0.17 ± 0.10	-0.34 ± 0.29	0.23
α_{RS}	-0.61 ± 0.06	-0.13 ± 0.18	-0.54 ± 0.58	0.21
N_g	83.8 ± 6.0	0.97 ± 0.13	0.72 ± 0.41	0.06
$N_{g,RS}$	57.6 ± 3.8	0.83 ± 0.13	-0.42 ± 0.37	0.08
$f_{*,mean}$	0.85 ± 0.01	-0.03 ± 0.08	0.33 ± 0.35	0.00

Note – This table summarizes our main results for the full and RS population: It shows the best fit power law behavior with mass and redshift trends, as well as the normalization of the relation and the intrinsic scatter σ_{int}. We summarize the results for the characteristic magnitude Δm^* (Δm^*_{RS} for RS) as a difference to our passive evolution model, the characteristic galaxy density $\phi^* E^{-2}$, which is evolution corrected and the faint end slope α. Additionally we show the best fit relation on the derived quantities, that is the Halo Occupation Number as N_g and the stellar mass fraction $f_{*,mean}$. These results are based on individual cluster fits.

Faint End Slope α

To study the faint end slope in individual clusters we carry out two parameter LF fits. Given the fact that we see no redshift evolution in the magnitude difference between the data and the passive evolution model, we can use the characteristic magnitudes from the model m^*_{mod} to explore the evolution of the faint end slope. We use a gaussian prior on m^* from the composite LFs. As for all the previous analyses, we adopt a faint end magnitude limit of $m^* + 2$ ($m^* + 1.2$ for the highest redshift clusters) so that we are extracting α from the same portion of the LF over the full redshift range.

Figure 3.8 shows the individual clusters (black dots) with their best fitting α values as a function of redshift. Results from the 3 parameter fits to the composite LF in each redshift bin are again shown as blue squares, which are in agreement with the individual clusters.

We fit the individual cluster αs to the power law relation in mass and redshift (Equation 2.10). Table 3.2 contains the best fit parameters. The faint end slope in the full population has a characteristic value of $\alpha = -1.19 \pm 0.06$ at the pivot redshift $z_{piv} = 0.46$ and it evolves with redshift as $\alpha \propto (1+z)^{(-0.34 \pm 0.29)}$. There is a weak 1σ significant tendency for $z = 1$ clusters to have flatter luminosity functions and therefore fewer faint galaxies with respect to the bright end than in their low redshift counterparts. For the RS population we measure $\alpha_{red} = -0.61 \pm 0.06$ at the pivot redshift and an evolution of the faint end with redshift of $\alpha_{red} \propto (1+z)^{(-0.54 \pm 0.58)}$. Thus, the RS galaxy LF typically has a flatter faint

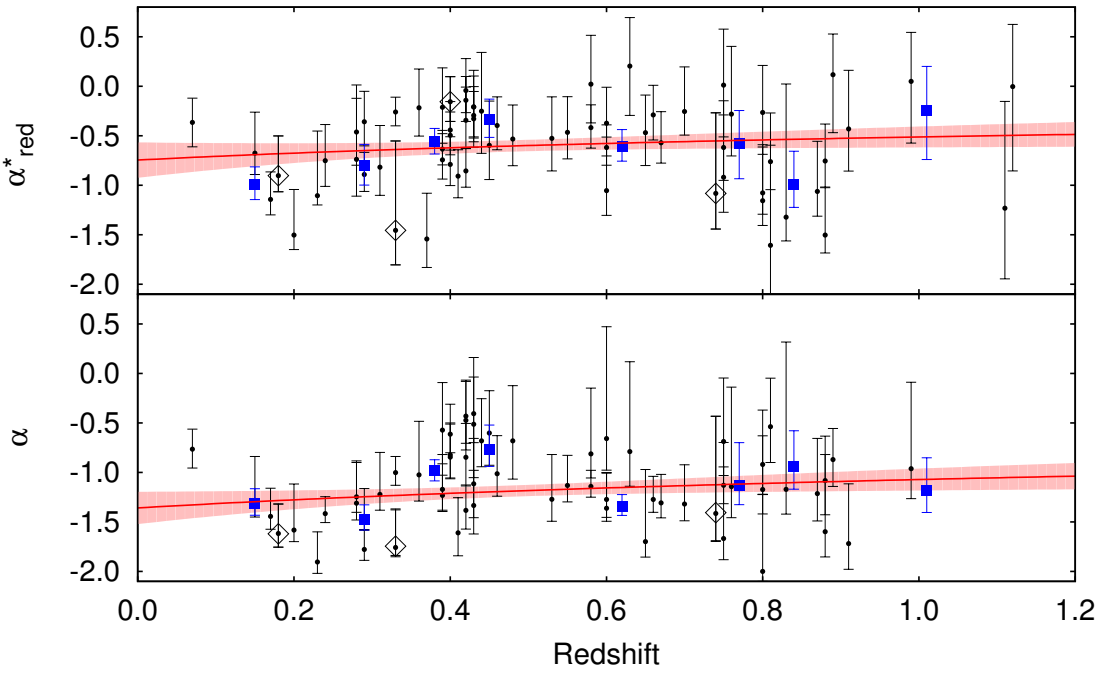

Figure 3.8 Evolution of the faint end slope α when keeping m^* fixed to the CSP passive evolution model (Section 2.3.1) for the full (bottom) and RS (top) galaxy populations. The color coding of the data is the same as Figure 3.7. The best fit power law (Table 3.2) and 1σ uncertainty (Equation 2.11) are in red.

end, as expected, but its redshift evolution is unconstrained. There is again no strong mass dependence in either sample. We note here that the evolutionary trend with redshift is not due to incompleteness at the faint end for the high redshift clusters, because all individual LFs are completeness corrected as described in Section 2.2.3. Also, we are studying the band redward of the rest frame 4000 Å break in all but the very highest redshift clusters in our sample, making this a robust experiment for extracting LF evolution.

Our result is in 1σ agreement with previously published results on individual clusters and samples at low redshift. For example we find agreement with the Jenkins et al. (2007) study on the Coma cluster at $z = 0.023$ with $\alpha = -1.25 \pm 0.05$. The analysis on the Norma cluster from Skelton et al. (2009) provides a faint end slope of $\alpha = -1.26 \pm 0.1$. Using the optical V-band for the Centaurus cluster, Chiboucas & Mateo (2006) measure a faint end slope $\alpha = -1.4^{+0.1}_{-0.18}$, which is still within the 2σ error bars of our result.

On the high redshift end we find agreement with a study of composite LFs of 7 clusters each in the $3.6\mu m$ and $4.5\mu m$ NIR bands from Mancone & Gonzalez (2012) with $\alpha = -0.97 \pm 0.14$ and $\alpha = -0.91 \pm 0.28$. These summarized literature studies are in favor of a redshift evolution in α, although the results have such large uncertainties that they do not require evolution. In contrast to the non-evolution there are various literature results over recent

years who have found evidence for a decreasing faint end slope with increasing redshift in the RS population (e.g. Gilbank et al. 2008; Stott et al. 2007; Tanaka et al. 2007; Rudnick et al. 2009), which we are not able to constrain within our errors.

One possible explanation for evolution in the faint end slope would be due to ongoing infall from surrounding field galaxies into the cluster. This effect strongly depends on the faint end slope of the field LF. Contrary to the findings of Mancone & Gonzalez (2012), a recent study of van der Burg et al. (2013a) shows that the field stellar mass function has a best fit faint end slope of -1.01 compared to the cluster environment with a faint end slope of -0.46.

3.3 Derived Properties

The LF parameter measurements in the previous section allow for additional quantities of interest to be studied. In the sections below we present an analysis of the halo occupation number (HON) and the stellar mass fraction.

3.3.1 Halo Occupation Number

In contrast to Section 2.4.3 here we calculate the HON by integrating the LF to $m^* + 2$ using the best fit α from the composite LF and the best fit values for m^* and ϕ^* from the individual LF fits. The HON is given as:

$$N_g = 1 + V_{200}\phi^* \int_{y_{low}}^{\infty} y^{\alpha} e^{-y} dy \tag{3.3}$$

Here the 1 comes from the fact that we excluded the BCG in our individual LFs. V_{200} is the cluster virial volume and $y_{low} = L_{low}/L*$.

We obtain errorbars on the HON by propagating the uncertainties in ϕ^* and m^* through the integration of the LF. Figure 3.9 is a plot of the measured HON for each cluster versus mass (left) and redshift (right) for the full population (bottom) and RS population (top). The best fit power law parameters (Equation 2.10) describing these data appear in Table 3.2. The characteristic HON at our pivot redshift $z_{piv} = 0.46$ and mass $M_{piv} = 6 \times 10^{14}\, M_{\odot}$ is 83.8 ± 6.0 for the full population and 57.6 ± 3.8 for the RS population. This is an indication that the red fraction at the pivot mass and redshift to $m^* + 2$ is 69%.

The mass trend for the full population is $N_g \propto M^{(0.97\pm0.13)}$ and for the RS population we find $N_{g,red} \propto M^{(0.83\pm0.13)}$. The full population shows basically self-similar evolution within the error bars. Yet the RS population seems to be more affected by galaxy formation efficiency with a $\mu < 1$. The full population shows evidence of $1.8\,\sigma$ to increase with redshift. In contrast to that the RS population exhibits a $1.1\,\sigma$ preference to fall with redshift $N_{g,red} \propto (1+z)^{(-0.42\pm0.37)}$.

Comparing to the derived constraints in Section 2.4.3 we find higher normalizations and steeper mass slopes from the LF parameters, yet all results hint towards a $\mu < 1$. Concerning the redshift evolution, we find agreement for the RS population for the trend of decreasing HON with redshift. Yet the trend for the full population is opposite between the constraints

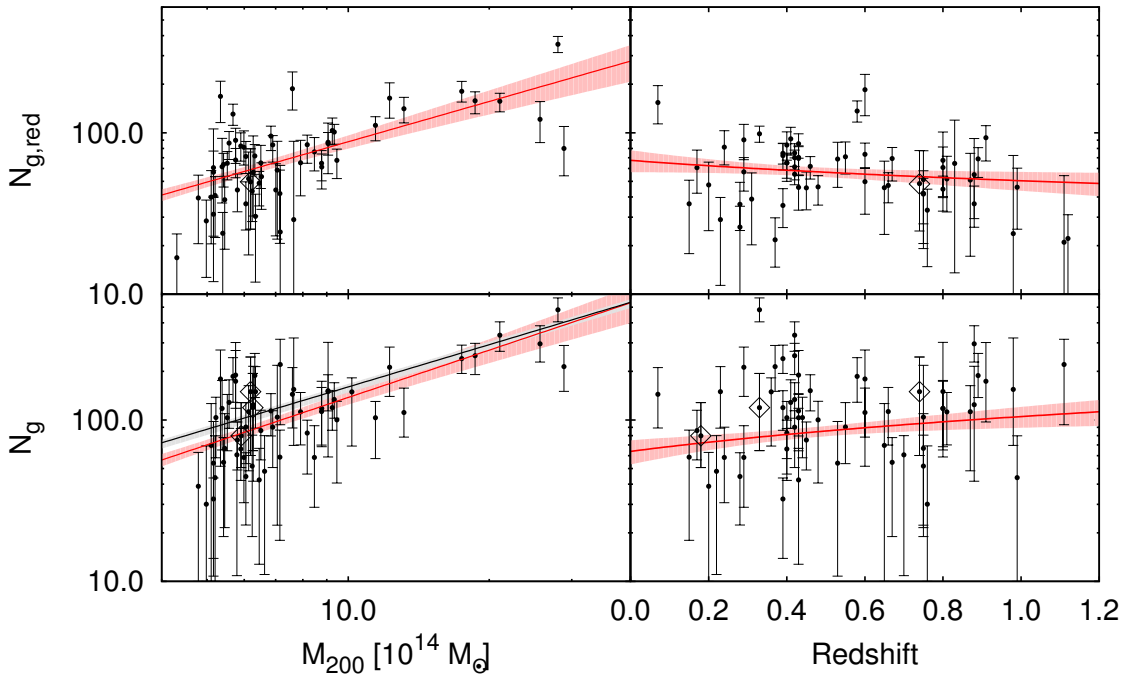

Figure 3.9 The HON integrated to $m^* + 2$ is plotted versus mass (left panels), and the HON normalized to a mass of $6 \times 10^{14} M_\odot$ is plotted versus redshift (right panels). In both cases the full (RS) population appears on bottom (top), and both populations have $N_g \propto M^\mu$ where $\mu < 1$ (fit parameters in Table 3.2). We find evidence of redshift evolution in the full and RS population. The 1σ region (Equation 2.11) for each fit is plotted in red. The black line in the lower left panel shows the behavior of clusters in the nearby universe (Lin et al. 2004). The LMC clusters with $\delta < -63°$ that are highly contaminated by stars are marked with black open diamonds.

from the RP and LF. A reason for non-evolution of the HON is given in Lin et al. (2006) and summarized here again: Looking at the evolution of the HON with mass and redshift we have:

$$HON(M, z) = V\phi^*\Gamma(\alpha + 1, L(z)/L^*(z)) \tag{3.4}$$

Here Γ is the incomplete Gamma function and $L(z)$ is the lower limit of the integration. As it is set to be a fixed value in terms of $L^*(z)$, the HON is mainly given by the product of the cluster virial volume V and the characteristic galaxy density ϕ^*. Given two galaxy clusters with the same mass but at different redshifts, the virial volume of the higher redshifted cluster is smaller than the one at the lower redshift. One thus expects that ϕ^* is increasing as a function of redshift. This behaviour is indeed seen from looking at the composite LFs in Figure 3.2 and Figure 3.3. If there is no evolution in the HON, then the decrease in the virial volume would compensate the increase in ϕ^*. Yet we already have seen in Section 3.2.3 that the redshift evolution corrected galaxy density $\phi^* E^{-2}$ is showing an increase with redshift. This reduction of the number density of massive galaxies over cosmic time, together with the

decrease of the HON with cosmic time could well be the product of the growth of the giant central galaxies through merging.

Yet we note that the LF parameters show a strong degeneracy, whereas we are able to reduce the parameter degeneracy in the RP analysis. Thus the HON from the RP analysis is tighter constrained and more reliable. Nevertheless both approaches give similar red fractions at the pivot redshift with $\sim 63\%$ and $\sim 69\%$ and show a mass dependency with $\mu < 1$. The LF HON constraints might hint towards a stronger decrease in the red fraction than the constraints from the RP analysis. We note that an extension of the sample will shed further light on this issue and we will gain in statistical significance to falsify or verify the redshift evolutionary trend.

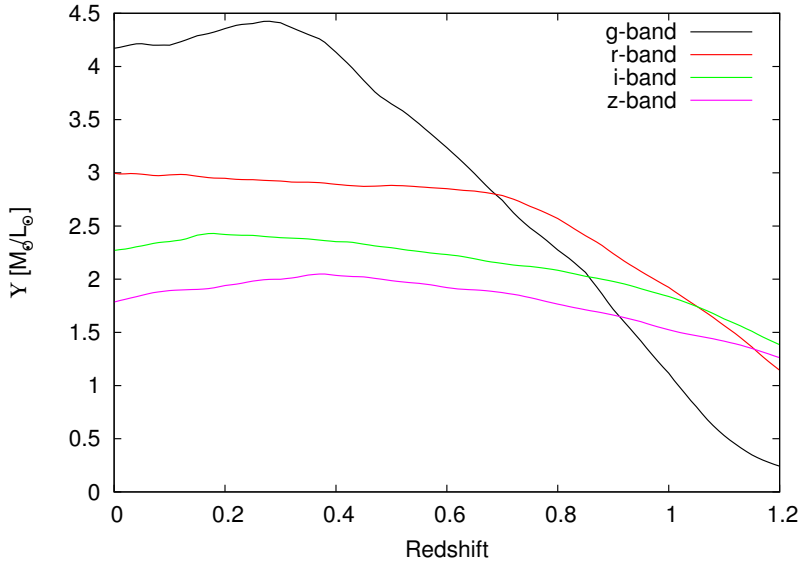

Figure 3.10 The redshift evolution of the mass-to-light ratio for the CSP model described in Section 2.3.1. The bands *griz* are color coded. We see a decrease in the mass to light ratio with increasing redshift, as expected in a passively evolving stellar population.

3.3.2 Stellar Mass Fraction

Here we present estimates of the total stellar masses of our clusters using the observed LFs together with mean mass to light information from our passive evolution model. Key results from the analysis presented in previous sections demonstrate that this model is consistent with the RS cluster galaxies and also the full population. These results include: (1) the good quality cluster photometric redshift measurements (Section 2.3.1), (2) our study of the color-magnitude distribution of cluster galaxies (Section 2.4.1) and (3) measurements of the evolution of m^* (Section 3.2.3) for both the RS and the full populations. All three results indicate that the RS galaxy population in SPT selected clusters is consistent with our passive evolution model (Section 2.3.1) over the redshift range $0 < z < 1.1$. In addition, the

consistency of the evolution of m^* for the full population with our CSP model shows that the full ensemble of galaxies also follows the gradual dimming expected in a passively evolving population. Thus, we can use the predicted, band-dependent stellar mass to light ratios in our model together with the integrated luminosity from our measured galaxy populations to constrain the stellar mass content.

As described previously (see Section 2.3.1), our passive evolution model is a combination of 6 different CSP models with different metallicities, tuned to reproduce the observed tilt of the RS. Thus, for our models, the mass to light ratio Υ in each band j varies not only with redshift z but also with the magnitude m of the galaxies $\Upsilon_j(m, z)$.

Moreover, there are both non-RS and RS galaxies present in our clusters, and our passive evolution model is most appropriate for the passive RS galaxies. The non-RS population is likely much more varied and in general will have lower mass to light ratios, given the ongoing star formation evidenced by the young stars and blue light coming from those systems. Rather than trying to predict an accurate mass to light ratio for the blue population, we use only the fact that the blue population must have a lower mass to light ratio than the RS population.

Within this context we can produce both upper and lower limits to the stellar mass in each cluster. Namely, we can measure the lower limit $M_{*,lo}$ by simply estimating the stellar mass in the RS population using the mass to light from our passive evolution models. Similarly, we can measure an upper limit on the stellar mass $M_{*,hi}$ by taking the luminosity of the total population and using the mass to light ratio of the RS population. The true stellar mass M_* will lie between these two limits: $M_{*,lo} < M_* < M_{*,hi}$. While this is not as precise as using many photometric bands to constrain the SED of each galaxy, it is a robust procedure that we can apply to a *griz* survey over the broad redshift range of our cluster sample.

For cluster i at redshift z_i whose LF $\phi_j(m)$ we have measured in band j (the band that lies redward of the rest frame 4000 Å break), we calculate the stellar mass lower limit $M_{*,lo}$ as

$$M^i_{*,lo} = M_{*,BCG} + V_{200} \int_{-\infty}^{m^*_i+2} \mathrm{d}m\, \phi^i_{j,RS}(m) L_j(m) \Upsilon_j(m, z_i) \tag{3.5}$$

where $M_{*,BCG}$ is the mass of the BCG, $\phi_{j,red}$ is the RS population LF for the cluster, $L_j(m)$ is the luminosity corresponding to magnitude m, and $\Upsilon_j(m, z_i)$ is the magnitude dependent mass to light ratio from the passive evolution model at the redshift of the cluster. Note that this integral is carried out to $m^* + 2$, the range over which we have measured the luminosity function (as noted earlier, we measure out to $m^* + 1.2$ in the highest redshift bin), and so it is does not represent the full stellar mass.

Similarly, we can write for the stellar mass upper limit $M_{*,hi}$

$$M^i_{*,hi} = M_{*,BCG} + V_{200} \int_{-\infty}^{m^*_i+2} \mathrm{d}m\, \phi^i_j(m) L_j(m) \Upsilon_j(m, z_i) \tag{3.6}$$

where ϕ_j is the LF of the full population, and the other terms and factors are the same as in Equation 3.5.

For the passive evolution model that describes our data, the tilt in the RS introduces only a slight variation in the mass to light ratio $\Upsilon(m)$, and therefore we adopt for our estimates here the value appropriate at $m = m^*$.

Figure 3.10 contains a plot of the mass to light ratios $\Upsilon_j(z)$ for band j of an m^* galaxy as a function of redshift in each band *griz*. We see a decrease in the mass to light ratio with increasing redshift, as expected in a passively evolving stellar population. The magnitude dependence of the mass to light ratio has only a small impact on estimates of the stellar masses.

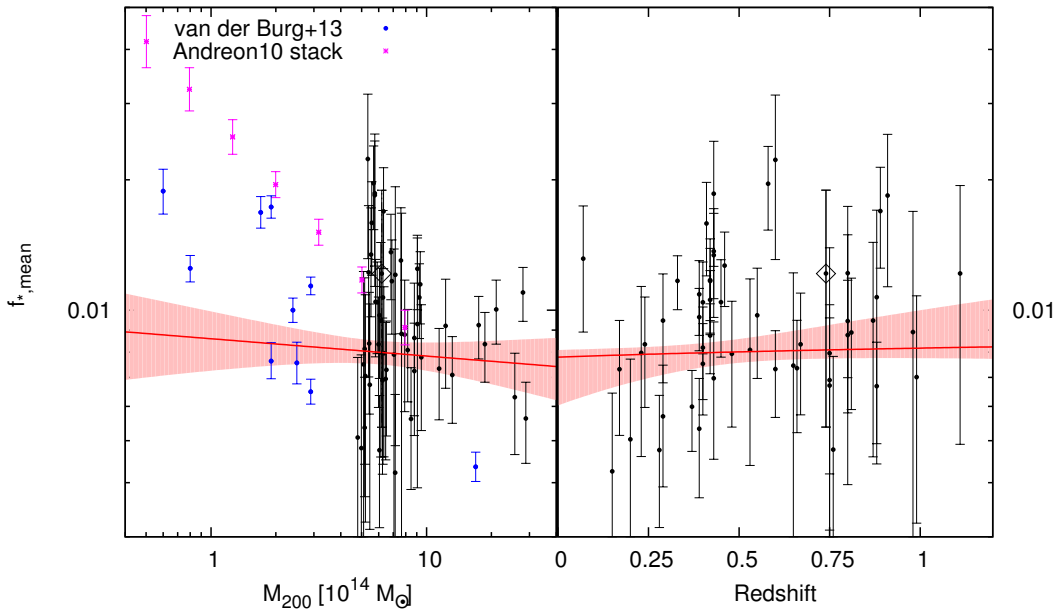

Figure 3.11 Stellar mass fraction within the virial radius R_{200} as a function of mass (left) and redshift (right). For each cluster we estimate a lower limit (from RS population) and an upper limit (from full population), and the black points represent the average of these values. The red band marks the 1σ region around the best fit on the mean stellar mass.. The typical stellar mass fraction for our clusters is $\sim$0.85%. The pink points are from a lower redshift study by Andreon (2010), and the blue points are from a high redshift study by van der Burg et al. (2014b).

We plot the fraction of the halo mass that is included in stars versus the cluster virial mass (left) and redshift (right) in Figure 3.11. The black points show the mean of the upper and lower limit on the stellar mass from the full and RS population. In addition, we show stacked results from Andreon (2010) using a sample of 52 clusters with SDSS data and caustic mass measurements with pink stars. In blue we add results from van der Burg et al. (2013a) using 10 individual clusters at $z \sim 1$.

We fit power law relations (Equation 2.10) to the upper $f_{*,hi}$ and low $f_{*,lo}$ limits to the stellar mass fraction. At the pivot mass and redshift of our sample, stellar mass fraction lies between the limits 0.71% and 0.95%. There is evidence for the upper limit stellar mass to

evolve positively with redshift $f_{*,hi} \propto (1+z)^{(0.70\pm0.45)}$, whereas the lower limit shows not such evolution $f_{*,lo} \propto (1+z)^{(-0.16\pm0.38)}$, because as noted in the previous section the red fraction seems to be falling with redshift. The upper limit shows a positive mass trend with $f_{*,hi} \propto M^{0.18\pm0.09}$, whereas the lower limit falls with $f_{*,lo} \propto M^{-0.16\pm0.15}$. The mean stellar mass fraction shows a typical value of 0.85%, is constant with redshift $f_{*,mean} \propto (1+z)^{(0.33\pm0.35)}$ and shows no significant mass trend with $f_{*,mean} \propto M^{-0.03\pm0.08}$.

Other observational results provide contradictory constraints on the variation of stellar mass fraction with halo mass: Lin et al. (2004) estimate the stellar mass fraction to be $f_* \sim M_{500}^{-0.26\pm0.09}$ for a sample of X-ray selected clusters. Andreon (2010) find $f_* \sim M_{200}^{-0.55\pm0.08}$ on a sample of 52 clusters and groups with precise mass measurements from the caustic technique. Recently Leauthaud et al. (2012) examined an X-ray selected sample of groups and clusters with a wide mass range. Based on a statistical Halo Occupation distribution model they derived the stellar mass function and used a simple M/L ratio conversion. They find only a weak dependence on mass and a much lower amplitude than previous studies. There are various cosmological simulations which predict that within R_{500} the total baryon fraction is supposed to be close to the universal baryon fraction (e.g. Kravtsov et al. 2005; Ettori et al. 2006). If the gas mass fractions are found to be lower in groups compared to clusters, then therefore the stellar mass fraction f^* is supposed to increase with decreasing halo mass in order to compensate for f_{gas}. Otherwise, if the stellar mass fraction does not rise significantly with decreasing mass, then groups are deficient in their baryon content compared to clusters and the universal mean (Budzynski et al. 2014). Reasons for these differences in the scaling relation might be due to different selection techniques, different virial mass estimates, different assumptions in deriving the stellar Mass-to-Light ratio (i.e. differences in the initial mass function), and the lack of the contribution from the diffuse intracluster light (Budzynski et al. 2014). Leauthaud et al. (2012) emphasize that differences in stellar mass estimates can be reduced by changing the IMF. Furthermore they note that a single M/L conversion factor used for all galaxies will introduce a bias in f^*, since not all galaxies in groups and clusters are quiescent and the fraction of quenched galaxies is supposed to change with the halo mass. Our result is most consistent with a study of 20,171 groups and clusters from Budzynski et al. (2014) over a wide mass range and at $0.15 < z < 0.4$. By stacking groups and clusters in mass bins they have a strong constraint on the variation of the stellar mass fraction with mass. They find a weak trend of $f^* \sim M_{500}^{-0.11\pm0.14}$ and on stacked images they get $f^* \sim M_{500}^{0.05\pm0.05}$. Yet their typical stellar mass fraction is higher with 1.3%, which can be partly explained by the ICL contribution between 20-40%. The weak mass dependence of f^* is supported by various cosmological simulations and semi-analytic models (e.g. Puchwein et al. 2010; Planelles et al. 2013). A steep decrease in f^* with virial mass raises questions, because within the standard hierarchical structure formation paradigm clusters form from the accretion of groups. In particular, our result is consistent with hierarchical structure formation models with $B > -0.35$ from Balogh et al. (2008) and ab-initio galaxy formation models with $B > -0.1$ from (Bower et al. 2006; Balogh et al. 2008).

3.4 Discussion and Conclusions

We study the luminosity functions of the SZE selected clusters, also probing for mass and redshift variation of the characteristic magnitude m^*, the characteristic density ϕ^*, and the faint end slope α. In these analyses we always use the photometric band that lies redward of the 4000 Å break so that we are less affected by any possible recent star formation and so that we are sensitive to the same portion of the rest frame galaxy SEDs. We first examine stacks of cluster LFs in 8 different redshift bins.

We use these stacked LFs to determine the characteristic faint end slopes α within each redshift range. These α's allow us to better constrain the evolution in m^* and ϕ^* on a single cluster basis. All trends are reported in Table 3.2; below we list the main results. Note that using the parameter m^* to constrain the other 2 does not affect our conclusions.

We find that the characteristic magnitudes of the LFs for both the full and RS populations evolve in good agreement with our passive evolution CSP model out to redshift ~ 1.1. This is consistent with a variety of literature studies that have found that cluster galaxies are well fit by passive evolution models (see, e.g., Stanford et al. 1998; Lin et al. 2006; Capozzi et al. 2012), but it is interesting to see this behavior in a uniformly selected sample extending over such a large redshift range. Figure 3.6 shows the redshift evolution of m^* for the $griz$ bands in our passive evolution model. We test for different formation epochs of the initial starburst in our model and find that a formation epoch of $z_f = 3 - 5$ is preferred.

Because we have robust mass estimates for these clusters (Bocquet et al. 2014) we can examine the characteristic density of the galaxies with $m \sim m^*$ within physical units of $Mpc^{-3}\ mag^{-1}$. We study $\phi^*/E^2(z)$ as a function of mass and redshift, because we have defined the virial region to be that region that encloses a density that is 200 times the critical density, which evolves as $\rho_{crit} \propto E^2(z)$ (see Section 3.2.3). Our data support variation of the bright galaxy population density with redshift (at $\sim 1.5\sigma$) for the full population, which increases as $\phi^*/E(z)^2 \propto (1+z)^{0.70\pm0.46}$, but weaker evidence in the RS population, which decreases as $\phi^*_{red}/E(z)^2 \propto (1+z)^{-0.33\pm0.41}$. Together, these trends suggest that there is a reduction of the number density of luminous $m \sim m^*$ galaxies over time coupled with a transformation of the blue members of this population into RS galaxies. This reduction of the number density of massive galaxies over cosmic time, together with the tendency for the concentration of the galaxy distribution to fall over time, could well be the product of the growth of the giant central galaxies through merging.

We examine the redshift evolution of the faint end slope α using LF fits to the individual clusters. We find $\alpha \propto (1+z)^{-0.34\pm0.29}$ using the full population and $\alpha \propto (1+z)^{-0.54\pm0.58}$ using the RS population. Thus, our data provide only weak indication that the faint end of the LF is less populated in high redshift clusters than in their low redshift counterparts. Moreover, our data prefer steeper faint end slopes for the full population (characteristic value of $\alpha = -1.19 \pm 0.06$ at pivot mass $M_{piv} = 6 \times 10^{14} M_\odot$ and redshift $z_{piv} = 0.46$) than for the RS population (characteristic value of $\alpha = -0.61 \pm 0.06$). This preference is clearly apparent in the stacked LFs in Figure 3.2 and Figure 3.3.

We examine the evolution of the HON to $m^* + 2$ with mass and redshift. Our result for the mass trend $N_g \propto M^{0.97\pm0.13}$ is somewhat steeper than previous results from the low redshift cluster population (Lin et al. 2004; Rines et al. 2004), and indicates that there is in

general self similar evolution. Moreover, we examine the redshift trend of the HON at fixed mass, finding a 1.8σ significant hint for the HON to decrease with cosmic time in the full population $N_g \propto (1+z)^{0.72\pm0.41}$. The reduction of galaxy number with cosmic time could also be explained through the growth of the massive central galaxies. The decrease of the RS population $N_{g,red} \propto (1+z)^{-0.42\pm0.37}$ hints towards an increase in the red fraction over cosmic time.

Finally, given the good agreement between our high redshift burst CSP model and our cluster sample, we have used the mass to light ratios Υ of this model together with the luminosity measured from our cluster populations to estimate the total stellar mass within the virial region for each of our clusters. We present a lower limit $f_{*,lo}$ to the stellar mass fraction by applying the mass to light ratio Υ to the RS population, and an upper limit $f_{*,hi}$ by applying it to the full population. We examine trends in these quantities as well as their mean as a function of mass and redshift. Our data provide no clear evidence of a redshift trend within the mass range we probe, with $f_{*,mean} \propto (1+z)^{0.33\pm0.35}$. The characteristic value of the stellar mass fraction to m^*+2 is $f_{*,mean} = 0.85\pm0.01\%$. Consistent with the work from Budzynski et al. (2014), we find no evidence for a mass trend with $f_{*,mean} \propto M^{-0.03\pm0.08}$. Our typical stellar mass fraction evolution is similar with a recent analysis of 14 massive clusters at a median redshift $z = 0.9$ (Chiu et al. 2014), demonstrating again that no strong redshift and mass trend is present.

The falling f_* with mass (observed in various literature studies (e.g. Lin et al. 2003)) and its approximate constancy with cosmic time (shown here on high mass cluster scales), poses challenges to a simple hierarchical structure formation model where massive clusters form solely from the accretion of groups. From a theoretical perspective, the buildup of clusters out of lower mass clusters and groups should lead to weak mass trends in f_* with mass unless there are dramatic redshift trends in f_* (e.g. Balogh et al. 2008). As emphasized in Chiu et al. (2014), it appears that significant infall directly from the field, where f_* is lower than that in massive clusters at $z \sim 1$ and comparable at $z = 0$ (Lin et al. 2003; van der Burg et al. 2013b) is required to reproduce the observed mass and redshift trends. Indeed, McGee et al. (2009) have examined formation on cluster mass scales and shown that only $\sim$40% of the galaxies in massive clusters have previous been members of lower mass clusters or groups. In this study we have shown that blue galaxies (at all luminosities) are found preferentially at the outskirts of the cluster virial region R_{200} and avoiding the cluster core, which is strongly suggestive of direct infall from the field (Section 3.2.2). Further theoretical galaxy formation studies that focus on trends in the properties of cluster galaxies as a function of mass and redshift are needed to demonstrate a precise match to the results presented here. Such studies will shed further light on the physical processes responsible for the transformation of infalling field galaxies into RS galaxies.

In summary, we have used a large, homogeneously selected sample of clusters with $M_{200} > 4 \times 10^{14} M_\odot$ extending to $z \sim 1.1$ to carry out a study of the mass and redshift dependencies of the galaxy population within the cluster virial region. Our results reveal that the characteristics of the cluster galaxy populations change since $z = 1$. We find generally good agreement with previous studies, but owing to the redshift range and sample size we are able to present more precise measurements of the population evolution. A scenario emerges where infall from the field over the full redshift range provides a supply of non-RS

galaxies at all luminosities. These cluster galaxies are then transformed into RS galaxies through initial quenching (perhaps ram pressure stripping– see Muzzin et al. 2014) followed by a natural dying away of the most luminous, massive young stars on a timescale of ∼2 to 3 Gyr. The concentration and the characteristic number density of $m \sim m^*$ galaxies in the full population falls over time, perhaps due to merging onto and growth of the giant central galaxies. This same process may explain why the HON exhibits a mass slope still shallower than unity. Our full set of observational results provides a resource for confronting specific galaxy formation simulations; matching the mass and redshift trends presented here should lead to significant improvements in our understanding of this process.

Overall, our study underscores the power of combining a large mm-wave survey from SPT that enables SZE cluster selection with the deep, multi band optical survey dataset from DES. The selection of the sample is homogeneous and does not directly depend on properties of the galaxy population. Moreover, each cluster has a high quality SZE mass proxy that has been calibrated to mass over the full redshift range (Bocquet et al. 2014). This, together with the deep and wide area DES data, allow us to study the galaxy populations present in the same portion of the virial region in massive galaxy clusters over the last ∼10 Gyr period in cosmic evolution. This initial examination of the galaxy populations within SPT selected clusters will benefit from expansion to the larger sample available today and from an increased focus on the transition of the population from the field to the cluster.

Table 3.3 Individual best fit parameters for the SPT Cluster sample

clustername	α α_{RS}	ϕ^* ϕ^*_{RS} $[Mpc^{-3}mag^{-1}]$	Δm^* Δm^*_{RS} [mag]	N_g $N_{g,RS}$ #	$f_{*,hi} * 100$ $f_{*,lo} * 100$ [%]
SPT-CLJ0001-5440	$-0.86^{+0.31}_{-0.27}$	$14.13^{+5.31}_{-3.82}$	$-0.43^{+0.38}_{-0.24}$	$188.5^{+70.0}_{-50.7}$	$1.26^{+0.46}_{-0.33}$
	$0.12^{+0.41}_{-0.59}$	$8.73^{+1.58}_{-2.06}$	$0.48^{+0.33}_{-0.27}$	$71.9^{+12.5}_{-16.7}$	$0.88^{+0.14}_{-0.19}$
SPT-CLJ0008-5318	$-0.59^{+0.49}_{-0.35}$	$1.68^{+0.63}_{-0.99}$	$-0.49^{+0.84}_{-0.73}$	$32.4^{+11.3}_{-18.5}$	$0.24^{+0.07}_{-0.12}$
	$-0.21^{+0.40}_{-0.36}$	$2.15^{+0.67}_{-0.60}$	$-0.13^{+0.46}_{-0.38}$	$31.3^{+8.5}_{-8.5}$	$0.31^{+0.07}_{-0.07}$
SPT-CLJ0012-5352	$-0.85^{+0.34}_{-0.22}$	$3.09^{+1.09}_{-1.14}$	$-0.21^{+0.59}_{-0.45}$	$66.1^{+22.4}_{-23.9}$	$0.46^{+0.15}_{-0.16}$
	$-0.79^{+0.28}_{-0.21}$	$5.16^{+1.15}_{-1.02}$	$0.57^{+0.29}_{-0.22}$	$82.8^{+17.1}_{-16.1}$	$0.77^{+0.15}_{-0.14}$
SPT-CLJ0036-4411	$-1.21^{+0.55}_{-0.28}$	$9.24^{+4.24}_{-5.32}$	$0.45^{+0.90}_{-0.75}$	$112.5^{+50.5}_{-64.2}$	$0.81^{+0.36}_{-0.45}$
	$-1.06^{+0.51}_{-0.25}$	$3.92^{+1.93}_{-2.65}$	$-0.13^{+1.16}_{-1.81}$	$51.9^{+24.0}_{-34.4}$	$0.35^{+0.16}_{-0.23}$
SPT-CLJ0040-4407	$-1.03^{+0.17}_{-0.14}$	$3.70^{+0.84}_{-0.71}$	$-0.01^{+0.27}_{-0.17}$	$239.5^{+51.2}_{-45.5}$	$1.61^{+0.33}_{-0.29}$
	$-0.63^{+0.19}_{-0.16}$	$3.74^{+0.57}_{-0.53}$	$0.36^{+0.20}_{-0.16}$	$180.7^{+27.3}_{-25.6}$	$1.62^{+0.23}_{-0.21}$
SPT-CLJ0041-4428	$-0.94^{+0.50}_{-0.24}$	$3.93^{+0.96}_{-2.13}$	$0.15^{+1.24}_{-2.74}$	$149.4^{+32.8}_{-80.5}$	$0.98^{+0.21}_{-0.53}$
	$-0.22^{+0.39}_{-0.29}$	–	–	–	–
SPT-CLJ0102-4915	$-0.85^{+0.35}_{-0.27}$	$6.47^{+1.96}_{-1.49}$	$0.23^{+0.40}_{-0.21}$	$296.4^{+87.1}_{-68.1}$	$2.29^{+0.66}_{-0.52}$
	$-0.75^{+0.37}_{-0.26}$	$2.60^{+0.85}_{-0.74}$	$0.05^{+0.39}_{-0.28}$	$121.1^{+34.9}_{-34.3}$	$0.94^{+0.26}_{-0.26}$
SPT-CLJ0107-4855	$-1.39^{+0.37}_{-0.14}$	$8.52^{+4.43}_{-6.11}$	$-0.57^{+1.48}_{-0.82}$	$179.5^{+92.0}_{-127.9}$	$0.96^{+0.49}_{-0.68}$
	$-1.05^{+0.54}_{-0.25}$	$14.33^{+3.55}_{-4.49}$	$1.26^{+0.75}_{-1.37}$	$167.9^{+40.9}_{-52.3}$	$1.43^{+0.35}_{-0.44}$
SPT-CLJ0330-5228	–	–	–	–	–
	–	–	–	–	–
SPT-CLJ0412-5106	$-1.25^{+0.35}_{-0.15}$	$1.19^{+0.57}_{-0.61}$	$-0.84^{+0.62}_{-0.47}$	$44.6^{+18.1}_{-22.3}$	$0.24^{+0.09}_{-0.11}$
	$-0.46^{+0.48}_{-0.33}$	$1.72^{+0.68}_{-0.55}$	$0.28^{+0.51}_{-0.31}$	$36.3^{+13.3}_{-11.3}$	$0.33^{+0.10}_{-0.09}$
SPT-CLJ0417-4748	$-1.12^{+0.24}_{-0.16}$	$2.23^{+0.95}_{-0.67}$	$-0.66^{+0.47}_{-0.27}$	$111.2^{+46.2}_{-32.9}$	$0.64^{+0.25}_{-0.18}$
	$-0.62^{+0.23}_{-0.18}$	$4.71^{+0.84}_{-0.87}$	$0.31^{+0.23}_{-0.18}$	$140.8^{+24.8}_{-25.7}$	$1.23^{+0.20}_{-0.21}$
SPT-CLJ0422-4608	$-1.33^{+0.29}_{-0.15}$	$2.74^{+1.22}_{-1.82}$	$-1.00^{+0.98}_{-0.81}$	$54.6^{+23.1}_{-35.7}$	$0.30^{+0.12}_{-0.19}$
	$-0.57^{+0.31}_{-0.21}$	$5.94^{+1.13}_{-1.66}$	$0.41^{+0.31}_{-0.28}$	$63.6^{+11.0}_{-17.5}$	$0.61^{+0.10}_{-0.15}$
SPT-CLJ0422-5140	$-0.65^{+1.11}_{-0.32}$	–	–	–	–
	$-0.37^{+0.36}_{-0.33}$	$3.81^{+0.88}_{-1.45}$	$0.48^{+0.55}_{-0.73}$	$53.4^{+11.7}_{-19.9}$	$0.48^{+0.10}_{-0.17}$
SPT-CLJ0423-6143	$-0.81^{+0.93}_{-0.36}$	–	–	–	–
	$0.20^{+0.49}_{-0.50}$	–	–	–	–
SPT-CLJ0426-5416	–	–	–	–	–
	–	–	–	–	–
SPT-CLJ0426-5455	$-1.19^{+0.22}_{-0.12}$	$3.64^{+1.54}_{-1.39}$	$-0.79^{+0.56}_{-0.40}$	$112.7^{+46.2}_{-42.8}$	$0.64^{+0.25}_{-0.24}$
	$-0.29^{+0.30}_{-0.25}$	$3.76^{+0.79}_{-0.85}$	$0.26^{+0.27}_{-0.24}$	$64.7^{+12.8}_{-14.3}$	$0.63^{+0.12}_{-0.13}$
SPT-CLJ0428-6049	$-1.15^{+0.44}_{-0.19}$	$4.19^{+2.82}_{-2.88}$	$-0.93^{+0.97}_{-0.52}$	$66.7^{+42.6}_{-45.2}$	$0.41^{+0.25}_{-0.26}$
	$-0.62^{+0.47}_{-0.33}$	$3.45^{+1.48}_{-1.80}$	$-0.39^{+0.78}_{-0.63}$	$38.5^{+15.2}_{-19.5}$	$0.33^{+0.12}_{-0.15}$
SPT-CLJ0429-5233	$-1.30^{+0.46}_{-0.23}$	$2.43^{+2.06}_{-1.98}$	$-0.35^{+1.30}_{-0.80}$	$53.9^{+43.9}_{-43.2}$	$0.30^{+0.23}_{-0.23}$
	$-0.53^{+0.42}_{-0.33}$	$4.91^{+1.40}_{-1.66}$	$0.74^{+0.46}_{-0.45}$	$60.7^{+16.3}_{-20.2}$	$0.54^{+0.14}_{-0.17}$
SPT-CLJ0430-6251	$-1.89^{+0.30}_{-0.11}$	$4.04^{+1.84}_{-1.65}$	$0.47^{+0.55}_{-0.34}$	$149.5^{+64.5}_{-60.4}$	$0.81^{+0.34}_{-0.32}$
	$-1.11^{+0.65}_{-0.09}$	$1.08^{+0.48}_{-0.68}$	$-0.26^{+1.27}_{-1.88}$	$30.3^{+11.3}_{-18.5}$	$0.20^{+0.07}_{-0.12}$

Table 3.4 Individual best fit parameters for the SPT Cluster sample continued

clustername	α α_{RS}	ϕ^* ϕ^*_{RS} $[Mpc^{-3}mag^{-1}]$	Δm^* Δm^*_{RS} [mag]	N_g $N_{g,RS}$ #	$f_{*,hi} * 100$ $f_{*,lo} * 100$ [%]
SPT-CLJ0431-6126	$-0.73^{+0.19}_{-0.18}$	$2.83^{+1.37}_{-1.09}$	$-0.84^{+0.60}_{-0.35}$	$144.2^{+66.6}_{-55.0}$	$0.77^{+0.35}_{-0.29}$
	$-0.36^{+0.25}_{-0.25}$	$4.85^{+1.32}_{-1.28}$	$0.07^{+0.35}_{-0.27}$	$187.3^{+50.8}_{-49.1}$	$1.21^{+0.32}_{-0.31}$
SPT-CLJ0432-6150	–	–	–	–	–
	$-0.00^{+0.63}_{-0.85}$	$3.85^{+1.70}_{-2.55}$	$0.42^{+0.88}_{-1.13}$	$16.8^{+6.8}_{-10.5}$	$0.25^{+0.08}_{-0.13}$
SPT-CLJ0433-5630	$-1.33^{+0.40}_{-0.17}$	$3.02^{+1.04}_{-2.52}$	$-0.78^{+1.37}_{-1.04}$	$60.7^{+19.2}_{-49.8}$	$0.33^{+0.10}_{-0.27}$
	$-0.25^{+0.45}_{-0.24}$	–	–	–	–
SPT-CLJ0437-5307	$-1.33^{+0.44}_{-0.17}$	–	–	–	–
	$-0.74^{+0.62}_{-0.37}$	$1.16^{+0.48}_{-0.78}$	$-0.14^{+1.07}_{-1.99}$	$23.8^{+8.3}_{-15.4}$	$0.18^{+0.06}_{-0.11}$
SPT-CLJ0438-5419	$-1.15^{+0.21}_{-0.16}$	$3.95^{+0.81}_{-0.94}$	$0.47^{+0.31}_{-0.25}$	$250.1^{+48.0}_{-59.3}$	$1.70^{+0.32}_{-0.40}$
	$-0.85^{+0.23}_{-0.16}$	$3.25^{+0.54}_{-0.55}$	$0.74^{+0.27}_{-0.24}$	$157.7^{+21.4}_{-26.7}$	$1.41^{+0.19}_{-0.23}$
SPT-CLJ0439-4600	$-1.09^{+0.33}_{-0.20}$	$3.61^{+1.08}_{-1.00}$	$0.39^{+0.38}_{-0.26}$	$119.1^{+32.6}_{-32.8}$	$0.90^{+0.22}_{-0.22}$
	$-0.74^{+0.27}_{-0.19}$	$4.19^{+0.84}_{-0.78}$	$0.76^{+0.25}_{-0.21}$	$103.3^{+20.0}_{-19.1}$	$1.07^{+0.18}_{-0.17}$
SPT-CLJ0439-5330	$-0.51^{+0.67}_{-0.53}$	$2.16^{+1.27}_{-1.55}$	$0.04^{+1.36}_{-0.91}$	$42.5^{+24.1}_{-29.7}$	$0.35^{+0.18}_{-0.22}$
	$-0.21^{+0.37}_{-0.35}$	$3.19^{+0.66}_{-0.91}$	$0.67^{+0.33}_{-0.32}$	$48.7^{+8.9}_{-13.5}$	$0.55^{+0.09}_{-0.14}$
SPT-CLJ0440-4657	$-0.58^{+0.29}_{-0.18}$	$2.92^{+0.65}_{-1.31}$	$-0.40^{+0.75}_{-1.06}$	$82.9^{+16.6}_{-36.7}$	$0.56^{+0.11}_{-0.25}$
	$-0.44^{+0.29}_{-0.20}$	$3.91^{+0.64}_{-0.92}$	$0.36^{+0.39}_{-0.41}$	$84.3^{+12.4}_{-19.5}$	$0.76^{+0.11}_{-0.17}$
SPT-CLJ0441-4855	$-0.86^{+0.52}_{-0.29}$	$6.19^{+2.99}_{-2.62}$	$-0.32^{+0.58}_{-0.40}$	$117.7^{+56.1}_{-49.4}$	$0.84^{+0.39}_{-0.34}$
	$-0.26^{+0.48}_{-0.42}$	$4.58^{+1.03}_{-1.25}$	$0.34^{+0.36}_{-0.29}$	$61.3^{+12.5}_{-16.5}$	$0.68^{+0.13}_{-0.17}$
SPT-CLJ0442-6138	–	–	–	–	–
	–	–	–	–	–
SPT-CLJ0444-4352	$-1.15^{+0.16}_{-0.11}$	$8.59^{+2.65}_{-2.67}$	$-0.56^{+0.35}_{-0.31}$	$186.3^{+56.7}_{-57.6}$	$1.04^{+0.31}_{-0.32}$
	$-0.42^{+0.23}_{-0.21}$	$10.54^{+1.65}_{-1.56}$	$0.56^{+0.22}_{-0.17}$	$130.4^{+20.1}_{-19.2}$	$1.19^{+0.18}_{-0.17}$
SPT-CLJ0444-5603	$-0.98^{+0.89}_{-0.31}$	$4.04^{+3.41}_{-3.63}$	$-0.73^{+1.82}_{-1.67}$	$43.9^{+35.8}_{-38.5}$	$0.28^{+0.22}_{-0.24}$
	$0.05^{+0.50}_{-0.62}$	$6.53^{+2.18}_{-3.02}$	$0.10^{+0.85}_{-1.48}$	$40.8^{+12.7}_{-18.4}$	$0.46^{+0.14}_{-0.20}$
SPT-CLJ0446-5849	–	$16.54^{+7.24}_{-9.58}$	$0.82^{+0.49}_{-0.41}$	$220.4^{+95.8}_{-127.1}$	$1.40^{+0.59}_{-0.78}$
	$-1.23^{+1.08}_{-0.71}$	$3.24^{+5.45}_{-2.94}$	$1.13^{+2.13}_{-1.10}$	$24.3^{+38.5}_{-21.1}$	$0.33^{+0.45}_{-0.24}$
SPT-CLJ0447-5055	$-0.46^{+0.40}_{-0.29}$	$4.37^{+1.24}_{-1.93}$	$0.21^{+0.66}_{-0.70}$	$90.2^{+23.8}_{-39.5}$	$0.70^{+0.18}_{-0.30}$
	$-0.34^{+0.34}_{-0.29}$	$5.23^{+0.84}_{-1.15}$	$0.99^{+0.27}_{-0.29}$	$84.1^{+11.9}_{-18.3}$	$0.91^{+0.12}_{-0.19}$
SPT-CLJ0449-4901	$-1.87^{+0.73}_{-0.15}$	$6.43^{+6.64}_{-3.93}$	$0.69^{+1.01}_{-0.15}$	$150.1^{+152.3}_{-91.2}$	$0.97^{+0.93}_{-0.56}$
	$-1.08^{+0.49}_{-0.22}$	$5.01^{+1.82}_{-1.77}$	$0.30^{+0.54}_{-0.39}$	$85.7^{+29.2}_{-30.0}$	$0.71^{+0.23}_{-0.24}$
SPT-CLJ0451-4952	$-1.63^{+0.36}_{-0.24}$	$6.47^{+2.52}_{-2.01}$	$0.72^{+0.46}_{-0.26}$	$128.3^{+48.9}_{-39.6}$	$0.93^{+0.32}_{-0.26}$
	$-0.91^{+0.27}_{-0.22}$	$5.87^{+1.08}_{-1.23}$	$0.71^{+0.26}_{-0.22}$	$86.2^{+15.5}_{-17.9}$	$0.84^{+0.13}_{-0.16}$
SPT-CLJ0452-4806	$-0.70^{+0.44}_{-0.27}$	$6.79^{+2.40}_{-2.99}$	$0.46^{+0.92}_{-1.48}$	$103.4^{+34.8}_{-45.1}$	$0.80^{+0.27}_{-0.34}$
	$-0.25^{+0.59}_{-0.43}$	–	–	–	–
SPT-CLJ0456-4906	$-1.59^{+0.77}_{-0.25}$	$9.89^{+7.31}_{-6.62}$	$0.75^{+0.96}_{-0.31}$	$124.3^{+90.8}_{-82.6}$	$0.96^{+0.62}_{-0.57}$
	$-1.50^{+0.48}_{-0.18}$	$3.70^{+2.61}_{-1.75}$	$-0.09^{+0.62}_{-0.31}$	$57.0^{+38.6}_{-26.5}$	$0.39^{+0.23}_{-0.16}$
SPT-CLJ0456-5623	$-1.75^{+0.75}_{-0.16}$	$3.74^{+3.18}_{-3.41}$	$0.59^{+1.20}_{-0.52}$	$69.5^{+56.8}_{-62.5}$	$0.40^{+0.31}_{-0.34}$
	$-0.47^{+0.38}_{-0.33}$	$3.81^{+1.85}_{-1.90}$	$0.32^{+0.86}_{-3.13}$	$39.9^{+18.4}_{-19.4}$	$0.36^{+0.16}_{-0.17}$

Table 3.5 Individual best fit parameters for the SPT Cluster sample continued

clustername	α α_{RS}	ϕ^* ϕ^*_{RS} $[Mpc^{-3}mag^{-1}]$	Δm^* Δm^*_{RS} [mag]	N_g $N_{g,RS}$ #	$f_{*,hi} * 100$ $f_{*,lo} * 100$ [%]
SPT-CLJ0456-6141	$-1.13^{+0.46}_{-0.35}$	$6.04^{+2.41}_{-2.29}$	$0.66^{+0.53}_{-0.31}$	$103.1^{+40.8}_{-38.7}$	$0.79^{+0.30}_{-0.28}$
	$-0.21^{+0.31}_{-0.30}$	$5.02^{+0.92}_{-1.08}$	$0.71^{+0.31}_{-0.26}$	$64.7^{+11.7}_{-13.7}$	$0.70^{+0.12}_{-0.14}$
SPT-CLJ0458-5741	$-1.64^{+0.48}_{-0.12}$	$1.32^{+0.88}_{-1.15}$	$-0.40^{+1.41}_{-0.76}$	$38.8^{+24.2}_{-33.1}$	$0.21^{+0.13}_{-0.17}$
	$-1.50^{+0.46}_{-0.15}$	$1.80^{+0.80}_{-0.89}$	$0.24^{+0.69}_{-0.58}$	$39.4^{+15.2}_{-18.9}$	$0.27^{+0.10}_{-0.12}$
SPT-CLJ0500-4551	$-1.42^{+0.17}_{-0.09}$	$1.35^{+0.78}_{-0.65}$	$-1.24^{+0.60}_{-0.35}$	$58.5^{+31.7}_{-27.8}$	$0.29^{+0.15}_{-0.13}$
	$-0.75^{+0.37}_{-0.26}$	$3.65^{+0.97}_{-0.83}$	$0.76^{+0.30}_{-0.20}$	$81.3^{+21.4}_{-18.2}$	$0.71^{+0.16}_{-0.13}$
SPT-CLJ0500-5116	$-1.25^{+0.43}_{-0.16}$	$1.35^{+0.65}_{-0.95}$	$-0.23^{+1.02}_{-0.84}$	$58.9^{+27.6}_{-40.9}$	$0.32^{+0.15}_{-0.22}$
	$-0.68^{+0.42}_{-0.22}$	$1.29^{+0.56}_{-0.67}$	$-0.46^{+1.06}_{-2.84}$	$42.0^{+16.8}_{-21.3}$	$0.28^{+0.11}_{-0.14}$
SPT-CLJ0502-6048	$-1.20^{+1.53}_{-0.26}$	–	–	–	–
	$-1.32^{+1.35}_{-0.24}$	$5.03^{+4.38}_{-4.04}$	$0.81^{+1.51}_{-1.64}$	$57.0^{+48.5}_{-45.0}$	$0.40^{+0.33}_{-0.31}$
SPT-CLJ0502-6113	$-1.19^{+0.55}_{-0.25}$	$9.73^{+4.91}_{-4.38}$	$0.33^{+0.70}_{-0.32}$	$117.8^{+57.8}_{-52.6}$	$0.85^{+0.39}_{-0.36}$
	$-1.16^{+0.54}_{-0.25}$	$5.01^{+2.58}_{-2.05}$	$0.32^{+0.60}_{-0.30}$	$61.6^{+30.8}_{-24.8}$	$0.47^{+0.21}_{-0.17}$
SPT-CLJ0504-4929	–	$1.23^{+0.89}_{-0.97}$	$-0.51^{+1.95}_{-1.68}$	$48.0^{+31.9}_{-37.0}$	$0.25^{+0.17}_{-0.20}$
	–	–	–	–	–
SPT-CLJ0505-6145	$-1.36^{+0.27}_{-0.13}$	$1.09^{+0.65}_{-0.57}$	$-1.06^{+0.72}_{-0.43}$	$58.6^{+33.5}_{-29.8}$	$0.30^{+0.16}_{-0.15}$
	$-0.36^{+0.31}_{-0.24}$	$2.76^{+0.65}_{-0.67}$	$0.15^{+0.32}_{-0.25}$	$76.1^{+17.3}_{-18.2}$	$0.65^{+0.14}_{-0.15}$
SPT-CLJ0508-6149	$-1.34^{+0.36}_{-0.29}$	$10.83^{+4.61}_{-4.10}$	$1.15^{+0.61}_{-0.25}$	$189.4^{+80.0}_{-71.3}$	$1.45^{+0.59}_{-0.52}$
	$-0.33^{+0.28}_{-0.29}$	$4.89^{+0.94}_{-1.11}$	$0.55^{+0.33}_{-0.33}$	$67.8^{+12.1}_{-15.2}$	$0.69^{+0.12}_{-0.15}$
SPT-CLJ0509-5342	$-0.95^{+0.36}_{-0.21}$	$6.09^{+1.65}_{-1.53}$	$0.77^{+0.36}_{-0.23}$	$151.7^{+38.9}_{-37.8}$	$1.26^{+0.30}_{-0.29}$
	$-0.40^{+0.29}_{-0.24}$	$4.38^{+0.73}_{-0.74}$	$0.81^{+0.24}_{-0.20}$	$87.2^{+13.0}_{-14.6}$	$1.00^{+0.14}_{-0.15}$
SPT-CLJ0509-6118	$-0.74^{+0.29}_{-0.21}$	$2.53^{+0.69}_{-1.13}$	$-0.27^{+0.74}_{-0.92}$	$103.1^{+27.2}_{-45.5}$	$0.69^{+0.18}_{-0.30}$
	$-0.50^{+0.24}_{-0.20}$	$3.62^{+0.55}_{-0.72}$	$0.33^{+0.30}_{-0.31}$	$111.1^{+14.6}_{-21.9}$	$0.98^{+0.13}_{-0.19}$
SPT-CLJ0516-5430	$-1.58^{+0.18}_{-0.10}$	$2.80^{+1.00}_{-0.96}$	$-0.31^{+0.35}_{-0.26}$	$211.8^{+70.9}_{-72.1}$	$1.07^{+0.35}_{-0.36}$
	$-0.89^{+0.22}_{-0.17}$	$3.63^{+0.91}_{-0.90}$	$0.24^{+0.31}_{-0.23}$	$163.7^{+40.1}_{-40.5}$	$1.19^{+0.28}_{-0.28}$
SPT-CLJ0516-5755	$-1.73^{+0.61}_{-0.26}$	$12.22^{+9.16}_{-5.41}$	$0.16^{+0.71}_{-0.14}$	$173.6^{+128.4}_{-76.4}$	$1.07^{+0.74}_{-0.44}$
	$-0.43^{+0.59}_{-0.43}$	$11.81^{+2.32}_{-3.37}$	$0.69^{+0.33}_{-0.28}$	$89.9^{+16.8}_{-25.3}$	$1.05^{+0.18}_{-0.26}$
SPT-CLJ0516-6312	$-1.62^{+0.30}_{-0.14}$	$2.14^{+1.32}_{-0.79}$	$-0.41^{+0.67}_{-0.25}$	$79.8^{+48.2}_{-29.1}$	$0.46^{+0.25}_{-0.15}$
	$-0.90^{+0.40}_{-0.16}$	–	–	–	–
SPT-CLJ0517-6119	$-0.51^{+0.47}_{-0.35}$	$7.14^{+2.40}_{-2.70}$	$-0.16^{+0.50}_{-0.33}$	$112.2^{+35.8}_{-42.1}$	$0.88^{+0.27}_{-0.31}$
	$-0.76^{+0.49}_{-0.28}$	$3.91^{+1.60}_{-1.49}$	$0.07^{+0.48}_{-0.31}$	$65.1^{+24.7}_{-24.4}$	$0.51^{+0.18}_{-0.17}$
SPT-CLJ0517-6311	$-1.74^{+0.38}_{-0.09}$	$3.19^{+2.08}_{-1.48}$	$-0.23^{+0.66}_{-0.28}$	$119.2^{+74.9}_{-54.8}$	$0.59^{+0.37}_{-0.27}$
	$-1.46^{+0.90}_{-0.35}$	–	–	–	–
SPT-CLJ0529-6051	$-0.68^{+0.64}_{-0.34}$	$3.38^{+1.99}_{-2.18}$	$-0.78^{+1.10}_{-0.69}$	$51.8^{+28.8}_{-32.8}$	$0.36^{+0.19}_{-0.22}$
	$0.01^{+0.57}_{-0.52}$	$4.27^{+1.11}_{-1.54}$	$0.35^{+0.48}_{-0.36}$	$43.5^{+10.6}_{-15.3}$	$0.50^{+0.11}_{-0.16}$
SPT-CLJ0534-5937	$-0.83^{+0.68}_{-0.25}$	–	–	–	–
	$0.02^{+0.49}_{-0.39}$	–	–	–	–
SPT-CLJ0539-6013	–	–	–	–	–
	–	–	–	–	–

Table 3.6 Individual best fit parameters for the SPT Cluster sample continued

clustername	α α_{RS}	ϕ^* ϕ^*_{RS} $[Mpc^{-3}mag^{-1}]$	Δm^* Δm^*_{RS} [mag]	N_g $N_{g,RS}$ #	$f_{*,hi} * 100$ $f_{*,lo} * 100$ [%]
SPT-CLJ0540-5744	$-1.62^{+0.70}_{-0.21}$	$4.90^{+5.51}_{-3.89}$	$-0.03^{+1.47}_{-0.41}$	$104.1^{+113.8}_{-81.8}$	$0.61^{+0.65}_{-0.47}$
	$-0.92^{+0.63}_{-0.35}$	$4.32^{+2.25}_{-2.75}$	$0.34^{+1.32}_{-2.27}$	$58.6^{+29.9}_{-36.7}$	$0.50^{+0.25}_{-0.31}$
SPT-CLJ0543-6219	$-0.63^{+0.52}_{-0.36}$	$3.75^{+1.23}_{-2.25}$	$0.02^{+1.03}_{-1.72}$	$100.2^{+30.4}_{-59.6}$	$0.77^{+0.23}_{-0.45}$
	$-0.53^{+0.34}_{-0.27}$	$3.19^{+0.63}_{-0.74}$	$0.70^{+0.39}_{-0.44}$	$67.4^{+11.7}_{-15.4}$	$0.71^{+0.12}_{-0.15}$
SPT-CLJ0546-6040	–	–	–	–	–
	$-1.61^{+1.01}_{-0.54}$	–	–	–	–
SPT-CLJ0549-6205	$-0.69^{+0.28}_{-0.23}$	$5.28^{+1.20}_{-1.08}$	$0.42^{+0.27}_{-0.21}$	$334.8^{+70.6}_{-68.5}$	$2.61^{+0.53}_{-0.51}$
	$-0.14^{+0.24}_{-0.21}$	$3.08^{+0.44}_{-0.43}$	$0.42^{+0.22}_{-0.17}$	$156.9^{+18.5}_{-22.0}$	$1.62^{+0.18}_{-0.21}$
SPT-CLJ0550-6358	$-1.41^{+0.98}_{-0.28}$	$9.56^{+6.22}_{-5.75}$	$0.39^{+0.83}_{-0.34}$	$149.7^{+95.6}_{-89.5}$	$1.01^{+0.62}_{-0.58}$
	$-1.08^{+0.81}_{-0.36}$	$4.39^{+2.76}_{-2.20}$	$0.79^{+0.83}_{-0.44}$	$49.7^{+29.9}_{-24.4}$	$0.50^{+0.26}_{-0.22}$
SPT-CLJ0555-6406	–	$14.58^{+2.91}_{-3.39}$	$0.47^{+0.31}_{-0.26}$	$685.3^{+132.1}_{-158.8}$	$4.50^{+0.87}_{-1.04}$
	$-0.16^{+0.25}_{-0.20}$	–	–	–	–
SPT-CLJ0655-5541	$-1.19^{+0.41}_{-0.15}$	–	–	–	–
	$-0.82^{+0.42}_{-0.28}$	$1.78^{+0.83}_{-0.87}$	$-0.04^{+0.96}_{-0.87}$	$44.2^{+20.1}_{-21.2}$	$0.34^{+0.14}_{-0.15}$
SPT-CLJ0658-5556	$-0.77^{+0.13}_{-0.10}$	$4.37^{+0.82}_{-0.69}$	$-0.07^{+0.21}_{-0.16}$	$480.8^{+89.3}_{-75.5}$	$3.11^{+0.57}_{-0.49}$
	$-0.26^{+0.15}_{-0.14}$	$4.33^{+0.52}_{-0.49}$	$0.33^{+0.16}_{-0.16}$	$353.6^{+41.4}_{-40.1}$	$3.05^{+0.35}_{-0.34}$
SPT-CLJ2248-4431	$-1.76^{+0.33}_{-0.25}$	$2.00^{+0.76}_{-0.60}$	$1.10^{+0.39}_{-0.24}$	$214.1^{+75.1}_{-63.7}$	$1.86^{+0.49}_{-0.41}$
	$-1.54^{+0.46}_{-0.29}$	$1.00^{+0.40}_{-0.33}$	$1.51^{+0.38}_{-0.25}$	$80.0^{+29.4}_{-25.9}$	$1.39^{+0.25}_{-0.22}$
SPT-CLJ2256-5414	–	–	–	–	–
	–	–	–	–	–
SPT-CLJ2259-5431	$-0.60^{+0.43}_{-0.33}$	$4.61^{+1.47}_{-1.63}$	$0.43^{+0.48}_{-0.38}$	$75.1^{+22.1}_{-26.1}$	$0.64^{+0.17}_{-0.20}$
	$-0.60^{+0.45}_{-0.35}$	$3.37^{+0.89}_{-0.93}$	$1.09^{+0.34}_{-0.28}$	$44.3^{+11.2}_{-11.9}$	$0.57^{+0.12}_{-0.12}$
SPT-CLJ2300-5616	$-1.42^{+0.28}_{-0.13}$	$2.18^{+0.81}_{-0.76}$	$-0.36^{+0.42}_{-0.28}$	$85.9^{+28.9}_{-29.4}$	$0.49^{+0.16}_{-0.16}$
	$-1.14^{+0.28}_{-0.16}$	$2.17^{+0.70}_{-0.67}$	$-0.11^{+0.41}_{-0.29}$	$65.0^{+18.5}_{-19.9}$	$0.46^{+0.12}_{-0.13}$
SPT-CLJ2301-5546	$-1.18^{+1.04}_{-0.32}$	$2.14^{+2.88}_{-1.83}$	$-0.68^{+2.70}_{-0.81}$	$30.1^{+39.0}_{-25.0}$	$0.20^{+0.24}_{-0.15}$
	$-0.28^{+0.68}_{-0.42}$	$3.10^{+1.22}_{-1.78}$	$-0.18^{+0.94}_{-1.15}$	$28.4^{+9.9}_{-15.7}$	$0.28^{+0.09}_{-0.14}$
SPT-CLJ2332-5358	$-0.40^{+0.33}_{-0.25}$	$4.90^{+1.41}_{-1.16}$	$0.21^{+0.43}_{-0.33}$	$134.0^{+36.2}_{-31.6}$	$1.06^{+0.28}_{-0.24}$
	$-0.04^{+0.32}_{-0.22}$	$4.65^{+0.64}_{-0.75}$	$0.66^{+0.28}_{-0.22}$	$101.0^{+11.8}_{-16.1}$	$1.09^{+0.12}_{-0.17}$
SPT-CLJ2342-5411	–	$9.25^{+10.12}_{-5.13}$	$0.56^{+0.88}_{-0.13}$	$154.5^{+167.2}_{-85.1}$	$0.98^{+1.01}_{-0.51}$
	–	$3.05^{+6.54}_{-2.72}$	$0.81^{+1.56}_{-0.36}$	$29.0^{+59.5}_{-25.0}$	$0.37^{+0.64}_{-0.27}$
SPT-CLJ2351-5452	$-0.40^{+0.36}_{-0.29}$	$5.82^{+1.66}_{-1.77}$	$0.28^{+0.50}_{-0.52}$	$113.7^{+31.7}_{-34.2}$	$0.91^{+0.25}_{-0.27}$
	$-0.29^{+0.29}_{-0.23}$	$5.83^{+1.00}_{-1.10}$	$0.58^{+0.32}_{-0.29}$	$95.3^{+14.5}_{-17.8}$	$0.95^{+0.14}_{-0.17}$
SPT-CLJ2354-5633	$-1.13^{+0.30}_{-0.17}$	$3.72^{+1.65}_{-1.53}$	$-0.40^{+0.60}_{-0.33}$	$90.4^{+37.8}_{-36.8}$	$0.52^{+0.20}_{-0.20}$
	$-0.46^{+0.36}_{-0.27}$	$4.98^{+1.21}_{-1.10}$	$0.39^{+0.28}_{-0.22}$	$71.4^{+17.0}_{-15.6}$	$0.66^{+0.14}_{-0.13}$

Note – The columns are summarized the following: We present for each SPT cluster the faint end slope α, the characteristic galaxy density ϕ^*, the difference between our passive evolution model and the best fit Δm^*, the Halo Occupation number N_g derived from the LF fits and the stellar mass fraction f_* both for the full and RS population. Note that for clusters where the LF was unconstrained or showed multiple peaks in the likelihood distribution we do not report a best fit.

Chapter 4

Final remarks

In this Thesis we studied and characterized the galaxy populations in galaxy clusters selected by the SZ effect, which provides mass limited cluster samples over a wide redshift range. With optical multiband imaging data from the Science Verification phase of the Dark Energy Survey we were able to study a sample of 74 SPT clusters extending to a redshift of ~ 1.1. Such an SZE selected sample is well suited for cosmological probes and any evolutionary studies of the cluster galaxy population. In this Thesis we used the advantage of an SZE selected sample to study how galaxy populations in cluster environments evolve with mass and redshift. In summary the following picture of galaxy evolution in clusters has emerged:
Our results have shown that the characteristic properties of the cluster galaxy populations change since $z = 1$. In general we find good agreement with previous and recent studies from the literature. Yet due to the redshift range and sample size we are able to present more precise measurements of the population evolution. A scenario emerges where infall from the field over the full redshift range provides a supply of non-RS galaxies at all luminosities. Thus it is expected that a population of infalling field galaxies can be detected in addition to the older, mainly early-type red galaxies. These cluster galaxies are transformed into RS galaxies over cosmic time. This happens through initial quenching followed by a natural dying away of the most luminous, massive young stars on timescales of ~ 3 Gyr. Given enough time, infalling spiral galaxies may acquire characteristics that are similar to S0 galaxies. The truncation of star-formation for infalling spiral field galaxies has been explained via various dynamical mechanisms such as ram pressure stripping or galaxy harassment (e.g. Moore et al. 1996; Goto et al. 2004). The concentration and the characteristic number density of $m \sim m^*$ galaxies in the full population tend to fall over time, which might be due to merging onto and growth of the giant central galaxies. One element of our population study remaining to be explained is the decrease in color width of the RS over cosmic time. The RS width presumably constrains the heterogeneity in age and metallicity at fixed galaxy luminosity of the old stellar populations that dominate in RS galaxies. Our full set of observational results is confronting specific galaxy formation simulations. Matching the mass and redshift trends presented here would lead to significant improvements in our understanding of the physical processes in the dense cluster environment.
This study will benefit significantly from extending the sample size within the full DES survey footprint. When the survey is completed, nearly all of the 516 identified and optically confirmed clusters in Bleem et al. (2015) will be covered within DES and the majority will

have redshift measurements as well as robust mass estimates. The resulting cluster sample will provide a new source of information based on the clean SZE selection function that will greatly improve our understanding of the evolution of galaxies in clusters. The depth of the full survey will be equivalent to the Science Verification phase and thus evolutionary trends might be analyzed down to a redshift of ~ 1. This can then help to verify (or falsify) our evolutionary trends with better statistical significance. A complementary study will be completed on X-ray selected clusters with a bayesian approach for studying the cluster LF (*Zhang et al. in prep*). The mean mass of this cluster sample is around $1 \times 10^{14} M_{\odot}$. This study will give new information on the constraints on mass trends for the cluster LF properties, which could not be significantly seen in our high mass-limited sample by an extension down to group scale systems.

A valuable extension of this study is the analysis of the radial dependence of the characteristic LF parameters. The LF is an optimal tool to search for changes in the galaxy population. In particular, the LF can help one understand the influence of the cluster environment on the galaxy population. A change in the shape of the LF as a function of cluster-centric radius provides information about the dynamical processes at work in the cluster environment. The dependence on radius is expected because the mixture of galaxy morphological types is varying as a function of radius. This is explained due to the characteristic morphology density relation (Dressler 1980). In that context Barkhouse et al. (2007) examined a sample of 57 low redshift Abell clusters ($z < 0.2$) and found variation in the LFs with cluster centric distance. They analyzed the LF for the full and a color selected red and blue population. They find an increase in the steepness of the faint-end slope with increasing radius. This change in α is largest for the full galaxy sample, while the blue population is less affected. Like in our analysis they find that the red color selected galaxy population shows shallower faint end slopes compared to the blue and full cluster population. They note that the very rapid increase in the faint end slope for the full LF might be due to a combination of steepening slope for both red and blue LFs. Furthermore the contribution from the blue population is more dominant in the outskirts of the cluster region. The tendency for the LF to become flatter with decreasing cluster-centric radius supports the hypothesis that dwarf galaxies are tidally disrupted near the cluster center. It has been already claimed by López-Cruz et al. (1997), that the faint-end slope of the galaxy LF is subject to environmental effects. They claimed that α results from the disruption of a large fraction of dwarf galaxies during the early stages of cluster evolution, which can explain the origin of the luminous central massive galaxies. Thus there has been seen strong evidence that the mixture of giant and dwarf galaxies depends on the fraction of the cluster region that is measured. Compared to the Barkhouse et al. (2007) analysis, a study of radial dependencies with an SZE selected sample will have the advantage of robust mass estimates and therefore robust radius measurements. As DES is a contiguous survey of the entire SPT survey region, the data are ideally suited for a radial dependence study. We are then able to examine a large portion of the cluster outskirts to study the infall of field galaxies in an homogeneously selected cluster sample over a wide redshift range. In addition it is worthwhile to compare the radial trends for the color selected red and blue populations found in Barkhouse et al. (2007), who used a fixed color box around the RS color, with our introduced weighted approach. A radial study based on the combination of deep multi band optical data of DES and a well selected clus-

ter sample from SPT will shed further light on the cluster formation via infall of field galaxies.

In addition it is worthwhile to analyze the evolution of the red fraction as a function of radius with RP or stacked color distribution constraints. This is an extension to a study from Loh et al. (2008). They found that the red fraction of galaxies decreases as a function of increasing redshift for all cluster-centric radii, which is consistent with the Butcher-Oemler (BO) effect. Butcher & Oemler (1984) reported an increase in the fraction of blue galaxies in ~ 30 rich galaxy clusters out to a redshift of 0.5 in comparison to local galaxy clusters. Since then it has been confirmed photometrically and spectroscopically (e.g. Ellingson et al. 2001). However, proofing the existence of the BO effect has been challenging from the beginning. In X-ray and near-infrared selected galaxy clusters the BO evolutionary trend was either weaker or even non-existent (e.g. Smail et al. 1998). As the original BO clusters were selected from photographic plates, it might have introduced selection biases that lead to a strong redshift evolutionary trend. Optical selections might have created cluster samples with lower masses and unvirialized merging systems that have preferentially higher star formation rates. In addition earlier studies suffered from a low number of galaxy clusters and thus poor statistical proofs. Thus a uniformly selected cluster sample that spans a large redshift range with clusters of similar masses (such as our SPT sample) is ideally suited for a reanalysis of the BO effect. A further crucial element of this discussion is the mass dependent radius in clusters. Early studies used a fixed radial size, which is probing a different galaxy population in clusters with different masses. With the SZE selected sample, having robust mass and thus radius measurements, we are able to probe the same population in different radial bins.
The study from Loh et al. (2008) used a sample of ~ 1000 clusters selected from the Red-Sequence Cluster Survey extending to redshift of ~ 0.9 to study the evolution of the color magnitude relation. They therefore constructed composite color-magnitude diagrams within different redshift bins and used a statistical background subtraction. Their findings suggest that in the cluster core the red fraction seems to decrease more mildly than in the cluster outskirts within $1 - 2R_{200}$, where they report a significant drop from $\sim 80\%$ towards $\sim 30\%$ at redshift 0.9. Qualitatively this is consistent with BO, yet they stress the difficulty of comparison between other methods, as they used additional correction factors for scatter and k-corrections for blue galaxies. Due to this reason their result showed a milder decrease in the blue fraction over cosmic time as the original BO effect. As they do not report evolutionary trends for the radial dependence and just show their measurements, it is worthwhile to repeat this analysis on a homogeneously selected clusters with fine radial binning and extension to large radii. Thus their hypothesis of radial gradients in the galaxy populations (in a sense that red fractions are higher in cluster cores than within larger radii at all redshifts) can be proofed or falsified. Since then there were only few studies that dealt with the confirmation of the BO effect. For example Urquhart et al. (2010) used a sample of 34 X-ray selected clusters from XMM at intermediate redshift between $0.15 < z < 0.41$. They studied the color bimodality and computed blue fractions with similar criteria than the original BO paper. They also find increasing blue fraction with redshift. Fitting for redshift and mass evolution (with a proxy from the X-ray temperature) they were able to rule out the non-evolution scenario with redshift, explicitly confirming the BO effect, yet they were not able to constrain the mass dependency. In addition they divided their cluster sample into cool, mid and hot

clusters based on their X-ray temperature. This enables them to identify an environmental dependence of the cluster blue fraction in a sense that cool clusters with preferentially lower cluster mass exhibit higher blue fractions than hotter (higher mass) clusters. De Propris et al. (2013) also revisit the phenomenon of the BO effect with a sample of 11 intermediate redshift ($0.2 < z < 0.6$) galaxy clusters. They report a distinct increase in the fraction of blue galaxies out to their highest redshift of 0.6 at all luminosities. They further note that bright blue galaxies are much more common in high redshift clusters than in low redshift systems. It remains still unknown whether this reflects evolution in the luminosity function of infalling field galaxies or an increase in the quenching efficiency with decreasing redshift. To conclude, a combination of radial-, mass-, and redshift- dependence of the evolution of the red fraction will be crucial to understand the history of the galaxy population within dense cluster environments and the effect of infall from field galaxies. Simulations of galaxy formation and evolution will benefit significantly from such observational constraints.

Bibliography

Abell, G. O. 1958, ApJS, 3, 211

Anderson, L., et al. 2012, ArXiv e-prints, 1203.6594

Andersson, K., et al. 2011, ApJ, 738, 48

Andreon, S. 1998, A&A, 336, 98

——. 2010, MNRAS, 407, 263

Andreon, S., & Congdon, P. 2014, ArXiv e-prints, 1406.1651

Arimoto, N., & Yoshii, Y. 1987, A&A, 173, 23

Arnaud, M., Pointecouteau, E., & Pratt, G. W. 2007, A&A, 474, L37

Babcock, H. W. 1939, Lick Observatory Bulletin, 19, 41

Bahcall, N. A., & Cen, R. 1992, ApJ, 398, L81

Balogh, M. L., McCarthy, I. G., Bower, R. G., & Eke, V. R. 2008, MNRAS, 385, 1003

Barkhouse, W. A., Yee, H. K. C., & López-Cruz, O. 2007, ApJ, 671, 1471

Bartelmann, M. 1996, A&A, 313, 697

Bartelmann, M., & Schneider, P. 2001, Phys. Rep., 340, 291

Bassett, B., & Hlozek, R. 2010, Baryon acoustic oscillations, ed. P. Ruiz-Lapuente, 246

Baum, W. A. 1959, in IAU Symposium, Vol. 10, The Hertzsprung-Russell Diagram, ed. J. L. Greenstein, 23

Benson, B. A., et al. 2013, ApJ, 763, 147

Berlind, A. A., et al. 2003, ApJ, 593, 1

Bertin, E. 2006, in Astronomical Society of the Pacific Conference Series, Vol. 351, Astronomical Data Analysis Software and Systems XV, ed. C. Gabriel, C. Arviset, D. Ponz, & S. Enrique, 112–+

Bertin, E., & Arnouts, S. 1996, A&AS, 117, 393

Beutler, F., et al. 2011, MNRAS, 416, 3017

Binggeli, B., Sandage, A., & Tammann, G. A. 1988, ARA&A, 26, 509

Birkinshaw, M. 1991, in Physical Cosmology, eds. A. Blanchard, L. Celnikier, M. Lachi'eze-Rey, J. Tran Thanh Van, Editions Frontieres, Gif sur Yvette, France, 177

Birkinshaw, M. 1999, Physics Reports, 310, 97

Bleem, L. E., et al. 2015, ApJS, 216, 27

——. 2014, ArXiv e-prints, 1409.0850

Blumenthal, G. R., Faber, S. M., Flores, R., & Primack, J. R. 1986, ApJ, 301, 27

Bocquet, S., et al. 2014, ArXiv e-prints, 1407.2942

Bower, R. G., Benson, A. J., Malbon, R., Helly, J. C., Frenk, C. S., Baugh, C. M., Cole, S., & Lacey, C. G. 2006, MNRAS, 370, 645

Bower, R. G., Lucey, J. R., & Ellis, R. S. 1992, MNRAS, 254, 601

Bruzual, G., & Charlot, S. 2003, MNRAS, 344, 1000

Budzynski, J. M., Koposov, S. E., McCarthy, I. G., & Belokurov, V. 2014, MNRAS, 437, 1362

Budzynski, J. M., Koposov, S. E., McCarthy, I. G., McGee, S. L., & Belokurov, V. 2012, MNRAS, 423, 104

Butcher, H., & Oemler, Jr., A. 1984, ApJ, 285, 426

Capozzi, D., Collins, C. A., Stott, J. P., & Hilton, M. 2012, MNRAS, 419, 2821

Carlberg, R. G., et al. 1997, ApJ, 485, L13+

Carlstrom, J. E., et al. 2011, PASP, 123, 568

Carlstrom, J. E., Holder, G. P., & Reese, E. D. 2002, ARA&A, 40, 643

Carlstrom, J. E., Joy, M. K., Grego, L., Holder, G. P., Holzapfel, W. L., Mohr, J. J., Patel, S., & Reese, E. D. 2000, Physica Scripta Volume T, 85, 148

Cash, W. 1979, ApJ, 228, 939

Chiboucas, K., & Mateo, M. 2006, AJ, 132, 347

Chiu, I., et al. 2014, ArXiv e-prints, 1412.7823

Coe, D. 2010, ArXiv e-prints, 1005.0411

Cole, S., & Lacey, C. 1996, MNRAS, 281, 716

Contini, E., De Lucia, G., Villalobos, Á., & Borgani, S. 2014, MNRAS, 437, 3787

Cowie, L. L., & Binney, J. 1977, ApJ, 215, 723

De Lucia, G., & Blaizot, J. 2007, MNRAS, 375, 2

De Propris, R., Phillipps, S., & Bremer, M. N. 2013, MNRAS, 434, 3469

de Propris, R., Stanford, S. A., Eisenhardt, P. R., Dickinson, M., & Elston, R. 1999, AJ, 118, 719

DeMaio, T., Gonzalez, A. H., Zabludoff, A., Zaritsky, D., & Bradač, M. 2015, MNRAS, 448, 1162

Desai, S., et al. 2012, ApJ, 757, 83

Desai, V., et al. 2007, ApJ, 660, 1151

Diehl, H. T., et al. 2014, in Society of Photo-Optical Instrumentation Engineers (SPIE) Conference Series, Vol. 9149, Society of Photo-Optical Instrumentation Engineers (SPIE) Conference Series, 0

Dressler, A. 1980, ApJ, 236, 351

Duffy, A. R., Schaye, J., Kay, S. T., & Dalla Vecchia, C. 2008, MNRAS, 390, L64

Duffy, A. R., Schaye, J., Kay, S. T., Dalla Vecchia, C., Battye, R. A., & Booth, C. M. 2010, MNRAS, 405, 2161

Einasto, J. 1965, Trudy Astrofizicheskogo Instituta Alma-Ata, 5, 87

Eisenstein, D. J., et al. 2005, ApJ, 633, 560

Ellingson, E., Lin, H., Yee, H. K. C., & Carlberg, R. G. 2001, ApJ, 547, 609

Ellis, R. S., Smail, I., Dressler, A., Couch, W. J., Oemler, Jr., A., Butcher, H., & Sharples, R. M. 1997, ApJ, 483, 582

Ettori, S., Dolag, K., Borgani, S., & Murante, G. 2006, MNRAS, 365, 1021

Ettori, S., Gastaldello, F., Leccardi, A., Molendi, S., Rossetti, M., Buote, D., & Meneghetti, M. 2010, A&A, 524, A68

Foreman-Mackey, D., Hogg, D. W., Lang, D., & Goodman, J. 2013, PASP, 125, 306

Freese, K., Fields, B., & Graff, D. 2000, ArXiv Astrophysics e-prints

Fujita, Y. 1998, ApJ, 509, 587

Fujita, Y., & Goto, T. 2004, PASJ, 56, 621

Gilbank, D. G., Yee, H. K. C., Ellingson, E., Gladders, M. D., Loh, Y., Barrientos, L. F., & Barkhouse, W. A. 2008, ApJ, 673, 742

Gladders, M. D., Lopez-Cruz, O., Yee, H. K. C., & Kodama, T. 1998, ApJ, 501, 571

Gladders, M. D., & Yee, H. K. C. 2005, ApJS, 157, 1

Goto, T., Yagi, M., Tanaka, M., & Okamura, S. 2004, MNRAS, 348, 515

Gunn, J. E., & Gott, III, J. R. 1972, ApJ, 176, 1

Guy, J., et al. 2010, A&A, 523, A7

High, F. W., et al. 2012, ApJ, 758, 68

Hilton, M., et al. 2013, MNRAS, 435, 3469

——. 2009, ApJ, 697, 436

Hinshaw, G., et al. 2013, The Astrophysical Journal Supplement Series, 208, 19

Holder, G., Haiman, Z., & Mohr, J. J. 2001, ApJ, 560, L111

Holtzman, J. A. 1989, ApJS, 71, 1

Hu, W., & Dodelson, S. 2002, ARA&A, 40, 171

Hubble, E. 1929, Contributions from the Mount Wilson Observatory, vol. 3, pp.23-28, 3, 23

Hubble, E. P. 1926, ApJ, 64, 321

Jenkins, L. P., Hornschemeier, A. E., Mobasher, B., Alexander, D. M., & Bauer, F. E. 2007, ApJ, 666, 846

Jerjen, H., & Tammann, G. A. 1997, A&A, 321, 713

Kauffmann, G., & Charlot, S. 1998, ArXiv Astrophysics e-prints

Kodama, T., & Arimoto, N. 1997, A&A, 320, 41

Kodama, T., & Bower, R. G. 2001, MNRAS, 321, 18

Koester, B. P., et al. 2007, ApJ, 660, 221

Kravtsov, A. V., Nagai, D., & Vikhlinin, A. A. 2005, ApJ, 625, 588

Leauthaud, A., et al. 2012, ApJ, 744, 159

Lin, Y., Mohr, J. J., Gonzalez, A. H., & Stanford, S. A. 2006, ApJ, 650, L99

Lin, Y., Mohr, J. J., & Stanford, S. A. 2003, ApJ, 591, 749

——. 2004, ApJ, 610, 745

Liu, J., et al. 2015, MNRAS, 449, 3370

Loh, Y., Ellingson, E., Yee, H. K. C., Gilbank, D. G., Gladders, M. D., & Barrientos, L. F. 2008, ApJ, 680, 214

López-Cruz, O., Yee, H. K. C., Brown, J. P., Jones, C., & Forman, W. 1997, ApJ, 475, L97

Mancone, C. L., et al. 2012, ApJ, 761, 141

Mancone, C. L., & Gonzalez, A. H. 2012, PASP, 124, 606

Mancone, C. L., Gonzalez, A. H., Brodwin, M., Stanford, S. A., Eisenhardt, P. R. M., Stern, D., & Jones, C. 2010, ApJ, 720, 284

Mantz, A., Allen, S. W., Ebeling, H., Rapetti, D., & Drlica-Wagner, A. 2010, MNRAS, 406, 1773

Marrone, D. P., et al. 2012, ApJ, 754, 119

Mather, J. C., et al. 1990, in Liege International Astrophysical Colloquia, Vol. 29, Liege International Astrophysical Colloquia, ed. B. Kaldeich, 25–31

McGee, S. L., Balogh, M. L., Bower, R. G., Font, A. S., & McCarthy, I. G. 2009, MNRAS, 400, 937

Mei, S., et al. 2009, ApJ, 690, 42

Melchior, P., et al. 2014, ArXiv e-prints, 1405.4285

Melin, J.-B., Bartlett, J. G., & Delabrouille, J. 2006, A&A, 459, 341

Messier, C. 1781, Catalogue des Nebuleuses des amas d'Etoiles (Catalog of Nebulae and Star Clusters), Tech. rep.

Moffat, A. F. J. 1969, A&A, 3, 455

Mohr, J. J., et al. 2008, in Society of Photo-Optical Instrumentation Engineers (SPIE) Conference Series, Vol. 7016, Society of Photo-Optical Instrumentation Engineers (SPIE) Conference Series

Mohr, J. J., et al. 2012, in Society of Photo-Optical Instrumentation Engineers (SPIE) Conference Series, Vol. 8451, Society of Photo-Optical Instrumentation Engineers (SPIE) Conference Series, 0

Mohr, J. J., Geller, M. J., Fabricant, D. G., Wegner, G., Thorstensen, J., & Richstone, D. O. 1996, ApJ, 470, 724

Moore, B., Katz, N., Lake, G., Dressler, A., & Oemler, A. 1996, Nature, 379, 613

Muzzin, A., et al. 2014, ApJ, 796, 65

——. 2012, ApJ, 746, 188

Muzzin, A., Yee, H. K. C., Hall, P. B., Ellingson, E., & Lin, H. 2007a, ApJ, 659, 1106

Muzzin, A., Yee, H. K. C., Hall, P. B., & Lin, H. 2007b, ApJ, 663, 150

Nagai, D., & Kravtsov, A. V. 2005, ApJ, 618, 557

Navarro, J. F., Frenk, C. S., & White, S. D. M. 1996, ApJ, 462, 563

——. 1997, ApJ, 490, 493

Ngeow, C., et al. 2006, in Society of Photo-Optical Instrumentation Engineers (SPIE) Conference Series, Vol. 6270, Society of Photo-Optical Instrumentation Engineers (SPIE) Conference Series

Oemler, Jr., A. 1974, ApJ, 194, 1

Oort, J. H. 1932, Bull. Astron. Inst. Netherlands, 6, 249

Padmanabhan, N., Xu, X., Eisenstein, D. J., Scalzo, R., Cuesta, A. J., Mehta, K. T., & Kazin, E. 2012, ArXiv e-prints, 1202.0090

Papadopoulos, A., et al. 2015, MNRAS, 449, 1215

Papovich, C., et al. 2010, ApJ, 716, 1503

Perlmutter, S. 2003, Physics Today, 56, 53

Perlmutter, S., et al. 1999, ApJ, 517, 565

Peterson, J. R., & Fabian, A. C. 2006, Phys. Rep., 427, 1

Planck Collaboration, et al. 2014, A&A, 571, A29

——. 2015, ArXiv e-prints, 1502.01598

——. 2011, A&A, 536, A26

Planelles, S., Borgani, S., Dolag, K., Ettori, S., Fabjan, D., Murante, G., & Tornatore, L. 2013, MNRAS, 431, 1487

Poggianti, B. M., et al. 2001, ApJ, 562, 689

Popesso, P., Biviano, A., Böhringer, H., & Romaniello, M. 2006, A&A, 445, 29

——. 2007, A&A, 464, 451

Postman, M., et al. 2005, ApJ, 623, 721

Puchwein, E., Springel, V., Sijacki, D., & Dolag, K. 2010, MNRAS, 406, 936

Rasia, E., Borgani, S., Ettori, S., Mazzotta, P., & Meneghetti, M. 2013, ApJ, 776, 39

Regnault, N., et al. 2009, A&A, 506, 999

Reichardt, C. L., et al. 2013, ApJ, 763, 127

Rephaeli, Y. 1995, ARA&A, 33, 541

Riess, A. G., et al. 1998, AJ, 116, 1009

Rines, K., Geller, M. J., Diaferio, A., Kurtz, M. J., & Jarrett, T. H. 2004, AJ, 128, 1078

Rozo, E., Rykoff, E. S., Bartlett, J. G., & Melin, J. B. 2014, ArXiv e-prints, 1401.7716, 1401.7716

Rozo, E., et al. 2009, ApJ, 699, 768

——. 2010, ApJ, 708, 645

Rudnick, G., et al. 2009, ApJ, 700, 1559

Ruel et al. 2012, In Preparation

Rykoff, E. S., et al. 2012, ApJ, 746, 178

——. 2014, ApJ, 785, 104

Sarazin, C. L. 2008, in Lecture Notes in Physics, Berlin Springer Verlag, Vol. 740, A Pan-Chromatic View of Clusters of Galaxies and the Large-Scale Structure, ed. M. Plionis, O. López-Cruz, & D. Hughes, 1–4020

Saro, A., Bazin, G., Mohr, J., & Dolag, K. 2012, ArXiv e-prints, 1203.5708

Schaeffer, R., & Silk, J. 1988, ApJ, 332, 1

Schaffer, K. K., et al. 2011, ApJ, 743, 90

Schechter, P. 1976, ApJ, 203, 297

Schindler, S. 1996, A&A, 305, 756

Schlafly, E. F., et al. 2012, ApJ, 756, 158

Schmidt, R. W., & Allen, S. W. 2007, MNRAS, 379, 209

Skelton, R. E., Woudt, P. A., & Kraan-Korteweg, R. C. 2009, MNRAS, 396, 2367

Skrutskie, M. F., et al. 2006, AJ, 131, 1163

Smail, I., Edge, A. C., Ellis, R. S., & Blandford, R. D. 1998, MNRAS, 293, 124

Song, J., Mohr, J. J., Barkhouse, W. A., Warren, M. S., & Rude, C. 2012a, ApJ, 747, 58

Song, J., et al. 2012b, ApJ, 761, 22

Spitzer, Jr., L., & Baade, W. 1951, ApJ, 113, 413

Springel, V., et al. 2005, Nature, 435, 629

Stanford, S. A., Eisenhardt, P. R., & Dickinson, M. 1998, ApJ, 492, 461

Story, K. T., et al. 2013, ApJ, 779, 86

Stott, J. P., Smail, I., Edge, A. C., Ebeling, H., Smith, G. P., Kneib, J.-P., & Pimbblet, K. A. 2007, ApJ, 661, 95

Sunyaev, R. A., & Zel'dovich, Y. B. 1972, Comments on Astrophysics and Space Physics, 4, 173

Suzuki, A., et al. 2012, Journal of Low Temperature Physics, 167, 852

Tanaka, M., Kodama, T., Kajisawa, M., Bower, R., Demarco, R., Finoguenov, A., Lidman, C., & Rosati, P. 2007, MNRAS, 377, 1206

Taniguchi, Y., et al. 2005, Journal of Korean Astronomical Society, 38, 187

The DES Collaboration, et al. 2015, ArXiv e-prints, 1503.02584

Urquhart, S. A., Willis, J. P., Hoekstra, H., & Pierre, M. 2010, MNRAS, 406, 368

van der Burg, R. F. J., Hoekstra, H., Muzzin, A., Sifón, C., Balogh, M. L., & McGee, S. L. 2014a, ArXiv e-prints, 1412.2137

van der Burg, R. F. J., et al. 2013a, A&A, 557, A15

——. 2013b, A&A, 557, A15

van der Burg, R. F. J., Muzzin, A., Hoekstra, H., Wilson, G., Lidman, C., & Yee, H. K. C. 2014b, A&A, 561, A79

Vanderlinde, K., et al. 2010, ApJ, 722, 1180

Vikhlinin, A., et al. 2009, ApJ, 692, 1060

Voit, G. M. 2005, Reviews of Modern Physics, 77, 207

Weymann, R. 1966, ApJ, 145, 560

Yee, H. K. C., Gladders, M. D., & López-Cruz, O. 1999, in Astronomical Society of the Pacific Conference Series, Vol. 191, Photometric Redshifts and the Detection of High Redshift Galaxies, ed. R. Weymann, L. Storrie-Lombardi, M. Sawicki, & R. Brunner, 166

Zenteno, A., et al. 2011, ApJ, 734, 3

Zhuravleva, I., et al. 2014, Nature, 515, 85

Zwicky, F. 1937, ApJ, 86, 217

Zwicky, F., Herzog, E., Wild, P., Karpowicz, M., & Kowal, C. T. 1961, Catalogue of galaxies and of clusters of galaxies, Vol. I

Curriculum vitae

Christina Hennig

Citizenship: German

Professional Experience

2012–2015 **Department of physics of the Ludwig-Maximilians-Universitaet**
PhD student in astrophysics working on galaxy cluster cosmology

List of scientific Publications

Refereed Publications

- Liu, J., **Hennig, C.** ,..., 2015, *Optical confirmation and redshift estimation of the Planck cluster candidates overlapping the Pan-STARRS Survey.* MNRAS, 449, 3370
- Liu, J. ,..., **Hennig, C.** ,..., 2015, *Analysis of Sunyaev-Zeldovich effect mass-observable relations using South Pole Telescope observations of an X-ray selected sample of low-mass galaxy clusters and groups.* MNRAS, 448, 2085
- Bleem, L. ,..., **Hennig, C.** ,..., 2015, *Galaxy Clusters Discovered via the Sunyaev-Zeldovich Effect in the 2500-Square-Degree SPT-SZ Survey.* ApJS, 216, 27
- Bocquet, S. ,..., **Hennig, C.** ,..., 2015, *Mass Calibration and Cosmological Analysis of the SPT-SZ Galaxy Cluster Sample Using Velocity Dispersion σ_v and X-Ray Y_X Measurements.* ApJ, 799, 214
- Saro, S. ,..., **Hennig, C.** ,..., 2014, *Constraints on the CMB temperature evolution using multiband measurements of the Sunyaev-Zeldovich effect with the South Pole Telescope.* MNRAS, 440, 2610

Articles in Preparation

- **Hennig, C.** ,..., 2015, *Galaxy Populations in massive galaxy clusters out to $z = 1.1$, Part 1.* in prep.

- **Hennig, C.** ,..., 2015, *Galaxy Populations in massive galaxy clusters out to* $z = 1.1$*, Part 2.* in prep.
- Zhang, Y. ,..., **Hennig, C.** ,..., 2015, *Galaxies in X-ray Selected Clusters and Groups in Dark Energy Survey Data: Stellar Mass Growth of Bright Central Galaxies Since* $z{\sim}1.2$*.* arXiv:1504.02983
- Chiu, I. ,..., **Hennig, C.** ,..., 2014, *Baryon Content of Massive Galaxy Clusters* ($0.57 < z < 1.33$). arXiv:1412.7823
- Baxter, E. J. ,..., **Hennig, C.** ,..., 2014, *A Measurement of Gravitational Lensing of the Cosmic Microwave Background by Galaxy Clusters Using Data from the South Pole Telescope.* arXiv:1412.7521

Acknowledgments

I want to thank my supervisor Joseph Mohr for his support,advise, comments and the possibility of observing in Chile as well as various travels. I want to express my gratitude to Andi Burkert for his personal support and secondary science opinion on the thesis. I want to thank the DES cluster working group for helpful discussions on the telecons. I want to express my gratitude to my fellow-students Sebastian Bocquet, Corvin Gangkofner, I-Non Chiu, Nikhel Gupta, Raffaella Capasso and (former)- postdocs Alfredo Zenteno, Jiayi Liu, Alex Saro, Jörg Dietrich, Kerstin Paech, Martin Kümmel, Shantanu Desai and Veronica Strazullo in my group. Thank you for lively (non-science) discussions and help on my way to graduation. Finally, thanks to my family, whose support and care have helped me throughout all my studies. Most importantly my deepest gratitude goes to my best friend Leonie and my boyfriend Carsten Ennulat, my contact person for coding problems. In various dark frustrating moments, your love has been my guiding light. At the end of the day, you helped me recover the right focus of what live is essentially about.